AN ABSTRACT OF THE THESIS OF

Michael D. Sabo for the degree of Master of Science in Mechanical Engineering presented on March 5, 2012.

Title: Performance and Flow Stability Characteristics in Two-Phase Confined Impinging Jets.

Abstract approved: _____

Deborah V. Pence

Advances in electronics fabrication, coupled with the demand for increased computing power, have driven the demand for innovative cooling solutions to dissipate waste heat generated by these devices. To meet future demands, research and development has focused on robust and stable two-phase heat transfer devices. A confined impinging jet is explored as means of utilizing two-phase heat transfer while minimizing flow instabilities observed in microchannel devices.

The test configuration consists of a 4 mm diameter jet of water that impinges on a 38 mm diameter heated aluminum surface. Experimental parameters include inlet mass flow rates from 150 to 600 g/min, nozzle-to-surface spacing from 1 to 8 mm, and input heat fluxes from 0 from 90 W/cm2. Results were used to assess the influence of the testing parameters on the heat transfer performance and stability characteristics of a two-phase confined impinging jet. Stability characteristics were explored using power spectral densities (PSDs) of the inlet pressure time series data.

Confined imping jets, over the range of conditions tested, were found to be

stable and an efficient means of removing large amounts of waste heat. The radial geometry of the confined jet allows the fluid to expand as it flows radially away from the nozzle, which suppresses instabilities found in microchannel array geometries. Conditions of the heater surface were found to strongly influence two-phase performance. Analysis of PSDs, for stable operation, showed dominate frequencies in the range of 1-4 Hz, which were attributed to generated vapor expanding in the outlet plenum and the subsequent collapse as it condensed. A stability indicator was developed by inducing artificial instabilities into the system by varying the amount of cross sectional area available for outlet vapor removal and compared to the results for stable operation.

Performance and Flow Stability Characteristics in Two-Phase Confined Impinging Jets.

by

Michael D. Sabo

A THESIS

submitted to

Oregon State University

in partial fulfillment of
the requirements for the
degree of

Master of Science

Presented March 5, 2012
Commencement June 2012

Master of Science thesis of Michael D. Sabo presented on March 5, 2012.

APPROVED:

Major Professor, representing Mechanical Engineering

Head of the School of Mechanical, Industrial, and Manufacturing Engineering

---

Dean of the Graduate School

I understand that my thesis will become part of the permanent collection of Oregon State University libraries. My signature below authorizes release of my thesis to any reader upon request.

Michael D. Sabo, Author

ACKNOWLEDGEMENTS

Special thanks goes to my parents, David and Patti Sabo, and my sister, Megan Sabo, for all their support and encouragement through the many years of school. I would also like to thank Kimberly Stanek for her help through the final months of testing and writing. Her enthusiasm and support made the entire process much more manageable. I would like to thank my advisor, Dr. Deborah Pence, for giving me the opportunity to work in her laboratory and for her guidance in throughout graduate school. I would like to thank Dr. James Liburdy and Dr. Vinod Narayanan for serving on my committee and assisting in several phases of the research process. A very special thanks goes to Christopher Stull for sharing his expertise and friendship over the years that we worked together. Additionally I would like to thank Nick Cappello, Randall Fox, and Adam Damiano for the long hours of data collection they assisted with.

TABLE OF CONTENTS

TABLE OF CONTENTS (Continued)

LIST OF FIGURES

LIST OF FIGURES (Continued)

LIST OF FIGURES (Continued)

LIST OF TABLES

LIST OF APPENDICES

LIST OF APPENDIX FIGURES

LIST OF APPENDIX TABLES

Nomenclature

A	Area (m^2)
c_p	Specific heat ($kJ/kg-k$)
D	Diameter (m)
E	Total Energy (kW)
G	Mass Flux (kg/m^2-s)
g	Gravitational constant (m/s^2)
H	Nozzle-to-surface spacing (m)
h	Heat transfer coefficient (W/m^2-K)
i	Enthalpy (kJ/kg)
i_{lv}	Heat of vaporization (kJ/kg)
k	Thermal conductivity ($W/m-K$)
L	Nozzle Length (m)
Nu	Nusselt number
P	Pressure (kPa)
Pr	Prandtl number

Q Electrical Power (kW)

q'' Heat flux (W/m^2)

r Radius (m)

Re Reynolds number

$S_{y,x}$ Standard error estimate

T Temperature (^oC)

V Velocity (m/s)

Greek Letters and Symbols

Δ Difference

$\dot{m}$ Mass flow rate (kg/s

$\dot{V}$ Volumetric flow rate ($kg/m^3 - s$)

ϵ Coefficient of performance

μ Viscosity ($kg/m - s$)

ρ Density (kg/m^3)

σ Surface tension (N/m)

$\wp$ Power (kPa^2/Hz)

Subscripts

Al Aluminum

b	Bubble
e	Excess
f	fluid
h	Hydraulic
IB	Initiate saturated boiling
in	Inlet
j	Jet
l	Liquid
out	Outlet
sat	Saturation
v	Vapor
w	Wall

Chapter 1 – Introduction

1.1 Motivation

Advances in electronics fabrication, coupled with the demand for increased computing power, has driven the demand for innovative cooling solutions to dissipate waste heat generated by these devices. Though electronics devices have become increasingly miniaturized, their power requirements have not decreased at the same rate. The increased sophistication of control systems used in many consumer and military applications has, correspondingly, required a increase in necessary computing power. Dense arrays of high powered compact devices require modular, stable, and robust cooling solutions to manage the waste heat generated during operation.

1.2 Background

Extensive research has been conducted on technologies capable of managing the high heat flux output of powered devices. One technology is microchannel heat exchangers and heat sinks. In 1981 Tuckerman and Pease [1] published the founding article, on this subject which developed the relationship between the decrease in the channel's hydraulic diameter and the increase in the non-dimensional heat transfer coefficient , Nusselt number, for laminar single phase flows. The Nusselt

number, as a function of the hydraulic diameter,

$$Nu_{D_h} = \frac{hD_h}{k_f} \tag{1.1}$$

where h is the heat transfer coefficient, D_h is the hydraulic diameter, and k_f is the thermal conductivity of the fluid. For fully developed laminar flows, the Nusselt number is a constant value. By examination of Eqn. 1.1, a decrease in the hydraulic diameter results in an increase in the heat transfer coefficient. Subsequently, a wide data base of experimental and numerical research has been compiled on the subject. Initial focus was directed toward single-phase flows through straight parallel channel networks. These geometries resulted in high heat transfer coefficients but, due to the mircoscale channel dimensions, the pressure drop was also very high. Reduction of the pressure drop through these devices was investigated using branching fractal-like channel networks arranged in a radial pattern, which was first introduced by Pence [2]. The fractal-like network is based on scaling laws from mammalian circulatory systems and at each branch there is an increase in the overall cross sectional area. This results in a lower overall pressure drop when compared to an equivalent straight channel design. While single-phase microchannel heat sinks have performance advantages over conventional heat sinks, there are also disadvantages that limit their feasibility. During single-phase operation, the bulk temperature of the working fluid increases as it passes through the microchannels causing axial temperature gradients. The gradients cause thermal stresses in fabricated electronic devices that can lead to failure. High manufacturing costs of microchannel networks also make these devices prohibitive for many applications.

Operating microchannel devices with two-phase flow conditions enables higher heat flux cooling due to the latent energy exchange during boiling, as compared

to single-phase flow. Another advantage to two-phase heat transfer is the bulk temperature of the fluid remains nearly constant, approximately the saturation temperature, throughout the device. This results in a nearly constant wall temperature, minimizing thermal stresses in the fabricated device. While a more robust design option from the perspective of thermal stress failure, two phase devices are prone to another failure mode described as "dry out". Dry out occurs at high heat fluxes when vapor bubbles that form on the channel wall coalesce into a vapor film, covering the channel wall. Dry out can also occur during unstable flow when vapor slugs travel against the direction of flow and prevent fluid from wetting the channel surface. During dry out, fluid is not present on the channel surface to conduct energy and as a result the heat transfer coefficient decreases significantly and the surface temperature increases to the point of device failure.

Another disadvantage to using two-phase flow in microchannel devices is flow instabilities that result from the expansion of the vapor phase in the confined space of the microchannel. Since the vapor phase is several orders of magnitude less dense than the liquid phase, when the working fluid changes phase the vapor must have room to expand. Due to the small hydraulic diameters of microchannels there is only one dimension for this expansion to take place, along the length of the channel. This causes vapor slugs to travel rapidly upstream or downstream depending on the relative flow resistance. The result is pressure oscillations which can lead to flow malidistribution and in extreme cases dry out. Flow maldistribution can cause nonuniform heat transfer and thermal gradients that can contribute to component failure. Research has led to innovative solutions such as tapered channel geometries, engineered nucleation sites, and vapor extraction to minimize these flows instabilities.

Impinging jets are another configuration capable of removing high heat fluxes and have a variety of applications in heat transfer and material processing. Jets have been used extensively to cool metals during forging and casting processes because of their ability to efficiently transfer large amounts of energy. As power densities of electronics devices have increased, impinging jets have been explored as a means of managing waste heat. Fig. 1.1 shows several different jet configurations that can be utilized for specific applications.

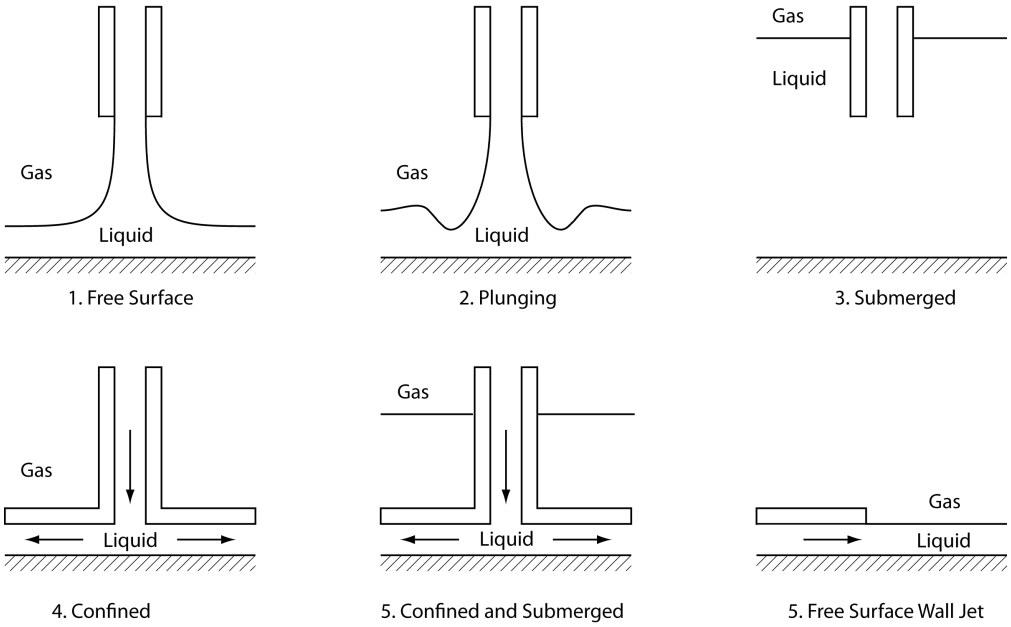

Figure 1.1: Various jet configurations used for heat transfer applications.

The first three configurations result in flow fields that are qualitatively similar and can be explained by examination of the free surface planar jet which discharges into quiescent ambient conditions [3]. As the working fluid leaves the jet nozzle, it is assumed to be turbulent and have a uniform velocity distribution. With increasing distance from the nozzle, momentum exchange with the surroundings causes the boundary of the jet to slow down and therefore broaden. The center of the jet remains at the uniform exit velocity and is termed the potential core.

The length of the potential core for a free jet discharging into ambient conditions is approximately equal to jet height to diameter ratio of $H/D_j \approx 5$ [4]. Outside the length of the potential core, the velocity profile is nonuniform and decreases with increasing distance from the jet nozzle. Exceptions to this generalization can occur for submerged or plunging jet configurations with low jet velocities or large jet heights [3]. Fig. 1.2 illustrates the evolution of the jet discussed above.

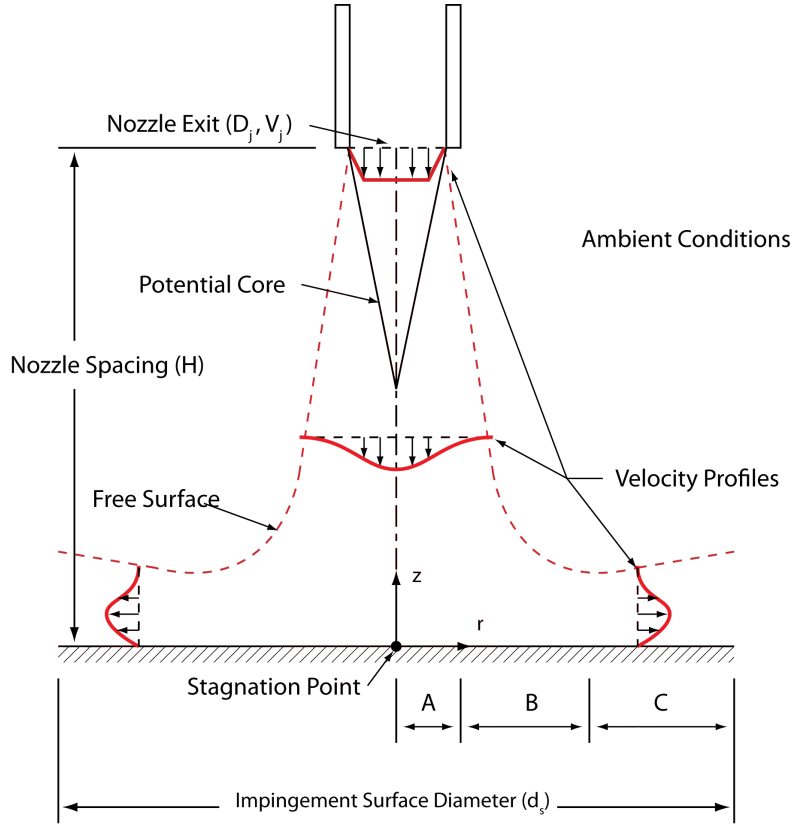

Figure 1.2: Cross section of a free jet discharging into quiescent air and impinging on a solid surface.

Figure 1.2 depicts three flow regions along the impingement surface; the stag-

nation, acceleration and parallel flow regions. At the stagnation point the flow exiting the jet decelerates to zero and therefore is the maximum in local pressure. From the stagnation point the flow accelerates along the wall until it approaches the velocity of the jet while the pressure decreases from the stagnation point value to that of the ambient pressure. The stagnation region, which corresponds to a radial distance of $r/D_j \leq 0.5$, is characterized by a near linear increase in stream-wise velocity. In the acceleration region, $0.5 \leq r/D_j \leq 2$, the stream-wise velocity continues to approach that of the jet velocity. Finally in the parallel flow region, $r/D_j > 2$, the stream-wise velocity, u_∞, reaches a maximum and the influence of the impinging jet is no longer significant [3]. A plot of the stream-wise pressure and velocity distribution as functions of r/D_j is shown below in Fig. 1.3.

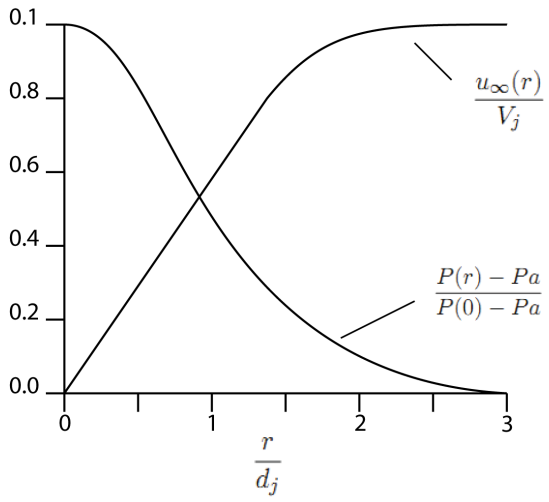

Figure 1.3: Velocity and pressure distributions as a function of radial distance from the stagnation point.

Convection of energy away from the heated surface is proportional to the acceleration of the fluid along the surface. The heat transfer coefficient is at a maximum at the stagnation point and decays with increasing radial distance. For low non-dimensional gap spacing, $H/D_j \leq 5$, there is a second local maximum

associated with an increase in turbulence levels from the transition from the accelerating region to the decelerating wall jet [5]. Based on the previous discussion of jet hydrodynamics, there are several factors influencing the heat transfer performance of single-phase impinging jet flows. Outside the potential core region, the nozzle-to-plate spacing can strongly influence jet performance. Exit velocity and correspondingly the inertia of the jet impacting the heated surface will influence the amount of energy removed. Finally, the characteristics of the working fluid being used, specific heat (c_p), viscosity (μ), density (ρ), and thermal conductivity (k), will also influence heat transfer. These fluid properties and flow conditions can be represented by the non-dimensional Prandtl (Pr) and Reynolds (Re) numbers.

$$Pr = \frac{c_p \mu}{k} = \frac{Viscous\ Diffusivity}{Thermal\ Diffusivity} \tag{1.2}$$

$$Re = \frac{\rho V D}{\mu} = \frac{Inertial\ Forces}{Viscous\ Forces} \tag{1.3}$$

The different jet configurations shown in Fig. 1.1 are all capable of removing large amounts of energy from a heated surface, but for applications that require a compact and manufacturable device the confined jet is a desirable option. As mentioned previously with single-phase cooling in microchannels, significant temperature gradients can develop within the heated device for single-phase impinging jets. Given the requirements discussed for high heat flux cooling with minimal temperature gradients, two-phase impinging jets have become the focus of many research investigations. For the confined jet geometries, the confinement gap restricts the expansion of the vapor phase similarly to microchannels. This leads to flow instabilities and the premature onset of critical heat flux, which will be described in the section below. The potential for these instabilities is still be lower than in

microchannel devices since the expanding vapor phase would only be confined in one dimension and could expand in the radial and theta directions.

Pool boiling is the base two-phase mode of heat transfer that the previously described two-phase geometries seek to improve upon. Since there is no forced convection component to the heat transfer, energy is removed from the heated surface by the formation and departure of bubbles and free convection. As the heat flux increases different modes of boiling occur, these can be illustrated by a representative boiling curve of water at atmospheric pressure show in Fig. 1.4.

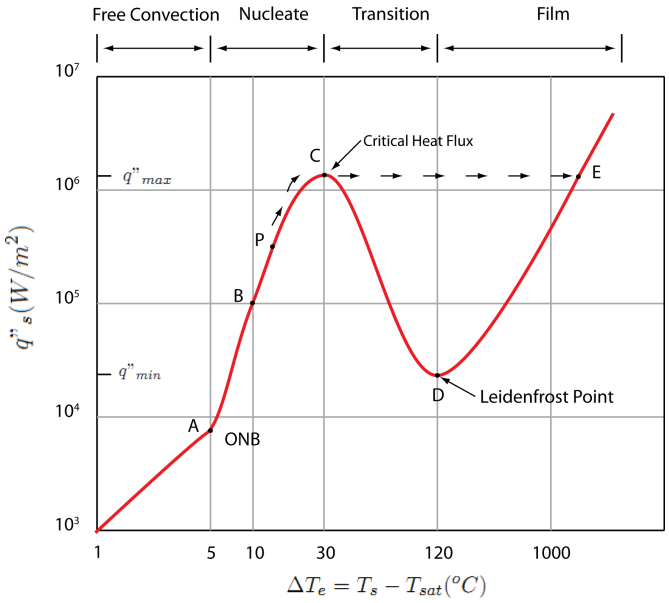

Figure 1.4: Representation of a boiling curve for water at atmospheric pressure.

Initially free convection removes energy from the heated surface until the excess temperature reaches a value where bubbles begin to nucleate. This is referred to as the onset of nucleate boiling (ONB), point A in Fig. 1.4, and occurs at an excess

temperature of approximately $\Delta T_e \approx 5^oC$. The excess temperature

$$\Delta T_e = T_w - T_{sat} \tag{1.4}$$

where T_w is the wall temperature and T_{sat} is the saturation temperature. Once the bubbles form on the surface, they grow until the buoyancy force is greater than the surface tension holding the bubble in place. The bubbles then depart from the surface, removing the energy that was required for formation. Isolated bubble formation occurs between an excess temperature of $5 \leq \Delta T_e \leq 10^oC$ which is represented by points A to B in Fig.1.4. After the bubble departs from the surface, a small amount of vapor is trapped in the nucleation site. This trapped vapor seeds the growth of the next vapor bubble at that site. The process of bubble formation, growth and departure is illustrated by steps 1-4 in Fig. 1.5.

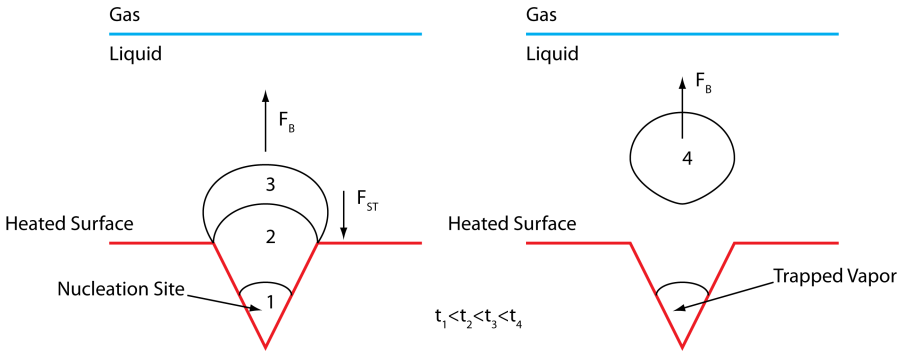

Figure 1.5: Time series of bubble growth and departure from a nucleation site.

As heat flux increases, isolated bubble formation changes into jets and columns until a point of maximum heat flux occurs. This is represented by point C in Fig.1.4 and is termed critical heat flux(CHF). At this point, vapor bubbles coalesce into vapor film that covers the surface causing a significant rise in excess temperature. The nucleate boiling regime, points A to C, is desirable from a heat

transfer perspective because a large change in heat flux corresponds to a small change in excess temperature. Beyond the critical heat flux point there is a jump in excess temperature and a decrease in heat flux, represented by points C to D in Fig. 1.4. This region is called the transition boiling regime and conditions may oscillate between film and nucleate boiling [4]. At point D, the Leidenfrost point, an insulating layer of vapor forms over the heated surface and is called dry out. Once the vapor layer forms, film boiling occurs where heat is removed through the surface by conduction and radiation through the vapor film. For a device operating with an increasing heat flux output, when the point of critical heat flux is reached there would be a jump between points C to E on the boiling curve. As can be seen from Fig. 1.4, this would result in dramatic increase in surface temperature and result in device failure. Accurate prediction of the inception of critical heat flux and understanding of flow instabilities are important for operating high heat flux devices with two phase cooling.

Examining the three heat transfer configurations described above, the most advantageous cooling device would have the highest performance for the lowest cost. As a pool of water sitting on a heated device is not a reasonable configuration to package for a cooling device, so pool boiling will be disregarded in the following performance discussion. Performance for heat transfer devices can be measured by the amount of energy capable of being removed and the cost associated is the pumping power required to drive fluid through the device. The coefficient of performance

$$\epsilon = \frac{q'' A}{\Delta P \dot{V}} \tag{1.5}$$

where q" is the heat flux, A is the heat transfer area, ΔP is the pressure drop, and $\dot{V}$ is the volumetric flow rate. Microchannel devices are capable of removing signif-

icant amounts of energy because of their high heat transfer coefficients and large surface areas due to the high number of channels that can be fabricated in a single device. While this is advantageous for heat transfer, the associated pressure drop is also large because of the microscale channel dimensions. Microchannel and impinging liquid jets were compared by Lee and Vafai [6] and it was determined that with proper treatment of spent fluid, impinging jet configurations could achieve similar performance to microchannel networks. Two-phase jet geometries are able achieve high heat fluxes but the heat transfer area, for a similarly size device microchannel device, is smaller since there are no channel walls present. Because there are no channel walls, the pressure drop through the device is smaller. Ultimately, the use of an appropriately designed jet geometry could yield a coefficient of performance on par with that of microchannels while reducing some of the flow instabilities that occur during two-phase operation.

Chapter 2 – Literature Review

2.1 Single-Phase Jets

The examination of literature concerning single-phase jets is divided into three sections: free jets, submerged jets, and confined jets. The purpose is to illustrate the hydrodynamic and heat transfer characteristics of each configuration and the parameters that influence their performance.

2.1.1 Free Jets

Martin [5] collected previous experimental results for free jets and developed empirical correlations for the purpose of engineering applications. Results were summarized from experiments using single round nozzles, arrays of round nozzles, single slot nozzles, and arrays of slot nozzles. Using these results, a fundamental understanding of impinging flow hydrodynamics and the three characteristic flow regions, shown in Fig. 1.2, was described. Correlations were presented to calculate potential core lengths, boundary layer thickness, and average Nusselt numbers for the various configurations described previously. Additionally optimization for jet nozzle spacing in arrays and the factors influencing heat transfer are analyzed. For single round nozzles the Martin [5] correlation is widely used to estimate the average Nusselt number in gaseous and single-phase liquid flows for engineering design purposes. A detailed discussion of this correlation is presented in section 4.1. The empirical correlations developed in this work are still used today in research and

industry to perform design calculations and as a reference for free jet impingement.

2.1.2 Submerged Jets

Single-phase jet impingement heat transfer is covered in depth by Webb et al. [7], focusing on free and submerged configurations for axisymmetric and planar geometries. An examination of previous experimental and theoretical results allowed the determination of factors that influence heat transfer for impinging liquid jet flows. A review of theoretical work for laminar planar and axisymmetric jets develops the relationship for the stagnation region Nusselt number from the solution of a special case of the Faulkner-Skan(F-S) equation [7]. A simplified result for stagnation Nusselt number for impinging jet flows,

$$Nu_{d,0} = CRe_d^m Pr^n \tag{2.1}$$

which is presented as a generalized stagnation correlation with variables C, m, and n that are determined for specific flows. The analytic laminar solution to the F-S equation give the exponent of the Reynolds number m equal to 0.5. Although many of the works examined are for turbulent exit conditions, this relationship is maintained. Experimental results using a variety of fluids and jet configurations are examined, with a focus on submerged jet studies with similar conditions to the current research. These works are presented in Table 2.1 for ease of reference.

Table 2.1: Experimental submerged liquid jet heat transfer studies reviewed by Webb et al. [7].

Authors	Fluid	Nozzle Diameter (d_j)	Re_D	z/D_j	Configuration
Besserman et al. [8]	FC-77	4.4 - 9.3 mm	1000-40,000	0.5-5	Conf.
Besserman et al. [9]	FC-77	4.4 ,9.3 mm	1000 - 40,000	1-5	Conf.
Chang et al. [10]	R-113	4.0 mm	9500-110,000	1.5 - 4	Conf.
Elison and Webb [11]	Water	0.25-0.58 mm	300-700	0.1 - 40	Sub. &F-S
Ma and Bergles [12]	R-113	1.1 mm	2500-29,000	1.5 - 21	F-S
Garimella and Rice [13]	FC-77	1.6, 3.2 mm	8500 - 23,000	1-10	Conf. &Sub.
Smirnov et al. [14]	Water	2.5 - 36.6 mm	16,000 - 50,000	0.5 - 10	Sub.
Sun et al. [15]	Water	1.0mm	5100-21,000	1-20	Sub.
Womac et al. [16]	Water	0.46 - 6.6 mm	200 - 50,000	0.25 -20	Sub.
Womac et al. [17]	FC-77	0.46 - 6.6 mm	200 - 50,000	0.25 -20	F-S

Based on the reviewed works listed in Table 2.1, Webb et al. [7] divides the analysis of the results into three regions of influence: influence of nozzle-to-surface spacing, influence of Reynolds number, and influence of Prandtl number. For submerged jets, the heat transfer is more sensitive to the nozzle-to-surface spacing than free-surface jets, particularly if the spacing is greater than length of the potential core. Inside the potential core the heat transfer is weakly affected by the nozzle-to-surface spacing, with a maximum in heat transfer at an $H/D_j \approx 5$. This increase in heat transfer can be attributed to an increase in turbulence generated by the jet interacting with the ambient surroundings [18]. With increasing distance from the nozzle exit, beyond the potential core, the jet velocity continues to decrease inversely proportional to H/D_j. As a result, the stagnation Nusselt number is inversely proportional to the square root of the ratio of the jet to surface spacing. The expression for the stagnation Nusselt number outside the potential core for a submerged jet is given by

$$Nu_{d,0} = Nu_{d,0,max} \left[\frac{(H/D_j)_p}{(H/D_j)} \right]^{1/2} \tag{2.2}$$

where $Nu_{d,0,max}$ is the maximum Nusselt number at the end of the potential core, denoted by $(H/D_j)_p$. At Reynolds numbers below $Re_D = 800$, the Nusselt number may be independent of the nozzle-to-surface spacing according to experimental results by Elison and Webb [11]. This can be attributed to the destabilization of the laminar jet as it issues in to the environment. As the jet destabilizes, there is a decrease in the centerline velocity and an increase in turbulence. The result is a near constant stagnation Nusselt number which is insensitive to nozzle-to-surface spacing.

The influence of the Reynolds number on impinging liquid flows has been in-

vestigated in several of the works listed using a variety of working fluids. The exponent m in Eqn. 2.1 was experimentally determined for different fluids to be 0.5 [12, 15]. These experimental results exhibit the same square root dependence on the Reynolds number that was derived using laminar solution to impinging jet flows discussed previously. This can be explained by the favorable pressure gradient that tends to laminarize the flow in the stagnation region, $r/D_j \leq 0.5$. This results in the formation of a laminar boundary layer [7]. For low Reynolds number flows ($Re_D \leq 800$), the dependence on the Reynolds number is stronger. For these low Reynolds number cases, values for m, in Eqn. 2.1, were suggested to be $0.70 \leq m \leq 0.8$ [11]. This is again due to the destabilization of the jet as it issues into the stagnant surrounding fluid.

The influence of Prandtl number was examined by Martin [5] and the exponent n, in Eqn. 2.1, was found to be 0.42. This is based on experimental work using impinging jet flow of air and water. The relationship was experimentally confirmed for submerged jet flows using water [11, 14–16], R-113 [10, 12], and FC-77 [13, 16]. For large Prandtl number fluids, the exponent n was reported to have a value of $n = 1/3$ [7].

Transition to turbulence, in the radial flow region, was reported by investigators and is another factor that can influence the local and average heat transfer coefficients [15]. The inflection point, or local maximum, occurs at a location corresponding to $r/D_j \approx 2$. This behavior was also observed for studies using submerged turbulent air jets [18] and for confined submerged liquid jets [19]. The influence of confinement was reported to enhance the magnitude of the secondary peaks in local heat transfer coefficient and are discussed in greater detail in the following section.

2.1.3 Confined Jets

Confined impinging liquid jets require an additional examination of literature due to the influence of the confinement surface on the hydrodynamics and heat transfer of the impinging flow. Chang et al. [20] examined confined submerged impinging jet flows of R-113. Stagnation point Nusselt numbers and local average Nusselt numbers were determined as a function of Reynolds number and the nozzle-to-surface spacing. The influence of the confinement gap on the impinging flow was to induce a recirculation vortex, the size and intensity of which is dependent on the gap spacing and inertia of the impinging jet. The resulting correlations for stagnation point and local average Nusslet numbers are presented in Eqn. 2.3 - 2.5 .

$$Nu(0) = 0.660 Re_j^{0.574} Pr^{0.4} (z/d_j)^{-0.106} \tag{2.3}$$

$$\overline{Nu}(r)/Nu(0) = [1 + 0.1147(r/d_j)^{1.81}]^{-1};\ r/d_j \geq 1.25 \tag{2.4}$$

$$\overline{Nu}(r)/Nu(0) = 1.0632(r/d_j)^{-0.62};\ r > 1.25 \tag{2.5}$$

The results of the heat transfer data show a slight decrease in the stagnation Nusselt number for gap spacing that falls within the length of the potential core for unconfined flows. As discussed previously, the stagnation Nusselt number is constant for free-jets within the length of the potential core. The decrease in stagnation Nusselt number was attributed to the recirculation vortex which causes the emerging jet to break up prematurely. The existence of these recirculation vortices were also noted independently by Garimella and Rice [19] and were thought to enhance secondary peaks in the heat transfer coefficient.

Garimella and Rice [19] used laser-Doppler velocimetry to examine the recircu-

lation zones for a jet of FC-77 with nozzle diameters of 6.35 mm and 3.18 mm, gap spacings (H/D_j) of 2, 3 and 4, and Reynolds numbers of 8500, 13,000 and 23,000. The recirculation zones were found to be a function of both nozzle-to-surface spacing and Reynolds number. With increasing Reynolds number the center of the vortex moved radially outwards and nearer to the impingement surface.

An increase in nozzle-to-surface spacing accomplished the same result as an increase in the Reynolds number, to move the center of the vortex radially outwards. Further influences of the confinement surface was an increase in peak turbulence levels for smaller (H/D_j) ratios. The location of transition to turbulence in the wall jet region also moved radially outwards with increasing (H/D_j) ratios. Secondary peaks in the heat transfer became more pronounced for smaller (H/D_j) ratios but their location occurred at a further radial position than the transition to turbulence [19].

Additional studies have been conducted to assess the influence of nozzle geometries on confined liquid jet impingement heat transfer [21]. Using nozzles with different diameters and aspect ratios (L/D_j), the effects of flow development and separation on the heat transfer coefficient were examined. For very small L/D_j ratios, heat transfer coefficients were at a maximum. Aspect ratios from $1 \leq L/D_j \leq 4$, showed a sharp decrease in the heat transfer coefficient. With a further increase to $4 \leq L/D_j \leq 8$, the heat transfer coefficient gradually increased. The cause of these trends was thought to be due to flow separation and reattachment in the nozzle and its influence on the exit velocity profile [21]. An increase in the nozzle diameter showed a substantial increase in the stagnation heat transfer coefficient, for a fixed Reynolds number, L/D_j, and H/D_j. Turbulent intensity near the jet centerline increasing with larger jet diameters was postulated as the reason for this

increase in the heat transfer coefficient.

Influence of thermophysical properties on heat transfer in confined liquid impinging jet heat transfer was investigated using air, water and FC-77 [22]. As was found in the discussion of the previous work by Garimella et al. [21], there was a distinct relationship between nozzle diameter and the heat transfer that was not captured by the Nusselt number non-dimensionalization, which was also reported in this work. Correlations were developed for the stagnation and area-averaged Nusselt numbers as a function of the Reynolds number, Prandtl number, orifice aspect ratio, and effective source to orifice ratio. The exponent for Prandtl number was experimentally determined to be 0.441 instead of constraining the value to the 0.4 used in previous works by the authors.

For the current experimental configuration, confined impinging jet of subcooled water, there are several parameters that influence heat transfer performance. Fluid properties as well as inertia of the exiting jet, captured by the non-dimensional Prandtl and Reynolds numbers, will influence the amount of energy removed from the heated impingement surface. Due to the confinement of the current geometry, recirculation vortices exist within the wall jet region and cause enhanced secondary peaks in local heat transfer for small nozzle-to-surface spacing.

2.2 Two-Phase Jets

As noted by an assessment of current high heat flux cooling technologies by Mudawar [23], achieving the heat flux demands of future power devices will require the use of phase change cooling in a variety of configurations tailored to specific devices. Jet impingement boiling is reviewed by Wolf et al. [3] for a variety of

jet configurations, working fluids, and regions of the boiling curve. Two particular points of interest that were discussed in the background section are the onset of nucleate boiling (ONB) and critical heat flux (CHF). ONB is necessary for increased heat transfer due to latent heat of vaporization and CHF is the limit for device operation. Understanding the parameters that affect these points on the boiling curve are necessary to design and safely operate a two-phase heat transfer device. While Wolf et al. [3] examines free-surface, submerged and confined jet configurations, this discussion will focus on the submerged and confined experiments that relate to the current research. A list of the relevant works concerning nucleate boiling reviewed by Wolf et al. [3] are listed in Table 2.2 for ease of reference.

Table 2.2: Experimental two-phase jet nucleate boiling(NB) and critical heat flux(CHF) studies reviewed by Wolf et al. [3]

Authors	Jet Type	Fluid	$\Delta T_sub(^oC)$	V_{jet}(m/s)	D_j(mm)	H (mm)	Study
Kamata et al. [24]	Cir.-Conf.	Water	0	10 - 17	2.2	0.3 - 0.6	NB, CHF
Kamata et al. [25]	Cir.-Conf.	Water	0	10 - 17	2.2	0.3 - 0.6	NB, CHF
Katto and Kunihiro [26]	Cir.- Conf.	Water	< 3	5.3 - 60	2	30	NB, CHF
Ma and Bergles [27]	Cir. - Sub.	R-113	0 - 20.5	1.08 - 10.05	1.07 -1.81	2.14 -3.62	NB, CHF
McGillis and Carey [28]	Cir.- Conf.	R-113	11.5 - 30	2.75 - 3.08	1.0	1.0	NB, CHF
Monde and Furukawa [29]	Cir.- Sub.	R-113	< 2	1 - 4	1.1	5	NB, CHF
Monde and Katto [30]	Cir. - Conf.	Water	0	8.0 - 17.3	2.0 -2.5	0.3 - 0.5	NB, CHF
Mudawar and Wadsworth [31]	Plan.- Conf.	FC-72	10 - 40	1 - 11	0.127 - 0.254	5.08	NB, CHF
Wadsworth and Mudawar [32]	Plan.- Conf.	FC - 72	10	5	0.254	5.08	NB, CHF

2.2.1 Nucleate boiling

Nucleate boiling literature can be divided into four major categories: jet velocity, subcooling, nozzle and heater dimensions, and nozzle-to-surface spacing. The works reviewed by Wolf et al. [3] will be discussed and augmented with recent articles on submerged and confined jets in the nucleate boiling regime.

Influence of jet velocity was investigated by Katto and Kunihiro [26] for nucleate boiling of a submerged circular jet of saturated water. The ratio of heat flux to surface temperature was shown to be unaffected except to extend the boiling curve to higher values of heat removal and surface temperature than that of pool boiling. Higher jet velocities also served to delay the incipience of nucleate boiling. This results was also reported by Ma and Bergles [27] for a circular submerged jet of saturated R-113. A highly confined circular impinging jet of saturated water was investigated by Monde and Katto [30], wherein jet velocity was found to have little influence on the nucleate boiling regime. Confinement heights for this experiment were 0.3 and 0.5 mm with jet diameters of 2.0 and 2.5 mm and jet velocities that ranged from 8.0 to 17.3 m/s. Additional studies with confined jets of water were performed by Kamata et a.l [24,25] and with FC-72 by Mudawar and Wadsworth [31], all reported a similar result of insensitivity to the relationship of heat flux to surface temperature as a function of the jet velocity in the nucleate boiling regime. The heat transfer in the nucleate boiling regime is dominated by the intense mixing of vapor bubbles leaving the heated surface, jet velocity was found to influence the subcooled and partial boiling regimes [33].

The influence of subcooling on boiling heat transfer was examined by Ma and Bergles [27] and was found to delay the incipience of nucleate boiling and slightly shift the boiling curve to the left, see Fig. 1.4. Mudawar and Wadsworth [31]

reported the same result for the delay of incipience of nucleate boiling but found no change in the nucleate boiling region for an increase in subcooling. The influence of subcooling, in a subcooled impinging free-surface water jet, was examined by Lui et al. [34] and was also found to delay the incipience of nucleate boiling but did not affect the full nucleate boiling regime. Additionally the influence of nozzle diameter was investigated for saturated water by Katto and Kunihiro [26], FC-72 by Wadsworth [32], and for a highly confined jet of water by Monde and Katto [30]. The result was the nucleate boiling relationship between heat flux and surface temperature was found to be insensitive to changes in jet nozzle diameter.

Kamata et al. [25] examined the influence of nozzle-to-surface spacing for confined jets of water with spacing ranging from 0.3 to 0.6 mm. It was determined there is no dependence on the stagnation point Nusselt number, in the nucleate boiling regime, as a result of changes in nozzle-to-surface spacings. This result was also reported for another confined jet water study performed by Monde and Katto [30].

Two-phase flows of R-113 in a confined and submerged jet configuration were investigated by Chang et al. [35] to determine the influence of Reynolds number, inlet quality, and nozzle-to-surface spacing. As reported in previous works, changes in Reynolds numbers and nozzle-to-surface spacing were found to have no influence on the ratio of heat flux to surface temperature. The inlet quality of the jet was found to greatly influence the heat transfer and was accounted for in the proposed correlation. Further experiments were performed by Zhou et al. [36] for submerged impinging jets of R-113. Again the nozzle exit velocity and subcooling were found to have no effect on the nucleate boiling regime. This was attributed to a negligible influence of jet exit velocity on the formation, growth, and departure of vapor

bubbles.

Summarizing the results analyzed, nucleate boiling is unaffected by changes in nozzle exit velocity, nozzle-to-surface spacing, nozzle dimensions, and subcooling. Variation of these parameters serves only to delay the incipience of boiling and extend the nucleate boiling regime to higher values of heat flux and excess temperature.

2.2.2 Critical Heat flux

The influence of jet parameters such as jet velocity, nozzle-to-surface spacing, nozzle dimension, and subcooling on critical heat flux were also examined by Wolf et al. [3]. The relevant experimental studies for critical heat flux reviewed by Wolf et al. are shown in Table 2.2. The influences of exit velocity, subcooling, and nozzle-to-surface spacing on critical heat flux are described below.

Katto and Kunihiro [26] used submerged and plunging jets of saturated water with exit velocities ranging from 1 - 3 m/s to explore the influence on critical heat flux. A linear relationship between CHF and jet velocity was reported but was also shown to be a function of the nozzle-to-surface spacing and pool heights. This linear relationship was not substantiated by any of the other works examined and a cube root relationship was most often reported [3]. The comparison of submerged to plunging jet data showed the submerged cases yielded the highest values of CHF. Monde and Furukawa [29] also investigated the relationship between jet velocity and CHF for submerged and plunging jet configurations. Results indicate a small influence of jet velocity for plunging configuration but for the submerged cases there was no effect. In their results, the submerged jet cases also resulted in the

highest CHF values.

Ma and Bergles [27] investigated CHF for a circular jet of R-113 with exit velocities ranging from $1.08 \leq V_j \leq 2.72 m/s$. Although the data presented was minimal, the basic trends showed a cube-root dependence for CHF. This result was replicated by Zhou et al. [36], also using flows of R-113 with exit velocities ranging from $0.32 \leq V_j \leq 2.08 m/s$. A highly confined impinging saturated water jet was examined by Kamata et al. [24,25] and was found that for a nozzle-to-surface spacing of 0.3 mm the CHF increased by 43% for an increase in jet velocity from 10 to 17m/s. Mudawar and Wadsworth [31] used a confined planar jet of FC-72 with jet velocities ranging from 1-13m/s, to show the dependence of CHF on velocity for varying nozzle-to-surface spacings. For high velocity cases, a decrease in gap spacing caused a decrease in CHF. This was attributed to a decrease in local subcooling from the confined high velocity flow along the wall that prevented vapor bubbles from mixing with the bulk fluid stream. An experimental study by Inoue et al. [37] reported an increase in CHF values with an increase in jet velocity for subcooled water in a planar jet geometry. Mitsutake and Monde [38] experimented with subcooled water impinging on a heated surface with high system pressures up to 1.3 MPa. CHF was explored using variable heater lengths, heat thicknesses, subcooling, and jet velocities. Jet velocity was found to increase CHF for each heater thickness, length, and degree of subcooling tested. Overall it was reported that CHF increases with an increasing jet velocity, with many investigators reporting a cubed root relationship [3].

The influence of subcooling on CHF were reported by Mudawar and Wadsworth [31] for a confined planar jet with subcoolings ranging from 0-40^oC, which showed an increase in CHF for an increase in subcooling. In the same work, the effect

of nozzle diameter was explored and it was determined that an increase in nozzle diameter results in an increase in CHF for a fixed Reynolds number. Ma and Bergles [27] also reported an increase in CHF by 30 to 80% for subcooling values ranging from 11.5 to 29.5^oC. Inoue et al. [37] also reported an increase in CHF with increased subcooling from 20-80^oC for a planar water jet, but did not quantify the relationship. Mitsutake and Monde [38] controlled subcooling, 80-170^oC, by increasing the system pressure of their experimental apparatus. An increase in CHF was observed for increased subcooling, and therefore system pressure, with other testing parameters held constant. This result of increased CHF for increasing subcooling was also observed by Liu et al. [34] for subcooled water at ambient pressures.

The final parameter explored was nozzle-to-surface spacing and its influence on CHF. Katto and Kunihiro [26] found the highest values of CHF resulted from the smallest H/D_j ratios for a circular submerged jet of saturated water. The highly confined saturated water study performed by Kamata et al. [24, 25] found a 36% increase in CHF for a nozzle-to-surface spacing of $H/d_j = 0.18$ over the larger spacing of $H/d_j = 0.27$. Mudawar and Wadsworth [31] reported the opposite effect for a confined planar jet of FC-72, at high jet velocities CHF was decreased for small H/D_j ratios. For slower velocity cases, a weak dependence of CHF on nozzle-to-surface spacing was observed. Shin et al. [39] also reported a decrease in CHF for an $H/W = 1.0$ in a confined planar jet, with a width of W, using a dielectric working fluid, as compared to nozzle-to-surface spacing of $H/W = 0.5$ and $H/W = 4.0$. Increased values of CHF at the smallest spacing, $H/W = 0.5$, was explained by increased turbulent mixing resulting from the recirculation zones due to the confinement. Also CHF increased for the spacing of $H/W = 4.0$, over

the $H/W = 1.0$, since the increased spacing allowed for bubbles to travel away from the heated surface and more easily mix with the bulk fluid stream. This effect is more pronounced at higher mass flow rates, which suggests there is an optimal spacing for a given mass flow rate to achieve maximum CHF.

In summary, critical heat flux is effected by nozzle exit velocity, subcooling, nozzle diameter, and nozzle-to-plate spacing. Increased nozzle exit velocities, nozzle diameters, and subcooling correspond to an increase in CHF. Reports on the effects of nozzle-to-surface spacing are conflicting as to how it relates to CHF. This would indicate that the effect of nozzle-to-surface spacing is coupled with other flow parameter.

2.3 Pool Boiling

The basic modes of pool boiling and a representative boiling curve of water at atmospheric pressure were presented in Fig.1.4. This section will examine relevant literature for the evaluation of pooling boiling correlations and factors that influence pool boiling heat transfer. As presented by Incropera [4], the standard form of Nusselt number for pool boiling correlations

$$\overline{Nu_d} = CRe_d^m Pr^n \tag{2.6}$$

where the constants C, m, and n are determined experimentally. For nucleate pool boiling, bubbles rise and mix the surround fluid so an appropriate length scale is the bubble diameter D_b. The departure diameter of the bubble can be determined

by a balance of the buoyancy and surface tension forces, as depicted in Fig.1.5.

$$D_b \propto \sqrt{\frac{\sigma}{g(\rho_l - \rho_v)}} \tag{2.7}$$

where g is the gravitational constant, ρ_l andρ_v are the liquid and vapor densities, σ is the surface tension, and D_d bubble departure diameter. A characteristic velocity for the perturbation of the liquid is found by dividing the distance liquid must travel to fill the void left by a departing bubble by the time between departures, t_b. The time, t_b, is equal to the energy it takes to form a vapor bubble divided by the rate heat is added to the solid-vapor contact area [4]. This results in the following expression

$$V \propto \frac{D_b}{t_b} \propto \frac{D_b}{\left(\frac{\rho_l i_{lv} D_b^3}{q"_s D_b^2}\right)} \propto \frac{q"_s}{\rho_l h_{lv}} \tag{2.8}$$

Substituting Eqns. 2.7 and 2.8 into Eqn. 2.6, absorbing the proportionality into the constant C, and finally substituting the resulting expression into Newton's law of cooling, the following expression for heat flux as a function of the excess temperature, derived by Rohsenow [40], is arrived at

$$q"_s = \mu_l h_{fg} \left[\frac{g(\rho_l - \rho_v)}{\sigma}\right]^{1/2} \left(\frac{c_{p,l}\Delta T_e}{C_{s,f} i_{lv} Pr_l^n}\right)^3 \tag{2.9}$$

where the coefficient $C_{s,f}$ and the exponent n depend on the surface-fluid combination and are experimentally determined. Experimental studies by Pioro [41] evaluated these constants for four working fluids (water, ethanol, R-113, and R-111) and four surface materials (copper, aluminum, brass, and stainless steel) for a variety of heat fluxes and system pressures.

The properties of the heated surface greatly influence the onset of nucleate

boiling and the excess temperature required for bubble growth. Hsu [42] developed a model to predict the range of sizes for active nucleation sites. The model can be extended to predict the incipience of boiling for a given cavity size. The theoretical models were consistent with existing experimental data.

Van Carey [43] reviewed correlations and experimental work relating to bubble departure frequency. The correlations were developed from experimental work using high speed images to estimate the departure size and frequency of bubbles leaving the heated surface. The departure Bond number is the most common non-dimensional number, which incorporates the bubble departure diameter, present in these correlations and is defined as

$$Bo_d = \frac{g(\rho_l - \rho_v)d_d^2}{\sigma} \tag{2.10}$$

Cole [44] proposed the following relationship between the departure Bond number and the Jakob number as a means of calculating the bubble departure diameter

$$Bo_d^{1/2} = 0.04Ja \tag{2.11}$$

where the Jakob number is defined as

$$Ja = \frac{\rho_l c_{pl}[T_w - T_{sat}(P_\infty)]}{\rho_v i_l v} \tag{2.12}$$

The bubble departure size can then be related to the departure time through the correlation proposed by Novak and Zuber [45]. This correlation was developed

through an analogy between the bubble release and natural convection.

$$f d_d = 0.59 \left[\frac{\sigma g(\rho_l - \rho_v)}{\rho_l^2} \right]^{1/4} \tag{2.13}$$

These correlations allow for the calculation of an approximate bubble departure size and frequency for a given system.

2.4 Stability

Flow instabilities can be classified as either static or dynamic and occur depending on the conditions present in the two-phase system. Static instabilities occur when flow conditions change in a small step from the original steady-state and another steady-state is not possible in the vicinity of the original state [46]. A static instability can either lead to a different steady-state condition or to a periodic behavior [47]. Dynamic instabilities affect a flow if inertia and other feedback effects have an essential part in the process [46]. According to Tong and Tang [46], there are three criteria that must be met for instabilities to occur:

1. Given certain external parameters, the system can exist at more than one state.
2. An external energy source is necessary to account for frictional dissipation.
3. Disturbances that can initiate the oscillations must be present.

A detailed analysis of static and dynamic flow boiling instabilities was presented by Boure et al. [47] which describes the different types of instabilities and the associated mechanisms that cause them. Three parameters were examined and their effects on instabilities were observed. The parameters are as follows:

1. Geometry - channel length, size, inlet and exit restrictions, single or multiple channels.
2. Operation Conditions - pressure, inlet subcooling, mass velocity, power input, forced or natural convection.
3. Boundary Conditions- axial heat flux distribution, pressure drop across channels.

Given a specific set of operating parameters, the resulting flow instability can effect the heat transfer from the heated surface and prematurely facilitate the onset of critical heat flux. This work gives examples of instabilities for common heat transfer configurations as well as the mathematical tools for their prediction. Two-phase flows offer significant heat transfer improvement over single phase flows but the existence of flow instabilities imposes significant limitations on practical application. Mitigation of these flow instabilities enhance the heat transfer potential of two-phase cooling systems. Limited research into flow instabilities exist for confined geometries. Recently more attention has been focused on instabilities in microchannel and minichannel configurations and a review of the relevant works in this area is presented.

In 2002 Kandlikar [48] noted in a review of existing literature that current research and numerical correlations do not account for the existence of two-phase flow instabilities. Further experimental studies and examination of existing experimental data allowed Kandlikar [49] to develop two non-dimensional numbers, K_1 and K_2, that relate forces due to surface tension, momentum change during evaporation, viscous shear and inertia during flow boiling.

$$K_1 = \left(\frac{q}{Gi_{lv}}\right)^2 \frac{\rho_l}{\rho_v} \tag{2.14}$$

$$K_2 = \left(\frac{q}{i_{lv}}\right)^2 \frac{D}{\rho_v \sigma} \tag{2.15}$$

These non-dimensional numbers, in conjunction with the Weber and Capillary numbers, were thought to be a better tool for analyzing experimental data and developing more representative models. A discussion of flow instabilities is presented but not their relation to the new non-dimensional numbers. Balasubramanian and Kandlikar [50] investigated instabilities and flow patterns in parallel minichannels with a hydraulic diameter of 333 μm using deionized water as the working fluid. A combination of pressure drop measurements and flow visualization was utilized. Using a discrete Fourier transform, the dominant frequencies of the pressure oscillations were analyzed as a function of the wall surface temperature. It was observed that the frequency increased with increasing surface temperature up to 109^{o}C which indicates increasing bubble nucleation frequency. After 109^{o}C, the frequency showed a decreasing trend that was associated with the formation of slug flow in the channels. The frequencies observed during tested ranged from 1.5 Hz to 2.5 Hz. Flow reversal and dry-out were observed using the flow visualization, but no correlation to the frequency or magnitude of the pressure drop oscillations was made.

Kandlikar et al. [51] developed a method of suppressing two-phase flow instabilities that involves flow restriction at the channel inlet and engineered nucleation sites to prevent instabilities and flow reversal. While this serves to suppress instabilities, the added flow restriction increases the overall pressure drop through the device, which corresponds to an increase in the necessary pumping power. The flow instabilities were observed using the same combination of flow visualization and pressure drop data used in the previous work by Balasubramanian and Kand-

likar [50]. Again the only means of assessing the stability of the flow was through the flow visualization, which was then matched with the experimental data.

Qu and Mudawar [52] observed two types of two-phase instabilities in a parallel microchannel network using water as the working fluid. The first type was pressure drop oscillations that were classified by the boundary between liquid and vapor phase oscillating between the heat sink inlet and outlet. This shows up as large amplitude pressure and temperature fluctuations in the time series data and corresponds to a premature onset of CHF. For the channel configuration tested by Qu and Mudawar, an upstream restriction increased the system stiffness and suppressed the pressure fluctuation instabilities.

The second type of flow instabilities were characterized by feedback between parallel channels. This corresponds to much lower magnitude and random pressure drop and surface temperature oscillations, as compared to the unrestricted pressure oscillation case. While both of these instabilities were observed during testing, their relationship to flow parameters and heat flux were not reported. No criteria for the onset of instabilities or the affect on the boiling performance was discussed by the authors.

Research by Lu and Pan [53] examined stabilization of flow boiling in microchannels by using microchannels with diverging cross sections. The experimental setup used subcoooled water as the working fluid and a test piece with 10 parallel channels that had a mean hydraulic diameter of 120μm, uniform depth of 76μm, and a diverging angle of 0.5^o. By reducing the downstream flow resistance through an increase in cross sectional area, the expanding vapor phase passes smoothly downstream and suppresses instabilities. A stability criteria was developed based on flow visualization and pressure measurements during testing.

They determined that at pressure oscillation equal to 3 kPa, vapor bubbles could flow backward into the inlet plenum. This was used as the criteria for stability and two non-dimensional numbers were used to map various experimental results with the stability criteria. The non-dimensional subcooling and phase change numbers, respectively,

$$N_{sub} = \frac{h_{sub}\nu_{lv}}{i_{lv}\nu_l} \tag{2.16}$$

$$N_{pch} = \frac{Q_c\nu_{lv}}{Wi_{lv}\nu_l} \tag{2.17}$$

where i_{lv} is the latent heat of vaporization evaluated at the system pressure, i_{sub} is the difference between the enthalpy of the saturated liquid i_l and the enthalpy of the subcooled inlet fluid h_{in}, Q_c is the heat transfer rate into the channel bottom and side walls, W is the total mass flow rate into all the channels, and ν_{lv} is the difference between the specific volume of the saturated vapor and liquid phases. The 3 kPa pressure oscillation that causes flow reversal in the parallel channels corresponds to values of N_{pch}=370 from N_{pch}=400. The stability criteria is independent of the subcooling number. Additionally Lu and Pan [53] pointed out that except for the square term in Kandlikar's [51] K_1, Eqn. 2.14, it is essentially equivalent to the phase change number, N_pch.

While the non-dimensional numbers account for changes in fluid properties, mass flow rate, and heat input, the stability criteria of 3 kPa was developed for a specific channel geometry. Since there are no channel dimension parameters in the non-dimensional numbers used by Lu and Pan [53], it is difficult to apply this stability criteria to different experimental configurations.

In-situ vapor extraction has also been investigated as a means for mitigation of flow instabilities in two-phase systems. Salakij et al. [54] proposed a model to

predict the results of using vapor extraction in microchannels that have an upper wall that is a hydrophobic permeable membrane. By applying a negative pressure to the reverse side of the membrane, the vapor is extracted while the liquid phase remains in the channel. This allows for the void fraction, volume ratio of liquid to vapor, to be effectively lowered while still retaining the higher heat transfer through latent energy exchange. By removing the vapor phase as it is generated, the instabilities associated with the formation and expansion of the vapor are thought to be mitigated.

While flow instabilities have primarily been studied in macro and microchannel geometries, the potential of instabilities exist for any geometry that has confining dimensions. For confined jet geometries, the upper confinement surface restricts the expansion of the vapor phase which could lead to flow instabilities. An examination of confined jet stability has not be performed in the literature, so the existence of instabilities and their influence on heat transfer is currently unknown.

Chapter 3 – Problem Statement

Review of current research in flow boiling heat transfer, for compact high efficiency cooling, has shown that microchannel and confined jet geometries offer high heat transfer from a scalable device. Two-phase flows offer superior heat transfer performance compared to single-phase flows, for a comparable device configuration, and near constant wall temperatures minimize thermal stresses in the powered device. Two-phase microchannel investigations have shown that flow instabilities can limit the performance of these devices. Research has proven two-phase flow instabilities can be suppressed through the use of tapered channels, upstream flow restrictions, or vapor extraction. Stability of two-phase confined jet geometries has not been studied and could be an alternative configuration for compact stable high heat flux cooling.

3.1 General Hypothesis

From previous research, tapered microchannel geometries mitigate flow instabilities by reducing the downstream flow resistance to the expanding vapor phase. Due to the radial expansion of the working fluid in the current confined jet geometry, flow instabilities that limit straight microchannel performance, are hypothesized to also be suppressed. While a confined jet geometry has less convective surface area than a microchannel array with the same footprint, the jet could be operated at much higher exit qualities due to the reduction of flow instabilities. Also the pressure drop through the device is much less for a comparable microchannel array,

so the performance index, defined in Eqn. 1.5, of the device could be on par with that of the microchannel array. Based on the expanding radial geometry and the decreased device pressure drop, confined jets could be a stable and viable alternative to microchannel devices for high heat flux cooling applications.

3.2 Experimental Objectives

The performance and stability of the confined subcooled water jet will be evaluated for a variety of heat fluxes, inlet mass flow rates, and nozzle-to-surface spacings in both the single-phase and two-phase regimes. The performance will be quantified by calculation of boiling curves, heat flux, q'', versus excess temperature, T_e. These results will be compared to pool boiling correlations, single-phase, and two-phase confined jet correlations. As seen in previous investigations, in the nucleate boiling regime, the boiling curves for the current impinging jet geometry are expected to approach those for pool boiling. This will allow the use of a pool boiling correlation to be modified and superimposed with a single-phase correlation to predict the results of the current testing . Validation of data was accomplished by setting up a pool boiling experiment, with the current experimental device, and comparing the results to the appropriate correlation.

Examination of stability characteristics will consists of frequency and power analysis of inlet pressure time series data. Inlet pressure data is used for this assessment as it has been used in previous research as an indicator of the presence of instabilities. Power spectral densities will be used to analyze the frequency and power of the pressure fluctuation at the different operating conditions. This will illustrate the influence of inlet mass flow rate and nozzle-to-surface spacing on the

magnitude of the pressure fluctuations for a given heat flux. Results will be non-dimensionalized to create a method for comparing data from using different flow conditions and allowing for an indicator of flow instabilities to be determined.

3.3 Tasks

Tasks are split into three sections: validation of experimental results, performance comparison between test cases and with appropriate correlations, and stability analysis. The validation of the surface temperature and heat flux calculations requires the comparison of pool data, taken with the top removed from the current device, with the Rosenhow [40] correlation. Repetitions of this experiment verifies the experimental results match and then the pool boiling correlation is compared with the data. Appropriate constants are evaluated based on this comparison and verified using from the results presented by Pioro et al. [41].

Performance of the confined and submerged water jet is assessed by producing boiling curves for each of the test conditions. Comparison between test cases demonstrate the effect of inlet mass flow rate and gap spacing on the heat transfer performance for a given heat flux. Three single-phase correlations are used to verify that the current experimental results follow expected trends in the single-phase region for changes in mass flow rate and nozzle-to-surface spacing. Using the two-phase impinging jet correlation, modified from Chang et. [35], performance trends for both the single-phase and two-phase regimes are examined. System performance is assessed using the coefficient of performance , ϵ, defined in Eqn. 1.5, and compared to the performance of the tapered microchannel array from Lu and Pan [53].

Finally the stability characteristics of confined and submerged jets are assessed by analysis of high frequency inlet pressure data. Power spectral densities are used to analyze the frequency and power of the oscillations for different test conditions. Plots of the dominant inlet pressure frequency as a function of heat flux are used to demonstrate the influence of inlet mass flow rate and nozzle-to-surface spacing. Instabilities are induced in control cases to examine their characteristics and compare the results to stable flow test cases. These results are non-dimensionalized using the non-dimensional power and Boiling numbers to relate the changes in gap spacing, heat flux, and inlet mass flow rate. These results are compared to the stability and frequency results from existing two-phase literature.

Chapter 4 – Correlation Formulation

From the literature examined previously, appropriate correlations were selected to compare to the present experimental work. Modification was necessary to some of the correlations due to differences in experimental parameters. A discussion of the correlations used for single-phase and two-phase heat transfer, their appropriate range of application, and necessary modification is presented in the following sections. To describe the single-phase and nucleate boiling heat transfer mechanisms the super position principle is used. The total heat flux is

$$q''_{tot} = q''_{1\phi} + q''_{NB} \tag{4.1}$$

where $q''_{1\phi}$ is the single phase contribution and q''_{NB} is the contribution due to nucleate boiling. Using the appropriate temperature differences Eqn. 4.1 can be rewritten as

$$q''_{tot} = h_{1\phi}(T_w - T_b) + h_{NB}(T_w - T_{sat}) \tag{4.2}$$

where T_w is the wall temperature, T_b is the bulk fluid temperature, and T_{sat} is the saturation temperature. Using the correlations discussed in the following section the heat transfer coefficients necessary to evaluate Eqn. 4.2 will be determined.

4.1 Single-Phase Correlations

The Martin [5] correlation

$$\frac{\overline{Nu}}{Pr^{0.42}} = G\left(A_r, \frac{H}{D}\right)\left[2Re^{1/2}\left(1+0.005Re^{0.55}\right)^{1/2}\right] \tag{4.3}$$

where

$$G = 2A_r^{1/2}\frac{1-2.2A_r^{1/2}}{1+0.2\left(H/D-6\right)A_r^{1/2}} \tag{4.4}$$

and

$$A_r = \frac{D^2}{4r^2} \tag{4.5}$$

and

$$\overline{Nu} = \frac{\overline{h}d_j}{k} \tag{4.6}$$

was developed from a review of existing experimental work using impinging gas and single-phase free-jets. It is applicable for a wide range of Reynolds numbers and geometries. The ranges of validity for the correlation are as follows:

$$2000 \leq \quad Re \quad \leq 400,000 \tag{4.7}$$

$$2 \leq \quad H/D \quad \leq 12 \tag{4.8}$$

$$0.004 \leq \quad A_r \quad \leq 0.04 \tag{4.9}$$

Because the current experimental parameters fall within the ranges of validity for this correlation, no modification to the Martin [5] necessary in the current work. This correlation has been widely used in design applications for impinging jets, so it will be used as a comparison to the correlations that are specific to confined and submerged jets.

Li and Garimella [22] examined single-phase heat transfer in a confined and submerged jet configuration using several different working fluids. For each working fluid, a correlation was developed for spatially average Nusselt number. The correlation specific to water is

$$\overline{Nu} = 0.690 Re_j^{0.555} Pr^{0.452} \left(\frac{l}{d_j}\right)^{-0.07} \left(\frac{D_{he}}{d_j}\right)^{-0.346} \tag{4.10}$$

with the experimental limits on parameters listed in Table 4.1. The correlation involves a combination of the Reynolds and Prandtl numbers, as discussed previous in section 2.1.2, to account for the fluid properties and the momentum of the fluid as it impinges on the heated surface. Exponents for the Reynolds and Prandtl numbers were experimentally determined to be 0.555 and 0.452, respectively. Additionally the correlation accounts for the influence of the nozzle length, l, and effective heater diameter, D_{he}. The only experimental condition, in Table 4.1, for the correlation that is not within the range of the current testing parameters is the ratio of nozzle length to the jet diameter, l/d_j. For the current experiment the ratio is 12.7, which is six times larger than the ratio used to develop spatially averaged water correlation by Li and Garimella [22]. For correlations using working fluids other than water, the current l/d_j is within the range tested for validation. All of the spatially averaged correlations use an exponent for the l/d_j equal to -0.07, implying a weak dependence on the nozzle length. Therefore, l/dj should

Table 4.1: Conditions for Li and Garimella correlation [22].

Re_j	$d_j(mm)$	H/D	l/d_j	Fluid	Accuracy
8,500-23,000	1.59-12.7	1-5	2	Water	12.67%

Table 4.2: Conditions for single-phase Chang et al. jet correlation [20].

Re_j	$d_j(mm)$	H/D	Fluid	$q"(W/cm^2)$	Accuracy
9,500-92,000	1-4	1.5-4	R-113	2.3-14.0	20%

not significantly influence the results of the correlation.

Chang et al. [20] developed a single-phase correlation for R-113 in a confined and submerged jet geometry. The correlation is split into three regions based on the radial distance from the stagnation point, which correspond to the flow regions of the impinging jet discussed previously in section 1.2. For the current geometry, the appropriate correlation for the stagnation point is

$$Nu(0) = 0.660 Re_j^{0.574} Pr^{0.4} \left(\frac{H}{d_j}\right)^{-0.106} \tag{4.11}$$

for $\frac{r}{d_j} \leq 1.25$ it is

$$\overline{Nu}(r) = 0.660 Re_j^{0.574} Pr^{0.4} \left(\frac{H}{d_j}\right)^{-0.106} \left(1 + 0.1147 \left(\frac{r}{d_j}\right)^{1.81}\right)^{-1} \tag{4.12}$$

for $\frac{r}{d_j} \geq 1.25$ it is

$$\overline{Nu}(r) = 0.7017 Re_j^{0.574} Pr^{0.4} \left(\frac{H}{d_j}\right)^{-0.106} \left(\frac{r}{d_j}\right)^{-0.62} \tag{4.13}$$

with experimental parameters ranges listed are in Table 4.2. The form of the correlation follows the general Nusselt number equation, Eqn. 2.1, with the addition of terms to account for the nozzle-to-surface spacing and for the ratio of the heated surface diameter to jet nozzle diameter. Exponents on the Reynolds and Prantl

numbers are similar to the values reported by Li and Garimella [22] for a confined and submerged jet, Eqn. 4.10, using water as the working fluid.

4.2 Two-Phase Correlations

Review of two-phase literature indicates that in the nucleate flow boiling regime, for a given working fluid, the relationship between heat flux and surface temperature is similar to pool boiling. This is due to the heat transfer being dominated by the formation and departure of bubbles and the convective contribution being very small. For pool boiling, Rohsenow [40] developed the following correlation, reported previously as Eqn. 2.9 ,

$$q_s'' = \mu_l h_{fg} \left[\frac{g(\rho_l - \rho_v)}{\sigma} \right]^{1/2} \left(\frac{c_{p,l} \Delta T_e}{C_{s,f} i_{lv} Pr_l^n} \right)^3 \tag{4.14}$$

which relates fluid parameters, surface-to-fluid interaction, and excess temperature to the applied heat flux. This correlation is valid for the isolated bubble region of the pool boiling curve, which corresponds to an excess temperature of $5 \leq \Delta T_e \leq 10^o C$. For the jets and column region , $10 \leq \Delta T_e \leq 25^o C$, the curve over predicts the surface heat flux as a function of excess temperature.

Chang et al. [35] developed a two-phase correlation for impinging confined and submerged jets of R-113 with a two phase inlet condition. The correlation uses the superposition method, described previously, and modifies the single-phase heat transfer coefficient with the Martinelli parameter to account for the two-phase inlet. The form of the nucleate boiling heat transfer coefficient, $\overline{h}_{NB}$, was taken from the Rohsenow [40] pool boiling correlation, Eqn. 4.14, with the exponent n set to 1.7 and the constant $C_{s,f}$, experimentally determined, set to be 0.0091. The

final form of $\overline{h}_{NB}$, spatially averaged from the center of the heated surface to some radius r, was defined as

$$\overline{h}_{NB} = \mu_l h_{fg} \left[\frac{g(\rho_l - \rho_v)}{\sigma}\right]^{1/2} \left(\frac{c_{p,l}}{0.0091 i_{lv} Pr_l^{1.7}}\right)^{3.5} {\Delta T_e}^{2.5}(r) \tag{4.15}$$

4.3 Proposed Correlation

Because the current work uses water instead of R-113, as was used by Chang et al. [35], $C_{s,f}$ and exponent n for the nucleate boiling heat transfer coefficient, $\overline{h}_{NB}$, will be taken from the experimental data reported by Pioro [41]. The single-phase heat transfer coefficient, from Chang et al. [20], for the range of $r/d_j \geq 1.25$ will be used to find the spatially averaged single phase heat transfer coefficient over the entire heated surface. The heat transfer coefficients

$$\overline{h}_{1\phi} = 0.7017 \frac{k_l}{d_j} Re_j^{0.574} Pr^{0.4} \left(\frac{H}{d_j}\right)^{-0.106} \left(\frac{r}{d_j}\right)^{-0.62} \tag{4.16}$$

and

$$\overline{h}_{NB} = \mu_l h_{fg} \left[\frac{g(\rho_l - \rho_v)}{\sigma}\right]^{1/2} \left(\frac{c_{p,l}}{C_{s,f} i_{lv} Pr_l^n}\right)^{3.5} {\Delta T_e}^{2.5} \tag{4.17}$$

will be used with Eqn. 4.2 to evaluate the total surface heat flux as a function of wall temperature. The average wall temperature extrapolated from the 1-D conduction approximation will be used with the proposed correlation.

Chapter 5 – Experimental Facility and Methods

The confined jet geometry used for testing requires the variation of three parameters: applied heat flux, q", inlet ass flow rate, $\dot{m}_{in}$, and nozzle-to-surface spacing, H. Note that H is also referred to as the gap height or gap spacing. Using a testing matrix that varies these three parameters, their influence on flow boiling performance and facility operation stability in a confined jet geometry is examined (the testing parameters are discussed in section 5.4). Discussion of the system designed to study these testing parameters is split into two sections, test device and test facility.

5.1 Test Device

A test device was designed to allow for the study of the three parameters and could be easily reconfigured between test cases. The device also had to withstand the high temperatures expected during operation, have necessary ports for instrumentation and visualization, and to seal completely for high vacuum pressure testing. Polyetheretherkeytone (PEEK) was selected as the material for the two piece housing that contains all the other modular pieces and serves as thermal and electrical insulation. The housing is constructed using a piston-cylinder arrangement that allows for the nozzle-to-surface spacing , H, to be set using precision machined gage blocks. A cross-sectional view of the test piece assembly is shown in Fig. 5.5(a). Features labeled in Fig. 5.5(a) will be discussed in following sections.

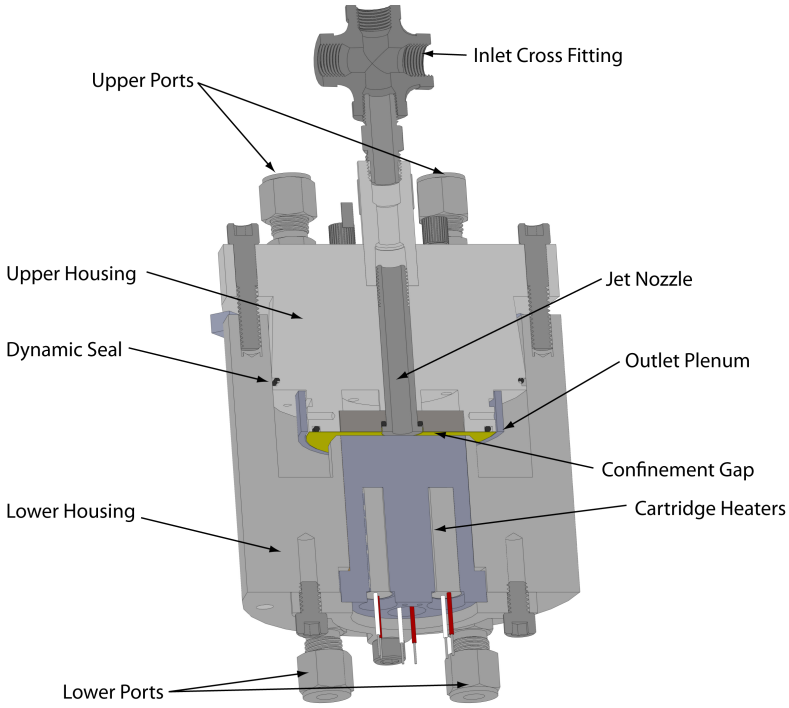

Figure 5.1: Cross section of test piece.

A three dimensional exploded view, shown in Fig. 5.2, illustrates the additional design features and fit of the modular pieces. Three borosilicate glass discs, sealed with compression o-rings and located at 120^o intervals, are used as ports for visualization of the impingement surface as well as for control of the fluid level in the test piece. Additionally the test piece was designed to allow for the confinement surface to be interchangeable for future vapor extraction studies. For the current study, a piece of non-porous Teflon layered with a permeable Teflon membrane was used as the upper confinement surface. The permeable membrane sheet was included to keep the surface characteristics of confinement surface comparable between the non-extraction testing reported here and extraction testing performed using the same device. A system of o-rings and retaining pieces was used to hold the Teflon sheets in place and seal the confinement surface from leakage. High temperature

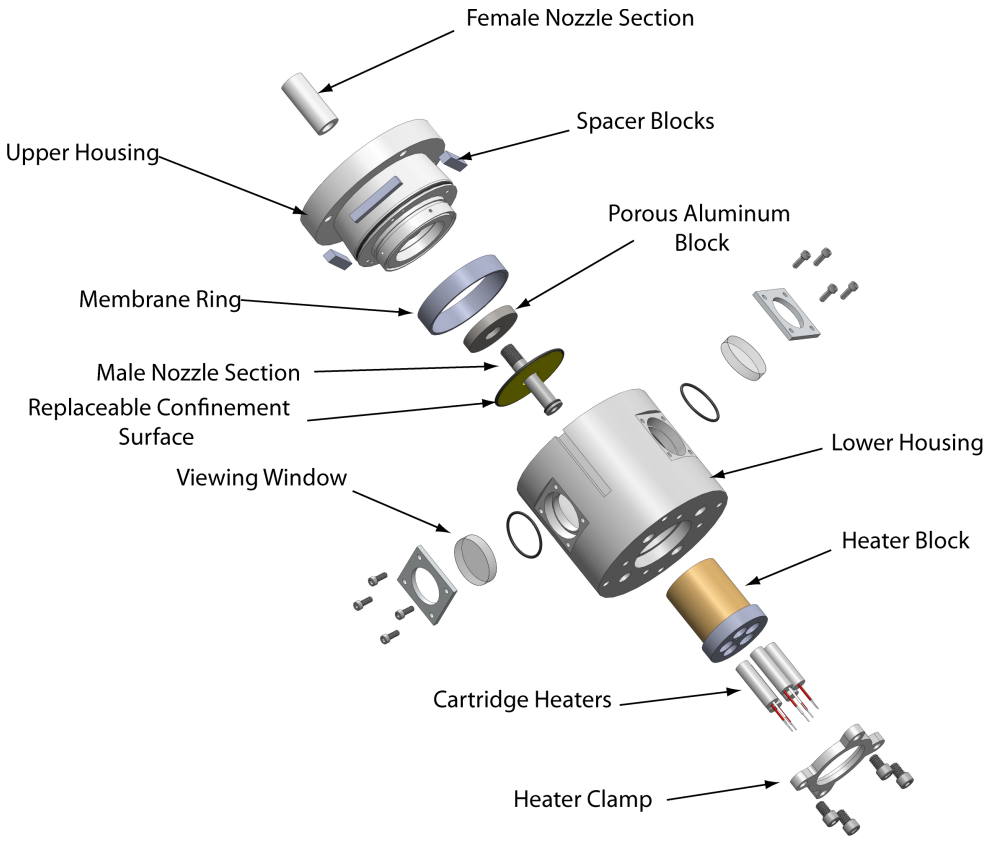

Figure 5.2: Exploded view of test piece.

porous aluminum blocks were used as structural backing for the Teflon sheets. The heater block was also designed to be removable from the PEEK housing. The heater block is secured using a system of o-rings and a retaining clamp that bolts to the lower housing of the test device. The heater block is machined from 6061 Aluminum with features for five 9.5 mm diameter, 300 Watt cartridge heaters and three thermocouples. The thermocouples are located on the same radius but have varying depths for use in the calculations of applied heat flux and surface temperature. A detailed discussion of the thermocouple locations and how they are used in calculations is provided later. The impingement surface is 38 mm in diameter and is sealed to the insulating PEEK sleeve using high temperature silicone RTV. The

surface of the heater block was roughened using a media blasting process and then plated with 24 Karat gold layer to inhibit corrosion of the impingement surface.

The device was insulated using Plexiglas containment structure filled with fiberglass insulation. Two containment structures were fabricated for the top and bottom of the device. The design allowed for easy removal of the insulation for servicing and modification of the test piece. A test stand was fabricated from extruded aluminum and a machined aluminum plate that attached to the PEEK housing of the test device. Additional features such as a parts tray, utility clamps for lighting, and secure mounting points for wiring and water lines were also designed into the test stand.

5.2 Test Facility

The following sections describe the flow loop, instrumentation, heater power supply, and data acquisition system used in the present study.

5.2.1 Flow Loop

A flow loop was designed to supply the working fluid, distilled water, to the test piece. Incorporated in the flow loop are devices to control the inlet temperature of the fluid stream entering the test device, and instruments to measure pressures, temperatures, and mass flow rates. A converted hot water heater serves as the degassing and storage tank for the distilled water. The fluid was then pumped, using a Micropump gear pump, through a series of filters and a needle valve for fine control over the flow rate. The inlet flow rate of the water is measured using a MicroMotion Coriolis flow meter before entering the constant temperature hot

oil bath. The oil bath preheats the water to approximately 10 degrees below the saturation point as it enters the test piece. Fluid pressure and temperature measurements are collected directly upstream to the inlet to the nozzle of the confined jet. Figure 5.3 shows the layout of the instrumentation and the path of the working fluid described above. A complete list of the instruments used in the experimental facility is located in section 1 of Appendix B.

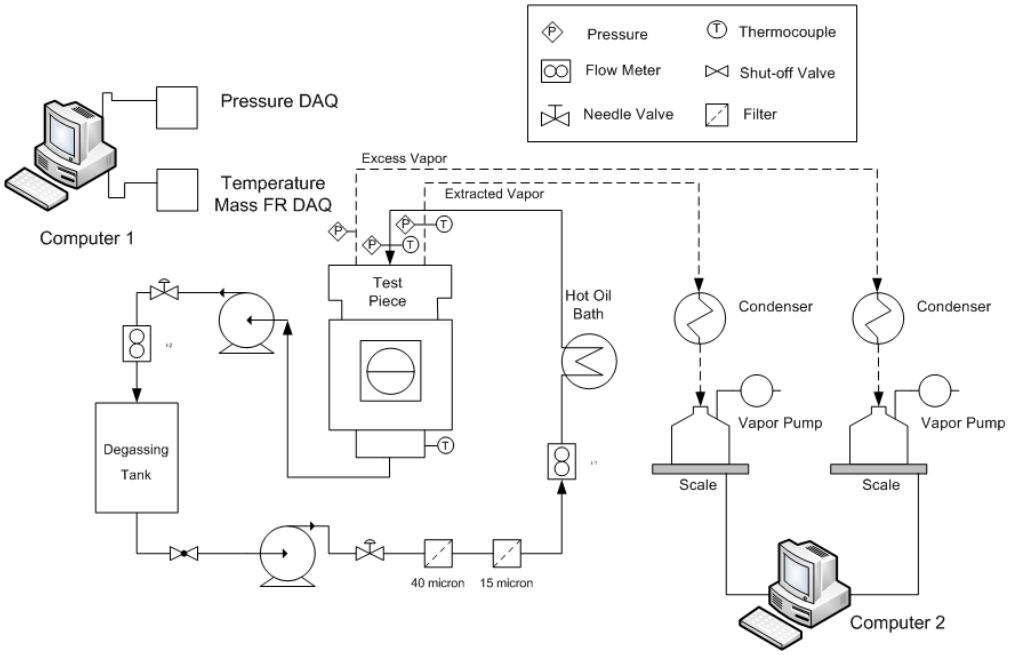

Figure 5.3: Schematic of the flowloop used in the experimental facility.

Once the sub-cooled water enters the test piece and the jet impinges on the heated surface, the fluid can take three different paths to exit the device. The generated vapor could be extracted through the porous Teflon sheets, excess vapor is collected from the top of the exit plenum, or excess liquid is drained from the bottom of the exit plenum. As extraction was not used in the current research, only the excess vapor and excess liquid paths are available for the fluid to exit from the exit plenum. Vapor leaves through the top of the test device, flows through a

condenser and the condensate is collected in a catch and weigh system. The liquid exits the bottom of test device, where a pump is used to control the outlet flow and thereby maintain a fixed fluid level in the exit plenum of the device. A needle valve serves as fine control for the exiting liquid flow rate before the fluid passes through the second MicroMotion Coriolis flow meter and returns to the degassing tank.

5.2.2 Instrumentation

Pressure, temperature, and mass flow rate measurements are collected at several locations in the flow loop and test piece. In the test piece, threaded ports for instrumentation allow for pressure transducer taps and sheathed thermocouples to be installed using compression fittings. Pressure transducers were installed vertically with snubbers to prevent damage to the sensing elements. Two absolute pressure transducers, with a range of 0-206 kPa, are located at the inlet and extraction ports. A 0-103 kPa differential pressure transducer is connected with one port to the inlet T-fitting with a second port to the outlet plenum. All three pressure transducers have an excitation voltage of 10 V and were powered using a Tektronix PG2125G programmable power supply. Voltage measurements were recorded by the data acquisition (DAQ) system, which is detailed in section 5.3, and converted to pressure measurements in the data processing using calibration curves. Complete calibration information is located in section 3 of Appendix B.

Thermocouples used for temperature measurements were shielded and grounded T-type. The sheathed thermocouples were installed with compression fittings and the device was pressurized with air to check for leaks prior to testing. Figure 5.4

shows the locations of pressure, temperature and fluid ports on the test piece.

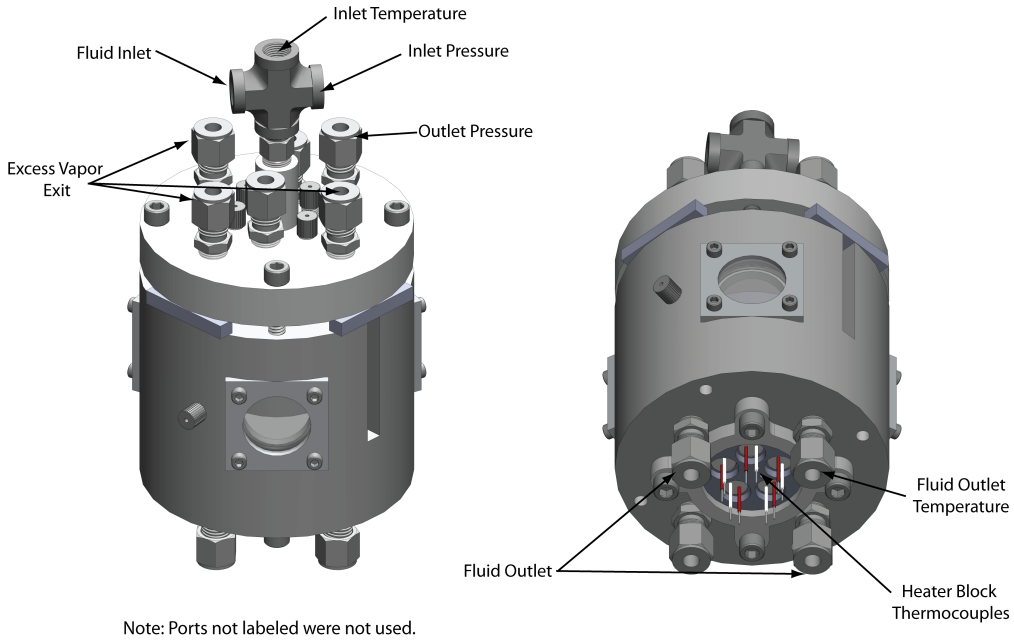

Figure 5.4: Locations of instrumentation and fluid ports in the test device.

Temperature measurements in the heater block are used to assess losses as well as extrapolate the surface temperature from input power data. The thermocouples are spaced 5 mm apart with the deepest one 1.25 mm from the impingement surface. The thermal conductivity ,k_{Al}, of 6061 aluminum is reported to be 172 W/m-K from the supplier. Using the thermocouple readings, input power measurements and the material constants, a one dimensional conduction analysis was used to validate the computed surface heat flux and extrapolate the surface temperature. A complete discussion of these calculations and comparison of the various methods used is presented in Chapter 6: Data Reduction and Analysis. Figure 5.5 shows the location of the three thermocouples in the heater block.

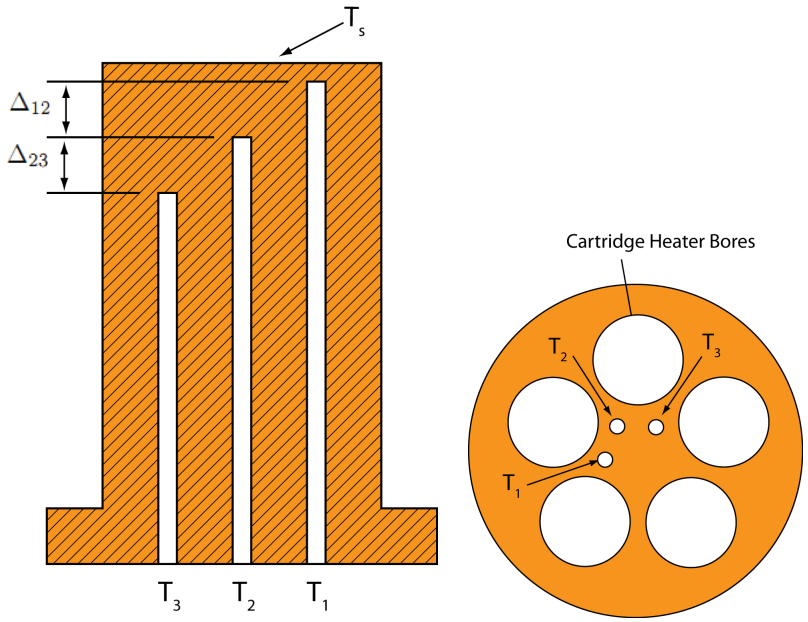

(a) (b)

Figure 5.5: Cross section (a)and bottom (b) view of the heater block.

The depths of the thermocouple bores were measured using a machined rod and a digital height gage on a machined granite block. Precise measurements of the thermocouple locations were required due to the sensitivity of the heat flux and surface temperature calculations to the thermocouple spacing. The five cartridge heaters were installed using high temperature silicone RTV to prevent movement during thermal cycling. After installing the heater block assembly into the test device, the leads for the heaters and the thermocouples were secured to a test stand fixed to the Newport table, preventing any movement of the heaters and/or thermocouples from accidental disturbances to the leads.

Mass flow measurements were taken using a combination of Coriolis flow meters and precision balances set up to catch and weigh the condensed vapor. The Coriolis flow meters were manufactured by MicroMotion and were installed in the inlet and

exit liquid lines The catch and weigh configuration was designed to allow for a vacuum to be drawn on the collection vessel. Attaching the vacuum lines to a cork placed in a glass flask caused the scale readings to be influenced when a strong vacuum was pulled. The vacuum caused the flexible lines to retract and lifted the flask off the scale. To resolve this issue, harder plastic tubes were heated and formed with right angles and then attached to a linear stage that allowed the flask to be precisely placed on the balance. A picture of the balance and translation stage is shown below in Fig. 5.6.

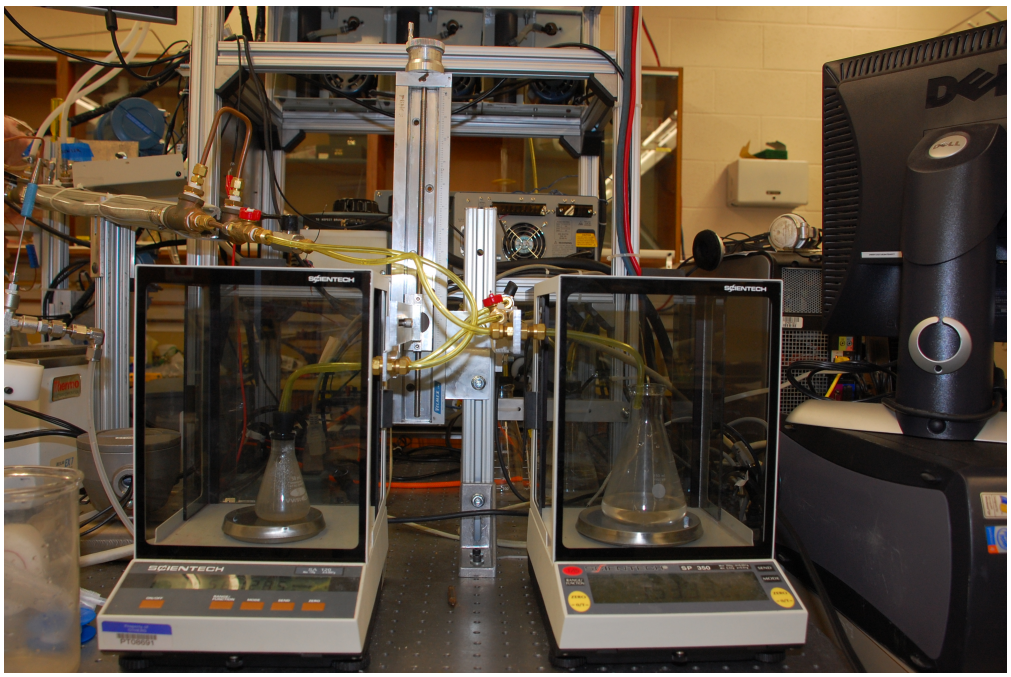

Figure 5.6: Catch and weigh balances with translation stage.

A complete list of the instrumentation employed, with manufacturer, model number, and calibration information is provided in Table B.3 in Appendix B.

5.2.3 Heater Power Supply

A custom power supply was fabricated to control the power input to the cartridge heaters. The five 300 W heaters required accurate and safe control throughout the anticipated input power range. The power supply features a Watlow TemperatureLV controller that operates a shut off switch that prevents the device from overheating should any malfunction occur. The switch is connected to the middle heater block thermocouple and can be set with a resolution 1^oC. The voltage supplied is controlled using a Powerstat variable transformer (variac) capable of delivering up to 1.5 kW. Measurements of current and voltage are recorded using a Tektronix THS720P digital oscilloscope that is connected to the data acquisition computer via a RS232 cable. The wiring schematic shown below in Fig. 5.7 illustrates interconnects between the components discussed.

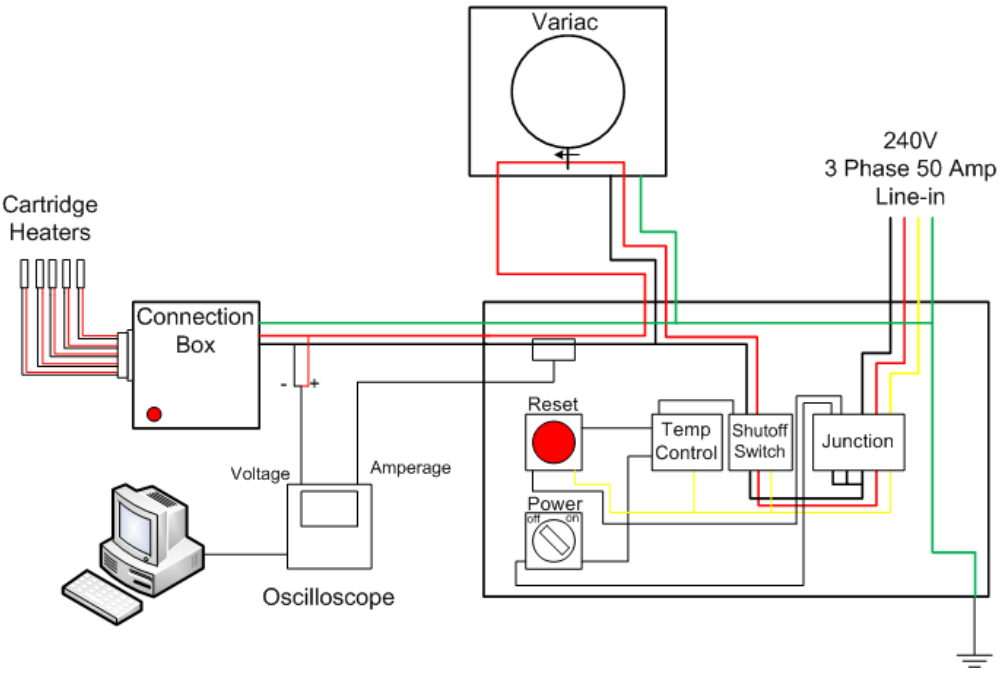

Figure 5.7: Schematic of cartridge heater power supply.

5.3 Data Acquisition

Two computers were used for data collection due to the number and type of signals collected. Pressure, temperature, and flow rate measurements, from the Coriolis meters, were collected using two National Instruments data acquisition cards interfaced with a Dell workstation. The first data acquisition card, used for the mass flow rate and temperature measurements, was an NI PCI-MIO-16E-4 with a 16 bit resolution and a 200 ks/s maximum sampling rate. The second data acquisition card, used for the pressure measurements, was a NI PCI-6034E with a 12 bit resolution and 250 ks/s multichannel sampling rate. Complete details about the data acquisition equipment used can be found in Appendix B. LabVIEW 2009 was used to collect measurements from both DAQ cards at a constant 3.5 Hz through the entire test case and were recorded using the proprietary LabVIEW format TDMS. High frequency data, from the inlet pressure transducer, was collected three times during each steady state test point at 2 kHz for 5 seconds.

While data were continuously collected throughout the entire test case, steady-state points were marked by the operator adhering to a strict timing schedule. Steady-state data were recorded for a minimum of 8 minutes. The duration of the transient period, between steady-state points, lasted a minimum of 10 minutes. In the data output, steady-state conditions were denoted in a column by the number one while transient conditions were denoted by the number zero. The process flowchart for this data acquisition program is shown in Fig. A.1. The LabVIEW front panel is shown in Fig. A.2, both of which are located in Appendix A. A representation of the computer and the two connection boxes in relation to the instruments can be seen in Fig. 5.3. Grounded shielded cables were used for all connections from the connection boxes to the pressure transducers. Removable

connections were installed on all thermocouples and pressure transducers to allow for easy disassembly of the test piece. All connections were tagged and marked to prevent confusion during reassembly.

Temperature measurements were converted automatically in LabView using the built in thermocouple data acquisition program and referenced to a cold junction thermistor built into the DAQ board. Pressure measurements were recorded as voltage values. Both output temperature and pressure voltage measurements were later converted using the curves provided in section 3 Appendix B. Mass flow rate measurements from the Coriolis meters were converted from the frequency values using the scaling value

$$F_{scale} = \frac{mass\ flow\ rate}{frequency} \tag{5.1}$$

where the rate corresponds to the flow rate range, 800 g/min for the current testing, and the frequency was 10 kHz. All the recorded values were saved within the TDMS file.

The second computer was interfaced with the digital scale and the digital oscilloscope for assessment of the vapor flow rate and power measurements. The digital oscilloscope recorded amperage measurements using a Tektronix A261 current probe and voltage measurements using a Tektronix P5200 differential voltage probe. The differential voltage probe had two ranges, 50x (0-150V) and 500x(150-1500V), and the proper range needed to be selected during the test cases. The oscilloscope and digital scale were interfaced with RS232 serial cables and data were collected using a second LabVIEW program. A flow chart for the data collection process is shown in Fig. A.3 and the font panel for the LabView program is shown in Fig. A.4 both of which are located in Appendix A. The weight, voltage, and amperage measurements are recorded in a tab delimited text file.

Table 5.1: Experimental testing parameters.

Parameter	Values
H	1, 2, 4 , 6, 8 mm
H/D_j	0.25, 0.5, 1, 1.5, 2
$\dot{m}_{in}$	150, 300, 600 g/min
Re_j	2530, 5060, 13500
q''	0-90 W/cm^2

5.4 Test Matrix

To assess the influence of nozzle-to-surface spacing, H, and inlet mass flow rate, $\dot{m}_{in}$, on the performance and stability of the confined jet, a range of test conditions were developed from results of initial testing. Fixed testing conditions included a 4 mm diameter jet, 38 mm diameter heated impingement surface, and 10^oC subcooled water for the working fluid. The test parameters, and their respective non-dimensional values, are shown in Table 5.1. For each combination of H/d_j and Re_j, a test case was taken with 20 different heat inputs from 0 to 90 W/cm^2. The heat input set points were selected to resolve sections of the boiling curve and to show performance trends in the different regimes. Additional repetitions of test cases were performed to ensure the accuracy and repeatability of each data set.

5.5 Test Procedure

The first step in the procedure consists of preparing the heater surface and the flow loop. The surface requires cleaning prior to the acquisition of each data set in order to ensure the surface characteristics are the same between test cases. The gold plated surface resists corrosion but the evaporating water still leaves deposits

on the surface. A commercially available metal cleaner, Eagle One® metal polish, is used to remove the deposits. The surface is then wiped thoroughly with isopropyl alcohol on a Kimtech® Kim-wipe. The alcohol is allowed to completely evaporate prior to reassembly of the test piece. Distilled water is degassed in the holding tank for approximately an hour during the cleaning and test device assembly process. The distilled water in the tank is replenished daily for testing.

Prior to operation, the filters are removed and back flushed to remove any contaminates that may have built up. Warm up of the flow loop and test device takes approximately 45 minutes, during which the temperatures are monitored to ensure the system is at steady-state before data collection began. Depending on the flow rate, the oil bath temperature required adjustment to compensate for the change in thermal capacity due the mass flow rate. Cooling water for the condensers is turned on prior to data collection. Once the system has reached steady state temperatures and the mass flow rates are constant, the data acquisition program is initialized and testing begins.

During testing the operator monitors the data acquisition process, fluid level in the test device, and fluid collection in the scale. As discussed previously, a timing schedule for transient and steady state conditions allows for consistent data collection. At each set point, the power was adjusted using the variac and the system is allowed to stabilize. After setting the power input, the fluid level is monitored and the outlet flow rate adjusted to compensate for increased vapor generation. After ten minutes, steady-state data collection was initiated by the operator. During the transient period, the collection vessels on the catch and weighs are be emptied, as necessary, particularly during the high heat flux cases.

After completing the test points in a given cases, the data collection was

stopped. The power to the cartridge heaters were shut off and the temperatures were monitored as water was allowed to continue circulating through the device. Once the device temperatures dropped below 100 ^oC, the pumps and remaining instruments were powered down.

Chapter 6 – Data Reduction and Analysis

The process used to convert the raw data to calibrated values, calculate relevant quantities for performance and stability analysis, and determine the uncertainty in the calculated results is detailed in this chapter.

6.1 Data Reduction

The LabView TDMS file from the first DAQ computer(which contains the temperature, voltage values from the pressure transducers, and mass flow rates measurement) is first converted to a Matlab object using code supplied by National Instruments. Next the data were processed and calibration curves, shown in Appendix B, are applied to the raw data. The scale data were checked to ensure that no irregularities exist, which can occur during operation if the collection flask over flows or is emptied in the middle of a steady-state case. Additional checks are performed to ensure that number of steady-state cases are the same for the data sets collected from both computers. Because the steady-state points are marked by the operator, it is possible for an error to occur and the number of cases will not match up. If an error was made during testing, the operator can select the erroneous point and remove it from the processed data. With duplicate cases or operator errors removed from the scale data, a linear curve fit was applied to the outlet vapor weight versus time data to assess the mass flow rate. After the scale and power data has been processed, they are combined with the calibrated pressure, temperature, and mass flow rate data into a single Matlab object.

6.2 Analysis

With all calibrated data contained within a single data structure, several post processing programs perform the necessary calculations and analyses. The calculations performed with the processed data are detailed in the following sections.

6.2.1 Performance

Several methods were used to evaluate the applied heat flux to the surface and compared for accuracy. The first method uses the measured power and the heater surface area to determine the raw uncorrected heat flux, according to

$$q''_P = \frac{IV}{A_s} \tag{6.1}$$

Adjusting this expression for losses results in

$$q''_{PC} = \frac{IV - Q_{loss}}{A_s} \tag{6.2}$$

where Q_{loss} was determined from a heat loss experiment, q''_P is the flux calculated from the raw electrical power, and q''_{PC} is the heat flux calculated from the electrical power corrected for losses .

To assess heat loss during operation, the impingement surface was insulted with a one inch thick piece of Teflon® and 10 ^oC subcooled water was circulated through exit plenum of the device to simulate conditions seen during operation. Power was supplied in increments of 5 W and the resulting heater block temperatures were recorded. This allowed for the heat losses as a function of heater block temperature to be determined. A curve fit was applied to the data to develop an equation, Eqn.

6.3, that relates losses to the heater block temperature. At steady-state conditions during testing, all the thermocouple measurements were within their uncertainties. Therefore, the middle heater block temperature was used to develop the heat loss equation

$$Q_{loss} = 0.4135(T_{HB2}) - 35.23 \tag{6.3}$$

to evaluate losses during testing. Figure 6.1 illustrates the heat loss data from the experiment and the curve fit of the data, Eqn. 6.3. The standard error of the curve fit was found to be 1.94 W.

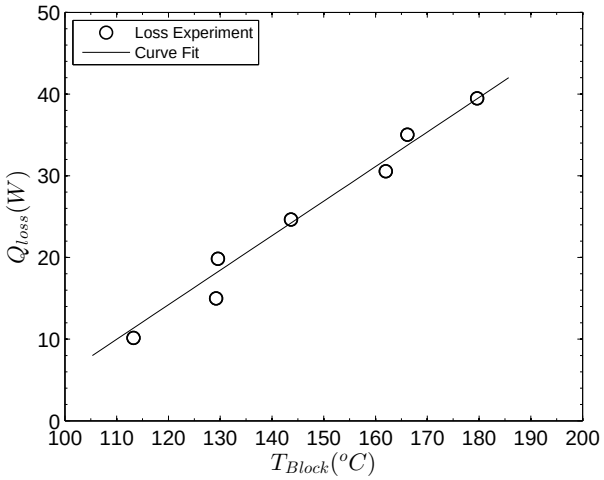

Figure 6.1: Heat loss as a function of heater block temperature.

An alternative method for calculating the heat flux uses a 1-D conduction approximation and the temperature measurements from thermocouples 2 and 3, the locations of which are shown in from Fig. 5.5. Thermocouple 1 was not used because the measurements differed significantly from the 1-D approximate temperature calculated for that location based on the other two thermocouples. This could be attributed to material lodged in the thermocouple bore that increased the conduction resistance. Therefore, this measurement is not used in the heat flux

calculations or thermocouple measurements. The resulting equation is

$$q''_{23} = \frac{k_s}{L_{23}}(T_3 - T_2) \tag{6.4}$$

Heat flux, calculated using Eqn. 6.4, is compared to the heat flux calculations defined from Eqn. 6.2. The wall temperature is extrapolated using a 1-D conduction model using surface heat flux and temperature measurements from the middle thermocouple:

$$T_w = T_2 - \frac{q''_s}{k_s \Delta_{2s}} \tag{6.5}$$

For this assessment q'' is determined from Eqn. 6.2. A comparison of the heat fluxes calculated using the raw electrical power (Eqn. 6.1), the loss corrected electrical power (Eqn. 6.2), and the 1-D conduction approximation (Eqn. 6.4) as a function of their respective wall temperatures is shown in Fig. 6.2.

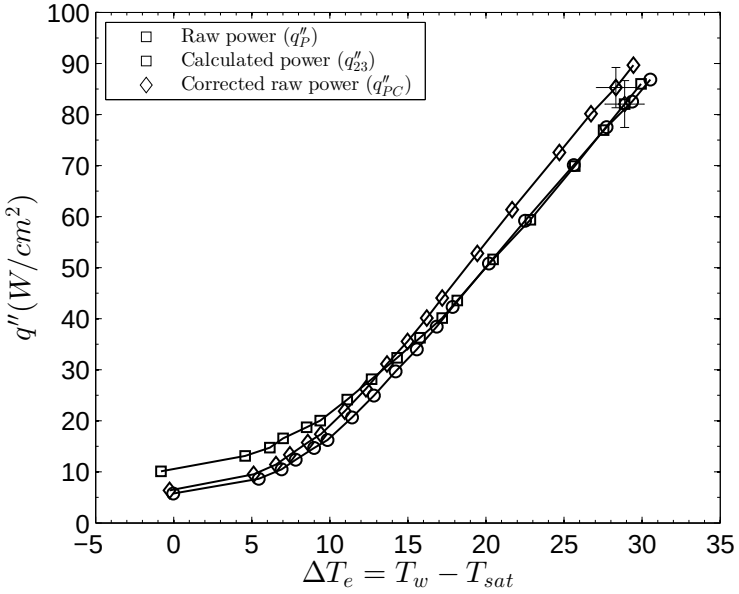

Figure 6.2: Comparison of heat flux calculations.

In the single-phase region, the calculated heat flux, q''_{23}, is observed to be somewhat greater than the heat flux calculate from the corrected electrical power, q''_{PC}. This can be explained by an examination of the uncertainties associated with the calculated heat flux and measured input power. The calculated heat flux, using thermocouples 2 and 3, has an uncertainty of approximately 5 W/cm^2 over the entire range, which encompasses the heat flux assessed using the input power in the single-phase region. The main contribution to this uncertainty is the repeated measurement error of the thermocouples. At low heat fluxes, the difference between the two thermocouple measurements is very small, on the order of their uncertainties. The error from the power measurement, on the other hand, is a function of the input power and is, therefore, very small at low power levels. Therefore, the input power, appropriately corrected for losses, is a more accurate method to calculate the applied heat flux over the entire input power range. Eqn. 6.2 was used to calculated the applied heat flux for all results presented. All fluid properties used in the calculated results were found using the XSteam program integrated with Matlab. The excess temperature is

$$T_e = T_w - T_{sat}(P_{in}) \tag{6.6}$$

where T_w is the wall temperature determined from Eqn. 6.5 and the saturation temperature evaluated based on the inlet pressure. Mass and energy balances, using the control volume shown in Fig. 6.3, were calculated to verify the accuracy and validity of the experimental results. the basic energy balance can be written as

$$\dot{E}_{in} = \dot{E}_{out} \tag{6.7}$$

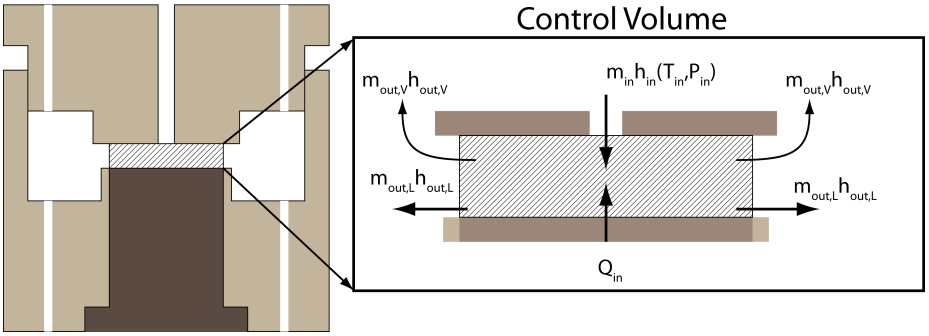

Figure 6.3: Control volume used for mass and energy balances.

where

$$\dot{E}_{in} = \dot{Q}_{in} + \dot{m}_{in} i_{in,L} \tag{6.8}$$

and

$$\dot{E}_{out} = \dot{m}_{out,L} i_{out,L} + \dot{m}_{out,V} i_{out,V} \tag{6.9}$$

Substituting Eqn.6.8 and Eqn. 6.9 in to Eqn. 6.7 yields

$$\dot{Q}_{in} + \dot{m}_{in} i_{in,L} = \dot{m}_{out,L} i_{out,L} + \dot{m}_{out,V} i_{out,V} \tag{6.10}$$

where the enthalpy of the inlet fluid, $i_{in,L}$, is evaluated using the inlet temperature and pressure measurements, the outlet fluid enthalpy, $i_{out,L}$, is assumed to be a saturated liquid evaluated at the measured outlet temperature, and the out vapor enthalpy, $i_{out,V}$, is assumed to be a saturated vapor evaluated at the outlet pressure. The energy balance is rearranged to solve for discrepancies between the energy input and the energy output, $\dot{E}_{error}$,

$$\dot{E}_{error} = \dot{Q}_{in} + \dot{m}_{in} i_{in,L} - \dot{m}_{out,L} i_{out,L} - \dot{m}_{out,V} i_{out,V} \tag{6.11}$$

The heat flux required to heat the inlet subcooled fluid to saturated boiling con-

ditions ,denoted by the subscript IB, was calculated using

$$q''_{IB} = \frac{\dot{m}_{in}}{A_s}(i_{sat,L} - i_{in,L}) \tag{6.12}$$

where q''_{IB} is the heat flux necessary to initiate saturated boiling and $i_{in,L}$ is evaluated using the inlet temperature and pressure, and $i_{sat,L}$ is evaluated using the inlet pressure and the assumption the fluid is a saturated liquid. The mass balance

$$\dot{m}_{in} = \dot{m}_{out,L} + \dot{m}_{out,V} \tag{6.13}$$

relates the inlet mass flow rate to the flow rates of the exiting vapor and liquid flow rates. Inlet and outlet mass flow rates are measured using Coriolis mass flow meters and the excess mass flow rate was measured using catch and weigh. Rearranging Eqn. 6.13, the error in measured mass balance is calculated.

$$\dot{m}_{error} = \dot{m}_{in} - \dot{m}_{out,L} + \dot{m}_{out,V} \tag{6.14}$$

6.2.2 Frequency Analysis

The frequency analysis of the time response of the inlet pressure was performed using a power spectral density calculated from a discrete Fourier transform. First the mean of the signal is removed and the length of the sample is adjusted to be equal to 2^n of points. The fast Fourier transform(FFT) was applied, which is a function in Matlab and is given by

$$X(k) = \sum_{j=1}^{N} x(j)\omega_N^{(j-1)(k-1)} \tag{6.15}$$

where

$$\omega_N = e^{(-2\pi i)/N} \tag{6.16}$$

The symmetric portion of the FFT is removed and the remaining component is multiplied by 2 to preserve the energy content. The PSD is found by squaring the final calculated FFT value.

6.2.3 Uncertainty

The bias and precision uncertainty were calculated for each of the instruments used for measurements. The error associated with the linear curve fit of the calibration data were found using the standard error estimate defined as

$$S_{y,x} = \sqrt{\frac{\sum y_1^2 - b\sum y_1 a \sum x_1 y_1}{n-2}} \tag{6.17}$$

where a and b are the coefficients of the least-squares curve fit to the calibration data and n is the number of points in each calibration curve. The curve fit error is then root sum squared with the published uncertainty for the calibration standard.

$$\Theta_{bias} = \sqrt{S_{x,y}^2 + U_{stnd}^2} \tag{6.18}$$

The precision error associated with the repeated measurement

$$\Theta_x = \sqrt{\Theta_{bias}^2 + (t \times \sigma)^2} \tag{6.19}$$

where the variable σ is the standard deviation, not to be taken as the surface tension as previously defined, t is the student T-statistic for a 95% confidence

interval, and Θ_{bias} is the bias error. The uncertainty values for each measurement are shown in Appendix A. The measurement uncertainty is propagated to the calculated results using the Kline and McClintock method. Which is defined as:

$$U_R = \sqrt{\sum_{i=1}^{n} \left(\frac{\partial R}{\partial x_i} u_i \right)^2} \tag{6.20}$$

A sample calculation for the uncertainties in the calculated results is located in Appendix C and representative values are also shown as error bars in the plots.

Chapter 7 – Results and Discussion

Mass and energy balances, performance results, and stability characteristics are presented for inlet mass flow rates of 150, 300, and 600 g/min and nozzle-to-surface spacing of 1 mm to 8 mm. The Reynolds numbers, for a 4 mm diameter jet, which correspond to the mass flow rates tested are 2530, 5060, and 10120.

7.1 Mass and Energy Balances

Mass balances were performed for each test case to verify the device was not leaking and the curve fit to the catch and weigh measurements yielded accurate results. The flow rate measurements from the inlet Coriolis flow meter were compared to the outlet flow rate, which was the sum of the outlet Coriolis flow meter and the vapor catch and weigh, as presented in Eqn 6.13. Shown in Fig. 7.1 are the normalized discrepancies between the inlet and outlet mass flow rats, where the discrepancies are defined as the mass flow error, $\dot{m}_{error}$, in Eqn. 6.14 The error resulting from the mass balance calculations for all test points were within ± 0.5 g/min, which corresponds to the uncertainty of the flow rate measurements.

The energy balance was assessed using Eqn. 6.11 with the enthalpy values evaluated at the proscribed temperatures and pressures described in section 6.2.1. The energy difference term, ΔQ defined in Eqn. 6.11, is normalized by the total energy input to the system, E_{in}, as defined in Eqn. 6.8. Figure 7.2 illustrates the energy difference calculated for the three different inlet flow rates at a 2 mm gap spacing.

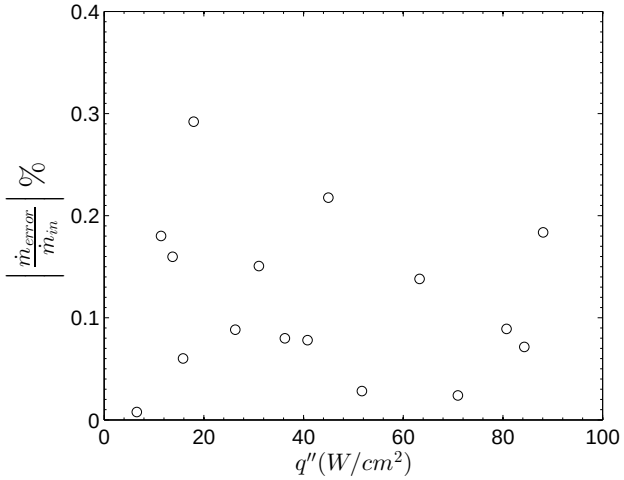

Figure 7.1: Error from mass flow rate measurements.

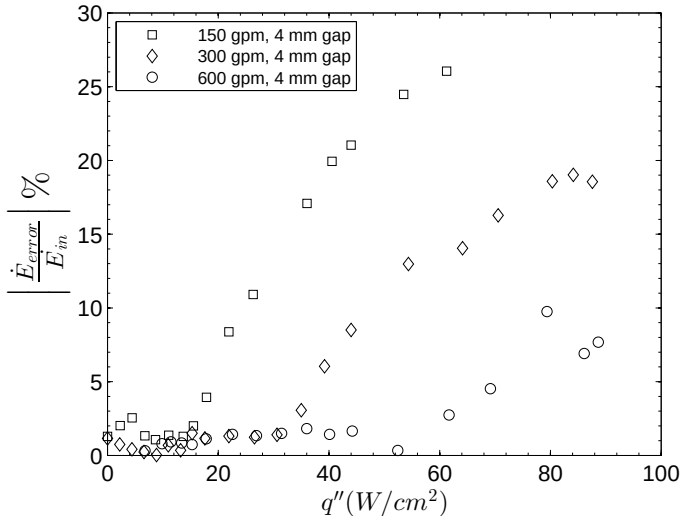

Figure 7.2: Discrepancies from the energy balance.

In the single phase region, the normalized energy difference is approximately $1-3\%$ and is attributed to the uncertainty in the temperature and pressure measurements used to evaluate the enthalpy terms. Once boiling occurs in the device, the discrepancies in the energy balance increase. Due to the small volume of the outlet plenum, the momentum of the exiting vapor pushes liquid up into the outlet

vapor ports. Because the enthalpy of saturated water vapor is an order of magnitude greater than that of saturated liquid water, the extra liquid in the outlet vapor flow rate causes large discrepancies in the energy balance. An alternative method for evaluating the energy balance is to solve for the total enthalpy of the outlet mass flow rate, h_{out} from Eqn. 7.1, leaving the outlet mass flow rate as a generic $\dot{m}_{out}$. Using this outlet enthalpy value, the exit quality(χ) can be determined from Eqn. 7.2.

$$Q_{in} + \dot{m}_{in} i_{in,L} = \dot{m}_{out} i_{out} \tag{7.1}$$

This quality represents a theoretical maximum amount of vapor that can be generated given the amount of heat input, Q_{in}, to the system.

$$h_{out} = (1 - \chi) h_l + \chi h_v \tag{7.2}$$

Comparing the calculated exit quality to the measured quality, as is done for a representative data set in Fig. 7.3, illustrates the influence of the extra liquid that is pushed up into the vapor outlet ports and measured in the vapor stream catch and weigh once condensed. Because the measured exit quality is higher than the calculated maximum, the explanation for the discrepancies in the energy balance at high heat fluxes appears to have been confirmed. Therefore, the exit quality is calculated using the energy balance, not from the vapor mass flow rate measurements.

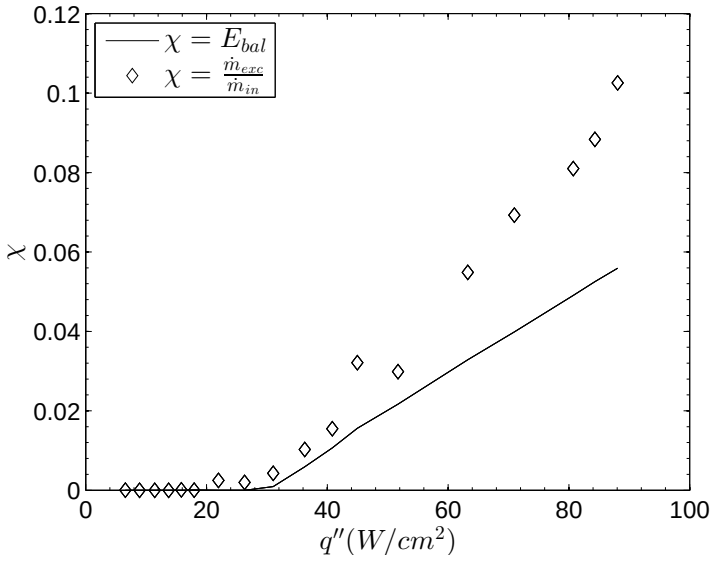

Figure 7.3: Calculated maximum exit quality and measured exit quality for a 300 g/min, 6 mm gap spacing case.

7.2 Boiling Curves

Boiling curves were generated for each test case to assess the influence of nozzle-to-surface spacing and inlet mass flow rate on the heat transfer performance of the confined impinging jet. To validate that the calculations of surface heat flux and excess temperature follow the expected trends, pool boiling data were collected and compared to the Rohsenhow [40] correlation, Eqn. 2.9. The surface-fluid coefficient, $C_{s,f}$, and the exponent on the Prandtl number, n, were determined, using the experimental pool boiling data, to be 0.016 and 1.26, respectively.

Examination of data repeatability over time illustrated that changes in the surface characteristics influenced the two-phase performance of the confined impinging jet. The surface was cleaned between test cases using a standardized cleaning procedure to remove mineral deposits left by the evaporating water. Despite the effort to ensure repeatable surface characteristics, pieces of the gold plating flaked off the

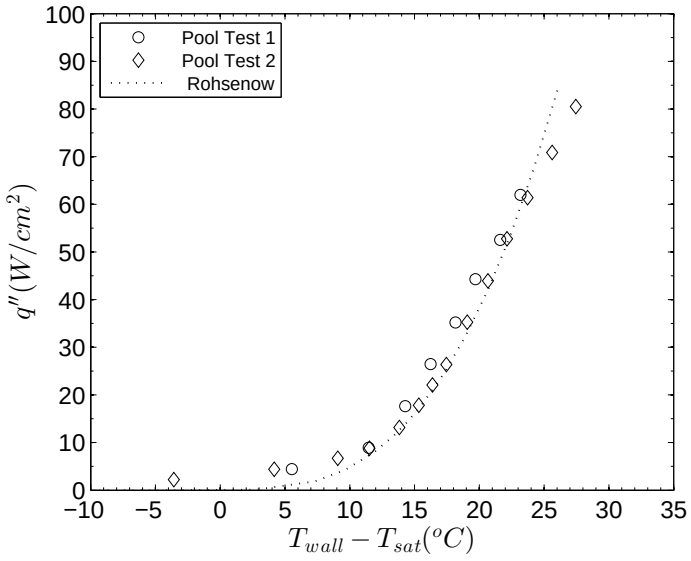

Figure 7.4: Comparison of pool boiling data to Rohsenhow [40] correlation using $C_{s,f} = 0.016$ and $n = 1.26$

surface over time. This resulted in changes in surface characteristics and effectively roughening the surface, which increased two-phase performance. Figure 7.5 shows three repetitions of a single test case, 150 g/min with a 4 mm gap spacing, illustrate the change in performance over time due to the changes in surface conditions. To eliminate this dependence on surface characteristics, test cases were taken after the gold plating had ceased to flake off and comparable cases were taking in succession to reduce changes in surface over time. All of the data presented uses this collection procedure. A method of validating data repeatability between test cases can be found from an examination of literature, which shows that the nucleate boiling regime is insensitive to changes in nozzle-to-surface spacing [3].

Influence of nozzle-to-surface spacing is illustrated in Figs. 7.6 and 7.7, which are examples of cases that were taken using the collection method described. As is evident, the influence of nozzle-to-surface spacing is insignificant, within the level of uncertainty, as would be expected and additionally validates the repeatability

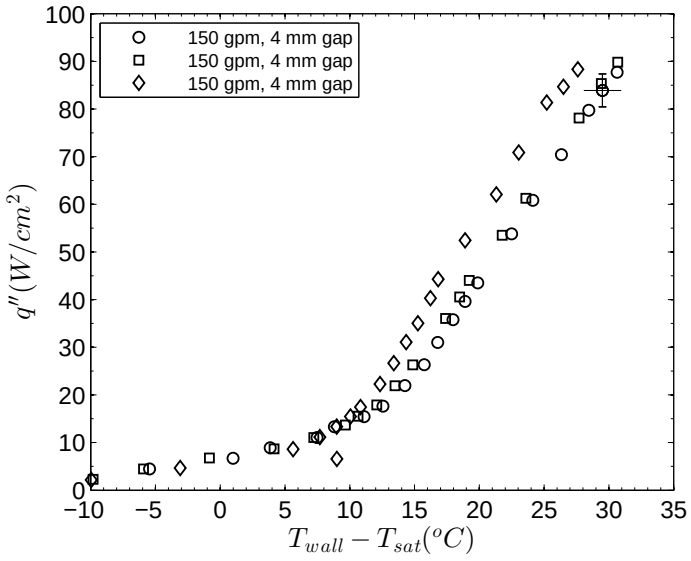

Figure 7.5: Effects of surface characteristics for a fixed mass flow rate of 150 g/min and 4 mm gap spacing.

of the results between data sets.

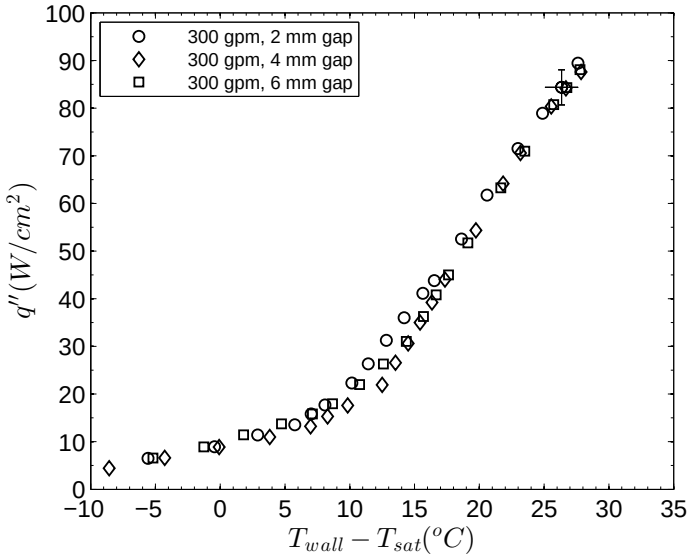

Figure 7.6: Effects of nozzle-to-surface spacing for a fixed mass flow rate of 300 g/min.

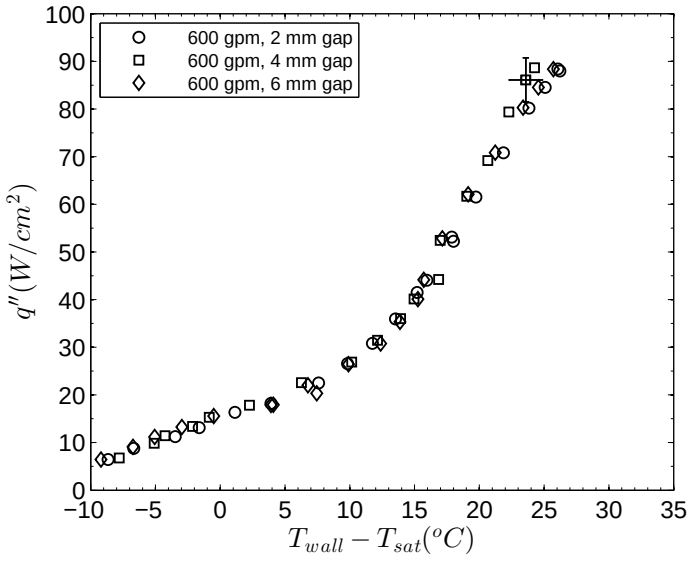

Figure 7.7: Effects of nozzle-to-surface spacing for a fixed mass flow rate of 600 g/min.

However in the single-phase region, existence of recirculation vortices have been shown in literature to influence local temperature distributions. These vortices are dependent on the nozzle-to-surface spacing [19]. Unfortunately because local surface temperature measurements are unavailable the degree of enhancement in q_s'', with respect to the nozzle to surface spacing, in the single-phase region is unknown. The results in the single phase region are not strongly influenced by the nozzle-to-surface spacing.

Figures 7.8 - 7.10 illustrate the influence of increasing mass flow rate for given nozzle-to-surface spacing of 2 mm, 4 mm, and 6 mm, respectively. For all three figures boiling curves were generated for inlet mass flow rates of 150 g/min, 300 g/min, and 600 g/min.

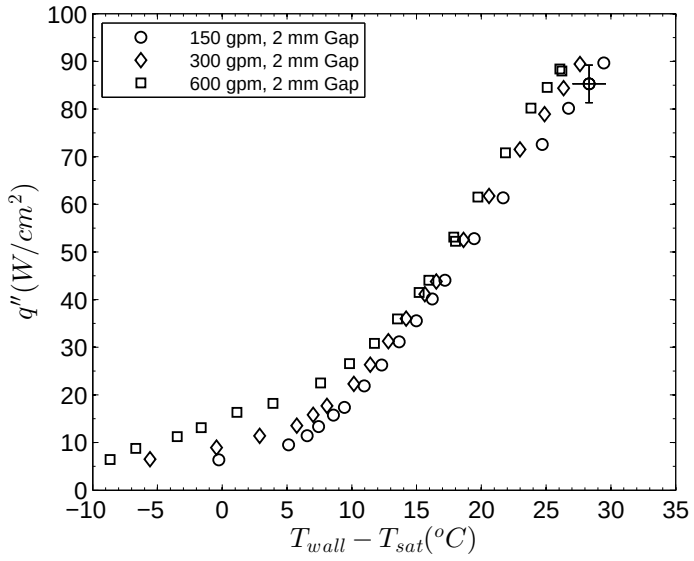

Figure 7.8: Influence of inlet mass flow rate for a 2 mm gap spacing.

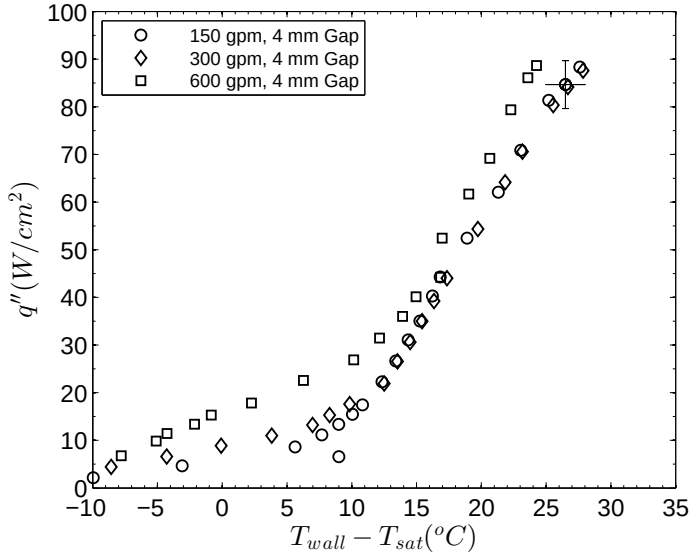

Figure 7.9: Influence of inlet mass flow rate for a 4 mm gap spacing.

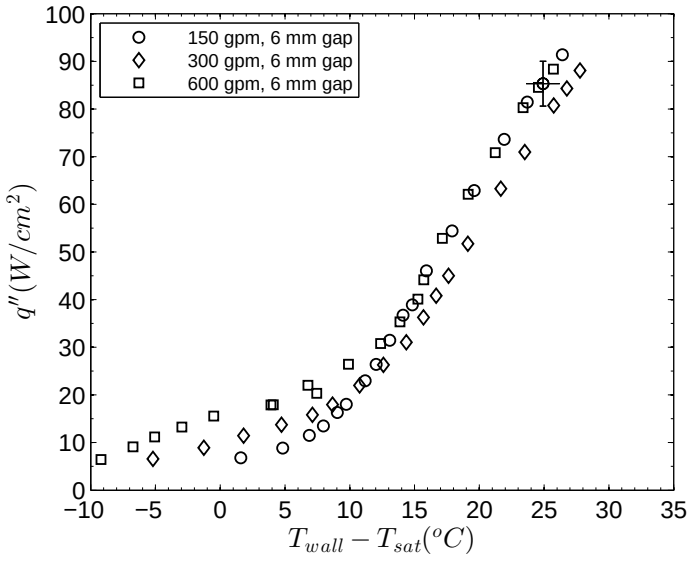

Figure 7.10: Influence of inlet mass flow rate for a 6 mm gap spacing.

Increasing inlet mass flow rate serves to enhance heat transfer in the single-phase regime and delay the onset of nucleate boiling (ONB) over the range of test conditions examined. The ONB corresponds the change in slope of the boiling curve. For example in Fig. 7.8, ONB for the 150 g/min case corresponds to an excess temperature ($T_w - T_{sat}$) of approximately 6^{o}C whereas the inception of ONB is delayed to approximately 11 ^{o}C for the 600 g/min case. These results agree with trends reported in previous literature [3]. Once the onset of nucleate boiling occurs, the heat transfer is dominated by the formation and departure of bubbles on the heated surface. The latent energy exchange results in the increase in the slope of surface heat flux (q''_s) as a function of excess temperature. To validate that the changes in slope, shown in Figs. 7.8 and 7.10, correspond to the onset of nucleate boiling, the heat flux necessary to heat the working fluid from the 10 ^oC subcooled inlet to saturated conditions is calculated using Eqn. 6.12. Figure 7.11 show the boiling curves for 150 g/min and 600 g/min at a 6 mm gap spacing and

the corresponding heat flux values required to initiate saturated boiling, q''_{IB}.

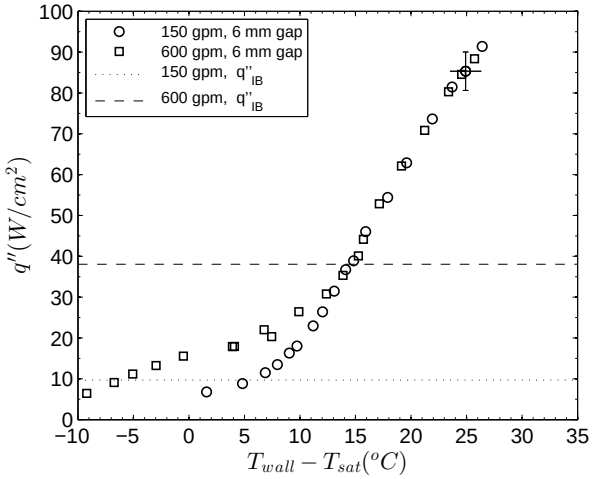

Figure 7.11: Calculated heat flux values necessary to initiate boiling for 150 g/min and 600 g/min at a 6 mm gap spacing.

The heat flux values necessary to initiate boiling, calculated from the energy balance, match with the changes in slope of the boiling curve that signify the transition from single-phase to nucleate boiling heat transfer.

The coefficient of performance(ϵ), originally defined in Eqn. 7.3, was used to measure the overall devices performance of the confined jet. Unfortunately the pressure drop through the test device was too low to be accurately measured except for test cases using the highest flow rate of 600 g/min and the two lowest gap spacing. The coefficient of performance as a function of applied heat flux is shown in Fig. 7.12 for the gap spacing of 2 mm and 4 mm.

$$\epsilon = \frac{q" A}{\Delta P \dot{V}} \tag{7.3}$$

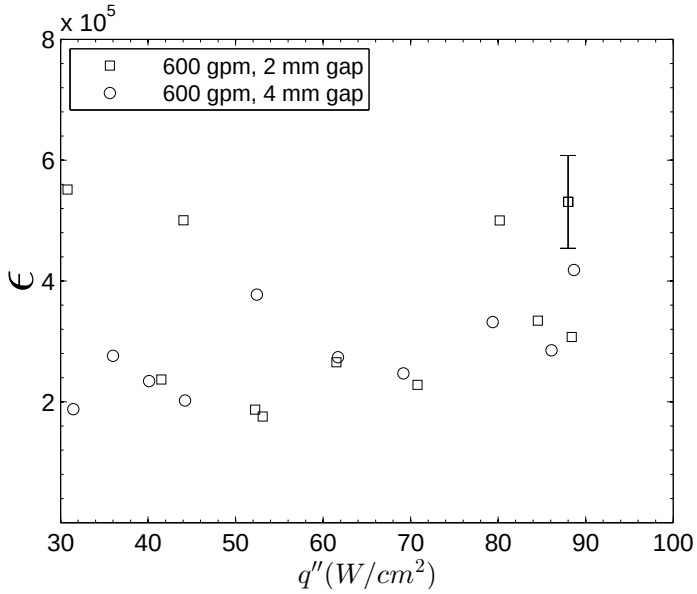

Figure 7.12: Coefficients of performance for 600 g/min with gap spacings of 2 mm and 4 mm.

For the test cases examined the maximum coefficient of performance achieved was $5.55x10^6$ at a heat flux of 90 W/cm^2 and a gap spacing for 2 mm. This result was determined using data from the highest flow rate and, therefore, the highest pressure drop. The pressure drop in the confined jet is a function of the surface heat flux and the quality of the fluid. As the fluid begins to boil, the vapor bubbles mix the fluid and effectively lower the total viscosity. This decreases the pressure drop through the device. There is a minimum in the pressure drop as a function of heat flux, after which the increasing vapor generation increase the pressure drop through the device. This phenomena will be examined in the stability results located in section 7.5. Based on this relationship, the coefficient of performance would be expected to have a similar trend, where the minimum in the pressure drop as a function of heat flux would correspond to a local maximum in the coefficient of performance. This trend cannot be distinguished in the current data due to the

insufficient accuracy in the differential pressure transducer.

The tapered microchannel geometry used by Lu and Pan [53] had a COP that was approximately 100 times greater than for the confined jet geometry. Their device consisted for ten parallel channels 26 mm long, 75 μm deep, with a 100 μm inlet and 560 μm outlet. While the COP of the microchannel is much higher than the COP for the current research, there are additional factors that contribute to performance of a heat transfer device. For the tapered microchannel geometry, the heat flux applied was three times lower that the confined jet but the maximum wall temperature was over 10 ^oC higher. Additionally because of the radial geometry in the impinging jet, for certain flow conditions, there can be a pressure recovery or the exit pressure can be greater than the inlet due to the expansion of the fluid. These factors, including the difference in length scales (micro versus mini), indicate that the COP, as it has been defined, may not be a comparable performance measure between the two geometries. Two-phase microchannel geometries have higher heat transfer coefficients and greater convective surface area, compared to confined jets. They are also susceptible to flow instabilities that limit performance and can lead to device failure. Although the heat transfer performance of the confined jets is less than microchannels, the inherent flow stability makes them a more robust design option. Examination of the confined jet flow stability is presented in section 7.5.

7.3 Experimental Comparison to Correlations

Experimental data were compared to existing single-phase and two-phase correlations. The wall temperature was extrapolated from the middle thermocouple and is assumed to be constant for the entire surface. The appropriate area-averaged

versions of each correlation were used for the comparison.

7.3.1 Single-Phase Correlations

The single-phase correlations from Martin [5], Li and Garimella [22], and Chang et al. [20] are compared to experimental data and are presented in Figs. 7.13- 7.15. The correlations are compared to three mass flow rates of 150, 300, and 600 g/min at a gap spacing of 4mm.

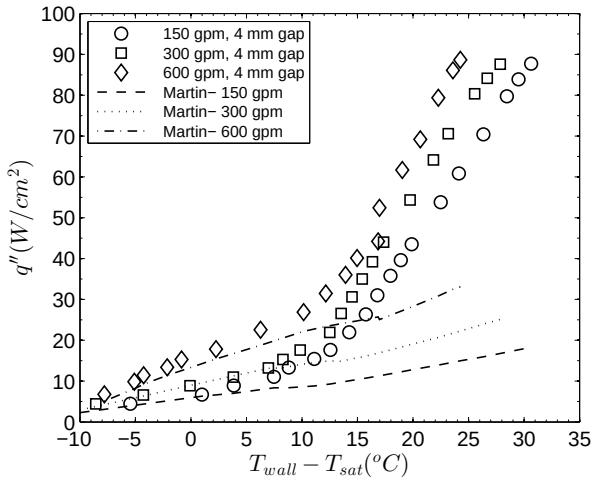

Figure 7.13: Comparison of Martin [5] correlation to experimental results for 4 mm gap spacing.

The Martin [5] correlation is a function of the Reynolds number, Prandtl number, ratio of jet diameter to impingement surface diameter, and nozzle-to-surface spacing. For the current test matrix, the Reynolds number is only a function of the mass flow rate since the nozzle diameter and working fluid are fixed. However, because the range of nozzle-to-surface spacings were well within the length of the potential core, there was no effect on heat transfer performance with respect to nozzle-to-surface spacing.

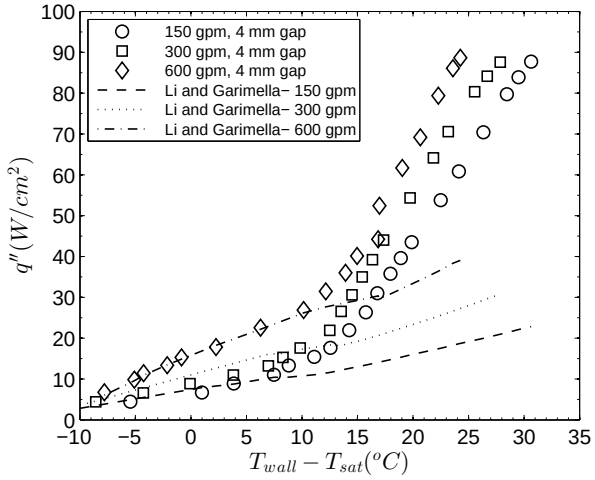

Figure 7.14: Comparison of Li and Garimella [22] correlation to experimental results for 4 mm gap spacing.

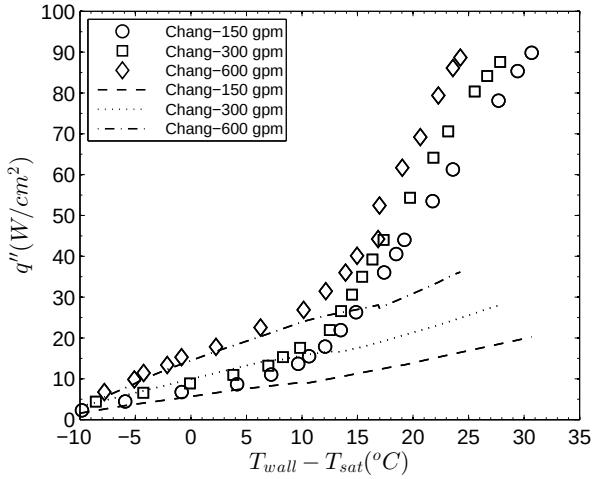

Figure 7.15: Comparison of Chang et al. [20] correlation to experimental results for 4 mm gap spacing.

Increasing Reynolds number, or mass flow rate for the current test conditions, caused an increase in the single phase heat transfer, which is predicted by all three correlations. However, where the Martin [5] correlation under predicted the single-phase heat transfer, the Li and Garimella [22] correlation also accurately predicted

the single-phase heat transfer for the range of conditions tested. Similarly, the single-phase correlation from Chang et al. [20] provided accurate predictions of surface heat flux (q_s'') as a function of excess temperature($T_w - T_{sat}$).

7.4 Two-Phase Correlations

The Rohsenow [40] pool boiling correlation was used as a means of assessing the surface-fluid parameter, $C_{s,f}$, and the exponent to the Prandtl number, n, using the pool boiling data shown in Fig. 7.4. Experimental results for $C_{s,f}$ and n, reported by Pioro [41], were used as a reference but the reported values differed slightly from those that best fit the current set of data. Values of $C_{s,f} = 0.016$ and $n = 1.26$ were used in the two-phase confined jet correlation for water, described in section 4.3, and compared to the experimental results in Fig.7.16 and Fig. 7.17 which are boiling curves for 2 mm and 6mm gap spacings, respectively

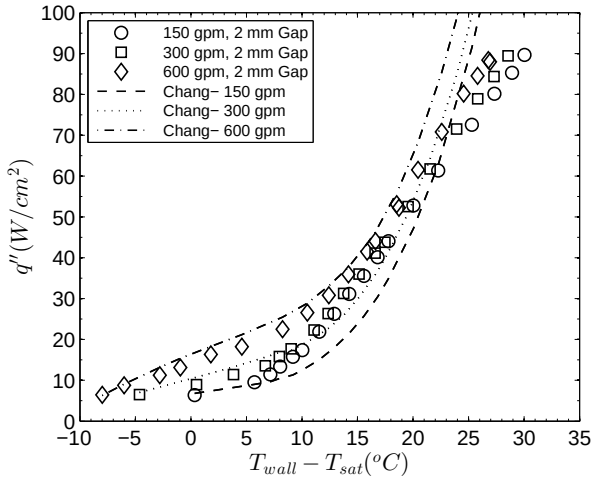

Figure 7.16: Comparison of two-phase confined jet correlation to experimental results for 2 mm gap spacing.

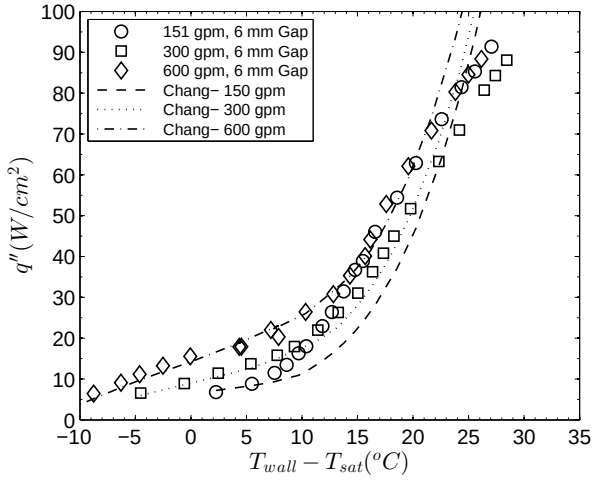

Figure 7.17: Comparison of two-phase confined jet correlation to experimental results for 6 mm gap spacing.

The correlation predicts the single-phase trends of increased heat transfer for an increase in Reynolds number, and correspondingly mass flow rate for the current fixed nozzle diameter, and collapses to the slope of the data in the nucleate boiling regime. Examination of the expression for the total heat transfer, Eqn. 4.2 combned with Eqns. 4.16 and 4.17 for the single phase and nucleate boiling heat transfer coefficients, gives insight into the behavior results from the correlations. For the nucleate boiling contribution, the temperature difference term is raised to the 3.5 power, which allows for the change in the slope of the curve to model the nucleate boiling regime. Although the data are not a function of the inlet mass flow rate in the nucleate boiling regime, the correlation is still a sum of the single-phase and two-phase components. This causes a shift in the curve, over the range of conditions tested, for an increase in mass flow rate. This suggests that a piece-wise function might give better results if results over the entire range are desired. Using $\pm 25\%$ error bands the experimental versus calculated values of heat flux are plotted to check the accuracy of the correlation in Fig. 7.18 and Fig. 7.19.

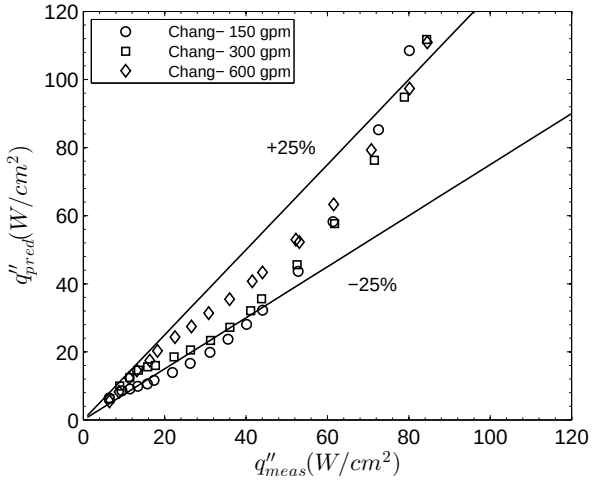

Figure 7.18: Accuracy of two-phase confined jet correlation for 2 mm gap spacing.

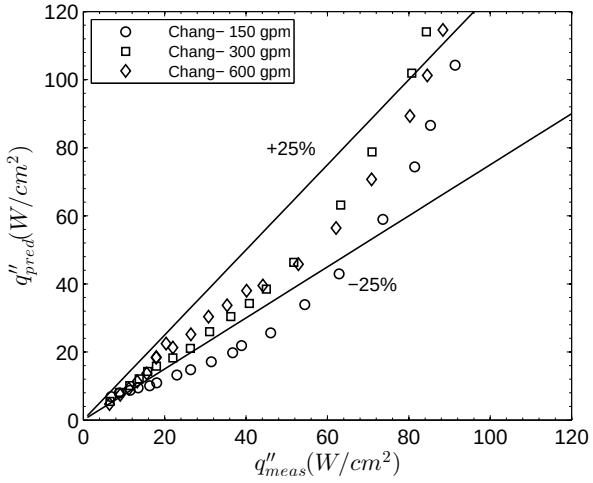

Figure 7.19: Accuracy of two-phase confined jet correlation for 6 mm gap spacing.

At high heat fluxes the correlation over predicted the results and for the lowest mass flow rate the correlation under predicted the surface heat flux. For the 2 mm and 6 mm gap spacings, the results are over predicted for a surface heat flux greater than 70 W/cm^2 and outside the error margins above 80 W/cm^2. This can be attributed to the two-phase component of the correlation uses being derived from the Rohsenow [40] pool boiling correlation, which is valid only for the isolated

bubble formation region of the boiling curve. At higher heat fluxes, that correspond to the columns and jets region of the boiling curve, the correlation diverges from experimental data and over predicts the results. Additionally for both gap spacings, the lowest inlet mass flow rate case, 150 g/min, is under predicted and outside the error margin for the single phase and partial nucleate boiling regimes. In the single-phase and partial nucleate boiling regimes, the correlations accurately predict the heat transfer for the 300 and 600 g/min cases up to approximately 75 W/cm^2. The proposed correlation with a subcooled inlet condition and a constants for the current experimental conditions proved to be fairly successful in predicting the surface heat flux, for the 300 and 600 g/min cases at heat fluxes less than 75 W/cm^2.

7.5 Stability

The stability of the impinging jet is examined using the high frequency time varying upstream pressure data collected during each steady state point. In the single-phase region there are almost no fluctuations in the inlet pressure, hence pressure data from this region is omitted from the following examination. Once boiling begins, small amplitude low frequency oscillations with higher frequency superimposed oscillations begin to appear in the inlet pressure time series. A representative time series of the inlet pressure data is shown in Fig. 7.20 for a flow rate of 300 g/min, gap spacing of 6 mm, and a surface heat flux of 45 W/cm^2. The PSD corresponding to the same time series, Fig. 7.21, shows a low power dominant frequency at approximately 2 Hz. This time series is representative of a stable flow scenario. Over the entire range of input heat fluxes corresponding to two-phase

flow conditions, the dominate frequencies varied from 1-3 Hz with power levels, $\wp$, below 0.14 kPa^2/Hz . The dominate frequencies and their associated powers, respectively, are plotted as a function of heat flux in Fig. 7.22 and Fig. 7.23 for the 300 g/min case for gap spacings of 2 mm, 4 mm, and 6 mm.

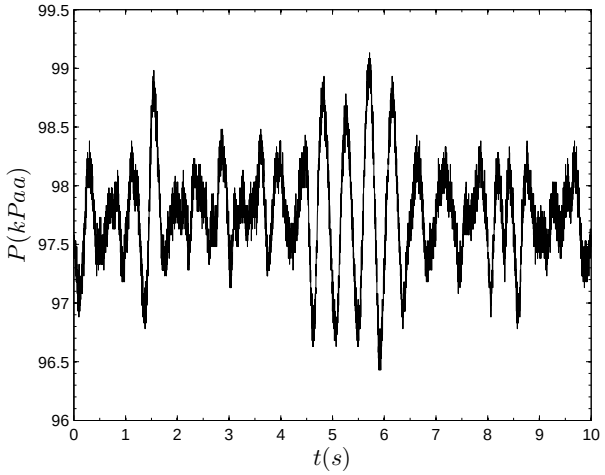

Figure 7.20: Time series for 300 gpm, 6 mm gap spacing, and $q'' = 45\ W/cm^2$.

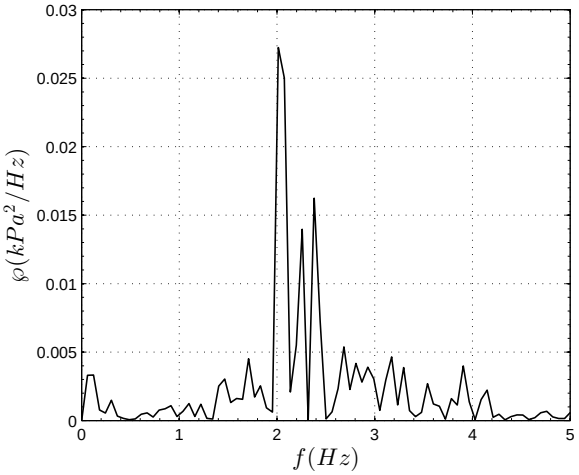

Figure 7.21: PSD for 300 gpm, 6 mm gap spacing, and $q'' = 45\ W/cm^2$.

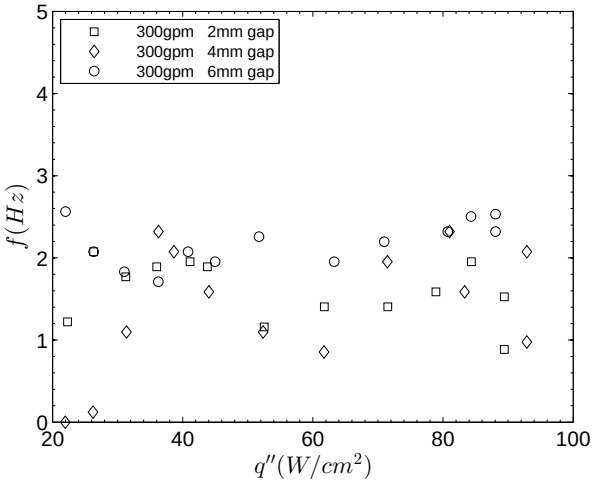

Figure 7.22: Dominate frequencies as a function of heat flux for a 300 g/min flow rate.

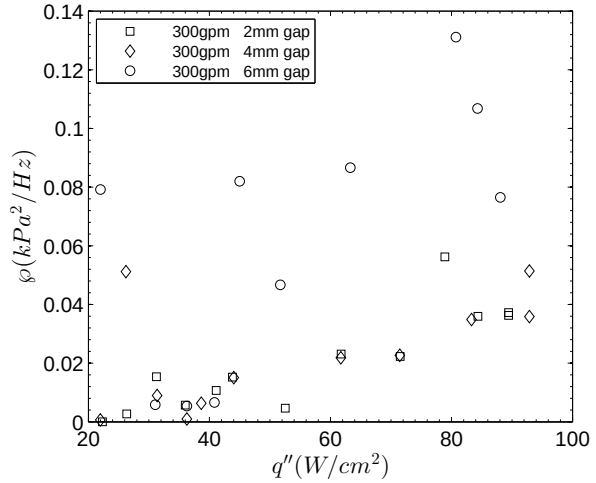

Figure 7.23: Power of dominate frequencies as a function of heat flux for a 300 g/min flow rate.

Figures 7.22 and 7.23 illustrate the range of dominate frequencies and associated power distributions in pressure fluctuations seen during operation over the range of gap spacings and mass flow rates tested. In the time series data shown in Fig. 7.20, the average inlet pressure is below atmospheric pressure for the case

examined. The radial expansion of the fluid in the confined jet causes a pressure recovery, or increase, which results in the sub-atmospheric inlet pressure. Because all test cases in Figs. 7.22 and 7.23 yielded stable flow conditions, these figures serve to give a base-line indicator of a confined jet system operating with no indication of instabilities present.

The dominate frequencies observed in the data match the results of Balasubramanian and Kandlikar [50], who reported a dominant frequency of ≈ 2 Hz in their pressure drop data. This oscillation was reported to be the bubble departure frequency for lower heat fluxes. At higher heat fluxes the frequency decreased slightly and was reported to be the vapor slug frequency. To verify that the pressure fluctuation in the current research are caused by the bubble departure frequency, Eqn. 2.13 was used to estimate the bubble departure frequency. The results of this calculation show the departure frequency to be on the order of 40 Hz for the current test conditions, which does not match the results reported. Qualitative observations of vapor slugs in the condenser lines coupled with the inlet pressure data suggest that fluctuations in the current research result from the expansion of the vapor phase in the device and the subsequent collapse and condensation in the outlet vapor line. Average inlet pressures for three mass flow rates (150, 300, 600 g/min) and two gap spacings (2 mm and 6mm) are shown in Fig. 7.24 and Fig. 7.25, respectively.

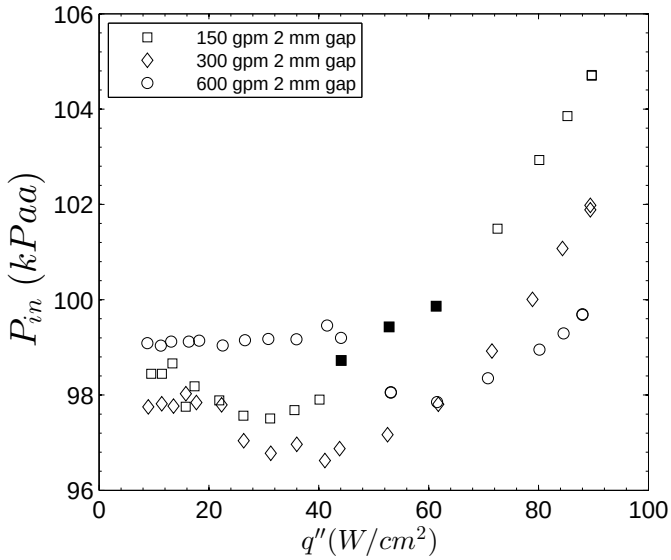

Figure 7.24: Inlet pressure as a function of heat flux for 2 mm gap spacing, solid markers indicate unstable points.

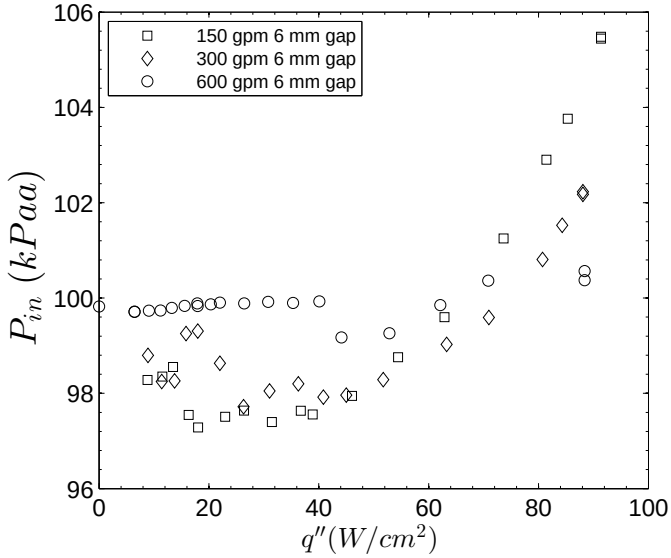

Figure 7.25: Inlet pressure as a function of heat flux for 6 mm gap spacing.

Examination of Figs. 7.24 and 7.25 illustrates that the inlet pressure is relatively constant in the single-phase region. Once nucleate boiling begins, the inlet

pressure drops slightly and then increases again as the vapor generation rate increases. The decrease in the inlet pressure results from the increased mixing of the fluid, due to the bubble formation and departure, which lowers the bulk viscosity of the fluid and pressure drop through the device. After this minimum, the heat flux, and correspondingly the vapor generation, increases so does the pressure drop. For a fixed inlet mass flow rate this corresponds to an increase in the inlet pressure. The heat flux corresponding to the decrease in inlet pressure is dependent on the mass flow rate, as this dictates when boiling occurs.

For one of the test cases examined, high amplitude oscillations were present over a specific range of heat fluxes. These instabilities were present with a mass flow rate of 150 g/min, 2 mm gap spacing, and a over a heat flux range of 40-65 W/cm^2. Figures 7.26 and 7.27 are representative a time series and PSD, respectively, for the given flow conditions at a heat flux of 53 W/cm^2 that illustrate the unstable flow condition.

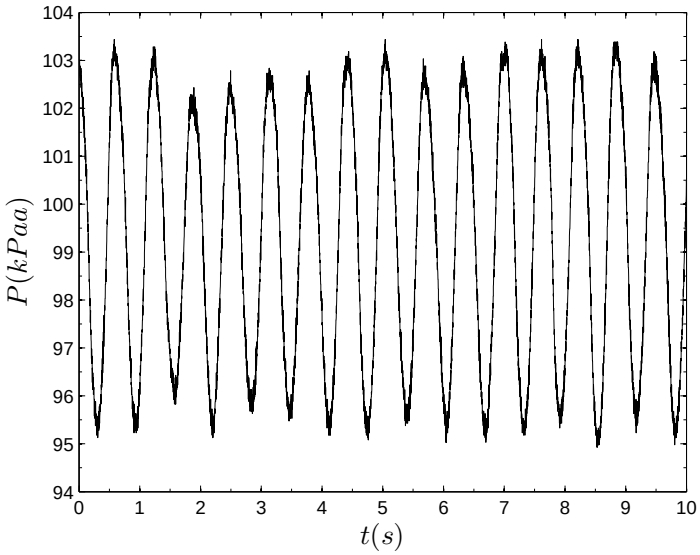

Figure 7.26: Time series for instability seen at 150 g/min, 2 mm gap spacing, and $q'' = 53\ W/cm^2$.

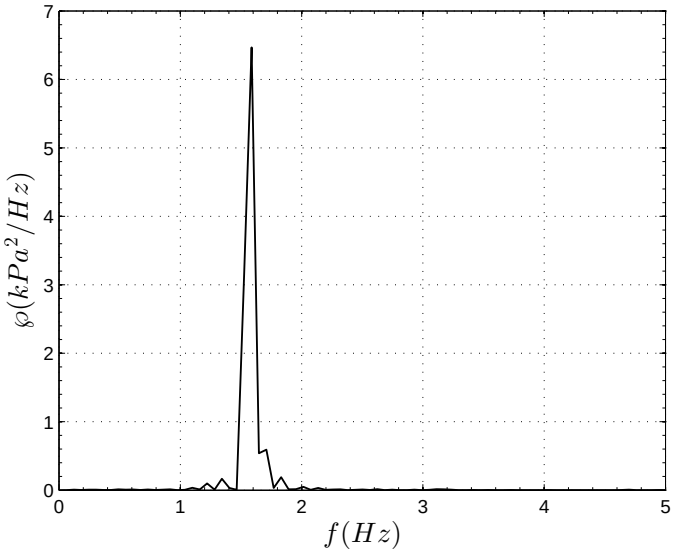

Figure 7.27: PSD for instability seen at 150 g/min, 2 mm gap spacing, and $q'' = 53\ W/cm^2$.

Additionally, during initial testing it was discovered these high amplitude pressure oscillations were a result of the design of the condenser line and could be induced by restricting the vapor exit area and thereby increasing the exit vapor pressure drop. Normally three ports are open in the top of the test piece for the outlet vapor to exit through. Using only one of these ports increased the pressure drop for the outlet vapor, which resulted in high amplitude pressure oscillations. With increasing vapor generation rates, the pressure drop through the exit port and condenser line increases to the point that the pressure in the test device is below that necessary to drive the vapor through the condenser line. The pressure in the test device then increases until it is high enough to drive the vapor out the exit port and through the condenser line. Once the vapor exits, there is a drop in the device pressure. This cycle repeats itself, oscillating between the pressure necessary to drive the vapor through the condenser and the resulting pressure min-

imum. As the vapor generation rate increases, so does the device pressure until it reaches a point where it is high enough to drive the vapor through the exit port and the condenser. At this point, the instabilities subside and the pressure time series return to those typically observed in Fig. 7.20. An example of a representative unstable pressure time series and its corresponding PSD, which are a result of this drop in device pressure, are shown in Fig. 7.26 and Fig. 7.27, respectively.

Two unstable control cases were taken with only one vapor port open to increase the exit vapor pressure drop and ensure that instabilities would be present. These cases were taken to illustrate that the current instabilities observed in the system were a result of the condenser design and to allow for unstable characteristics to be observed. The power of the fluctuation associated with the dominant frequency and obtained from the PSD are plotted as a function of heat fluxes in Fig. 7.28 for two flow rates, 150 and 300 g/min, and a gap spacing of 2 mm. Data corresponding to test cases were the instabilities were induced by restricting size the outlet vapor port are denoted by solid symbols. Data for similar flow conditions but with unforced instabilities are also presented in Fig. 7.28 as unfilled symbols. Unforced instabilities, $\wp > 2kPa^2/Hz$, were found in the data set with a flow rate of 150 g/min, gap spacing of 2 mm, and over the range of heat flux 40 - 65 W/cm^2.

Significant oscillations exist over the range of heat fluxes from 40 -70 W/cm^2 for the two control cases and the 150 g/min, 2 mm gap test case. Because the condensed vapor exits to atmospheric pressure, for these instabilities to occur the following criteria must be met:

$$P_{device} < [\Delta P_{vapor} + P_{amb}] \tag{7.4}$$

where ΔP_{vapor} is the vapor pressure drop due to minor losses as it passes through

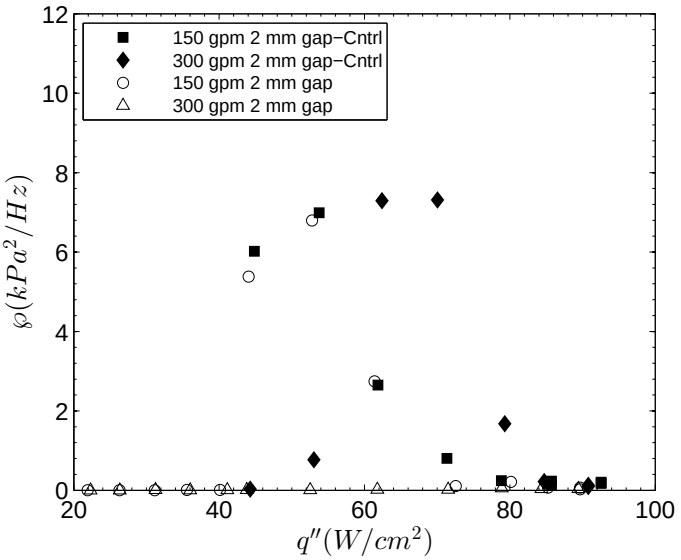

Figure 7.28: Power as function of heat flux.

the exit ports and then condenses in the condenser line. The device pressure, once boiling begins, is a function of the vapor generation rate, which is higher for lower inlet mass flow rates. The vapor pressure drop is also a function of the vapor generation rate. The frequency of the pressure fluctuations, shown in Fig. 7.29, for the two control cases and the other two cases taken at a 2 mm gap spacing, do not vary significantly between the two forced unstable cases and the two cases with the same flow conditions. Instabilities occurred in three of the four cases presented in Fig. 7.29 but no definitive frequency delineation exists between stable and unstable cases. However, the frequency does increase slightly for an increasing heat flux and then drops precipitously at the highest heat flux.

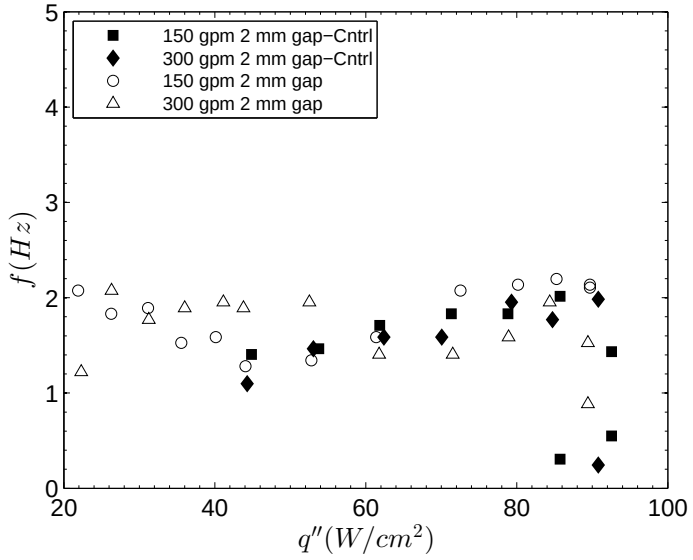

Figure 7.29: Dominant frequency as function of heat flux.

The instabilities are a function of the vapor generation rate and the device pressure, both of which depend upon the inlet mass flow rate and heat flux. Non-dimensionalizing the power of the pressure oscillations and the input power are accomplished using

$$N_{power} = \frac{\wp f}{P_{in}^2} \tag{7.5}$$

and

$$Bo = \frac{Q_{in}}{\dot{m} h_{lv}} \tag{7.6}$$

,respectively. The non-dimensional results are plotted against one another in Fig. 7.30. The unstable flow conditions correspond to a scaled non-dimensional power value greater than approximately 0.2×10^{-3} over the range of Boiling numbers from 0.12 to 0.23. The instabilities from the 300 g/min control case were present over the range of Boiling numbers from 0.12 to 0.15. Instabilities were observed for 150 g/min cases over the range of boiling numbers from 0.15 to 0.23. While

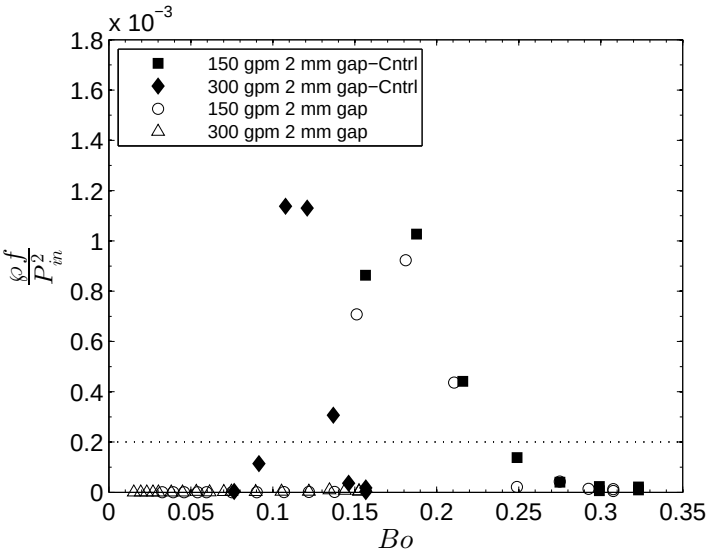

Figure 7.30: Non-dimensional power versus the Boiling number for unstable cases.

this non-dimensionalization does not collapse the data, it preserves the relation of the pressure fluctuation power to the inlet pressure and input heat. Use of existing non-dimension relationships, such as the phase change and subcooling numbers used by Lu and Pan [53], did not preserve the influence of inlet pressure and heat flux. Comparison of stability results with the work of Lu and Pan [53] demonstrates that the confined impinging jet is capable of operating at higher heat fluxes with much lower pressure oscillations. However, as demonstrated by the forced or controlled instability cases, this is predicated upon the exit vapor lines being managed properly.

In Fig. 7.31 the performance of one of the unstable control cases is compared to a test cases with same flow parameters but with stable flow conditions. For the unstable flow condition, over the range of heat fluxes tested, the heat transfer performance was not adversely influenced by the presence of flow instabilities. This can only be said for the confined jet flow geometry presently under study. Although

pressure drop instabilities in microchannels have been shown to be a precursor to dry out and subsequent device failure, it can be concluded that pressure fluctuations in the current study do not significantly alter wetting of the heated surface. Hence, instabilities in the confined jet, under the existing test conditions, are likely to not be indicative of dryout. The inherent stability, associated with the radial expansion of the working fluid in the confined jet geometry, suppresses flow instabilities within the confinement surface. The instabilities observed in the current testing were a system instability associated with the vapor exiting the test device and passing through the condenser line.

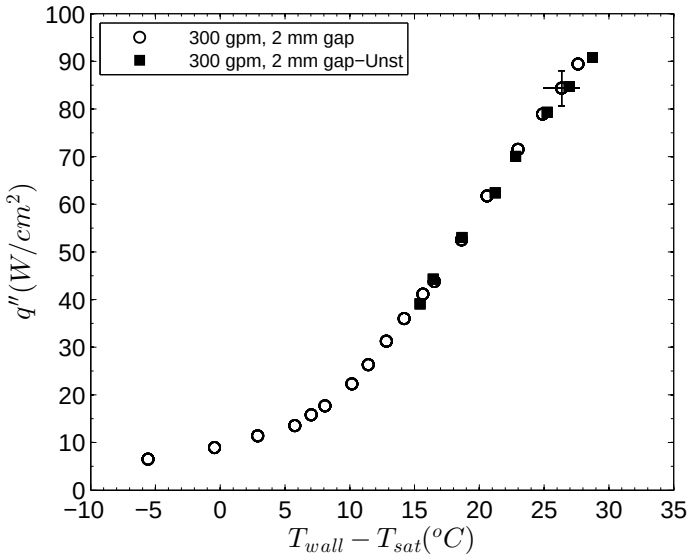

Figure 7.31: Performance comparison of stable case and unstable control case with the same flow conditions.

Chapter 8 – Conclusion and Recommendations

A summary of the findings is presented and recommendations for future work with confined impinging jets are provided in this chapter.

8.1 Conclusion

Confined jet impingement heat transfer and stability was examined using experimental results that vary the inlet jet mass flow rate and nozzle-to-surface (gap) spacing. Increasing demand for robust and stable high heat flux cooling was the motivation for performing the current research. Heat transfer performance was presented using boiling curves, the results of which were compared to existing correlations. Stability characteristics were examined by analysis of the time series data from the inlet pressure transducer.

The experimental setup consisted a 4 mm diameter jet with ten degree subcooled water that impinged on a 38 mm diameter gold plated aluminum heater block. The test device was designed to be modular and allow for changes in gap spacing, heat input, and replacement of the upper confinement surface to allow for vapor extraction studies in the future. Evaluation of the heat losses allowed for the input power to be corrected and used to calculate the applied surface heat flux. The surface temperature was extrapolated using a 1-D conduction model and temperature readings from thermocouples inside the heater block. The uncertainty in the experimental results were quantified and example calculations are located in the appendices.

Boiling curves indicated that an increase in mass flow rate served to enhance the single-phase regime and delay the onset of nucleate boiling. Nozzle-to-surface spacing was determined to not influence heat transfer performance, over the ranges of nozzle-to-surface spacings tested, in either the single-phase or two-phase flow regimes. Surface characteristics and preparation were found to strongly affect heat transfer performance during nucleate boiling. Due to the location of the thermocouples used for evaluation of the surface temperature, the surface was assumed to have a constant temperature and was compared to the area averaged correlations for single-phase and two-phase heat transfer. Using constants deemed most appropriate for the existing fluid and impingement surface conditions, correlations predicted the measured heat flux within 25% for the two higher mass flow rate cases. The results from the lowest mass flow rate case were outside the 25% error margin for the single-phase and partial nucleate boiling regimes. The two-phase component of the correlation used was derived from the Rohsenow [40] pool boiling correlation, which is only valid for the isolated bubble region of the boiling curve. At higher heat fluxes, the correlation over predicts the surface heat flux. This is reflected in the comparison of the correlation to the experimental data at heat fluxes above 75 W/cm^2.

The coefficient of performance, defined as the ratio of energy removed to the required fluid flow power, was used to compare the heat transfer performance of the current research to that of the microchannel array used by Lu and Pan [53]. As measured by the COP, the microchannel's performance was one hundred times greater than the confined jet geometry. Despite this result, the confined jet geometry has a maximum heat flux three times great than the microchannel array and a 10^oC lower maximum wall temperature. Depending upon desired operating

conditions, the COP may not be the best measure of performance comparison between the two geometries.

Stability characteristic results indicate that pressure drop instabilities can exist if the pressure drop required for the vapor generated to exit the test device is greater than the driving pressure in the test device. Unstable flow, characterized by large amplitude pressure fluctuations, was a temporary phenomena which ceased once the upstream pressure reached a value greater than the pressure drop due to minor losses as the vapor passes through the exit plenum and the condenser line. Instabilities were identified by performing a power spectral density on the time series pressure data. The magnitudes of the power associated with these fluctuations were plotted as a function of heat flux to determine the parameters that influence their existence. A method for non-dimensionalizing the results was presented and allowed for a clear indicator of when pressure drop instabilities were present. The instabilities present in the current device were determined to be a result of the condenser line and not the confined gap. The inherent stability associated with the radial expansion of the working fluid in the confined gap suppressed instabilities. To verify this, the performance of an unstable control case was compared to the performance of a stable case . The pressure drop instabilities were determined to have no influence on the heat transfer performance of the confined jet. These results support the hypothesis that the confined impinging jet offers a stable high heat flux alternative to current microchannel designs.

8.2 Recommendations

Nucleate boiling heat transfer has been shown to strongly depend on the surface characteristics of the impingement surface. While a consistent cleaning procedure was used between test cases, differences in technique between operators and changes in the surface topography over time influenced the repeatability of the test results. A method of ensuring the size of the active nucleation sites are the same for each case would allow for more repeatable results. Wet sanding or lapping instead of just cleaning, although time intensive, would allow for the surface characteristics to be more consistent between test cases. Assessing and maintaining thermocouple locations in the heater block was another challenge faced throughout the project. Orienting the thermocouples horizontally instead of vertically would allow for more repeatable positioning and less interference in the measurements from the AC cartridge heaters. Ideally surface temperature measurements could be taken with thermocouples beads embedded and welded to the impingement surface. This would give a means of validating the 1-D conduction extrapolations used in the current research.

For critical heat flux (CHF) testing using a confined impinging jet, the heater block assembly would need to be encases in a material with a much higher maximum working temperature than the PEEK used in the current design. At the 90 W/cm^2 heat flux, the hottest thermocouple gave readings of approximately 190^oC, which is above the glass temperature of the PEEK. This made removing the heater block very difficult and cause some dimension changes that required the device to be remeasured and spacers to be machined.

The size of the outlet plenum was also found to influence results by yielding artificially high measured outlet vapor flow rates. The vapor exiting the confined

jet would push liquid through the vapor ports which cause large discrepancies in the energy balance at high heat fluxes. A larger outlet plenum would allow for more accurate measurements of the outlet flow rates.

Bibliography

[1] Tuckerman, D. B., and Pease, R. F. W., 1981. "High-performance heat sinking for vlsi.". *IEEE Electron Device Letters,* ***ED-2***(5), pp. 126–129.

[2] Pence, D. V., 2002. "Reduced pumping power and wall temperature in microchannel heat sinks with fractal-like branching channel networks". *Microscale Thermophysical Engineering,* ***6***(4), pp. 319–330.

[3] Wolf, D., Incropera, F. P., and Viskanta, R., 1993. "Jet impingement boiling". In *Advances in Heat Tranfer*.

[4] Incropera, F. P., and Witt, D. P. D., 2006. *Fundamentals of heat and mass transfer, 6th edition*.

[5] Martin, H., 1977. "Heat and mass transfer between impinging gas jets and solid surfaces". In *Advances in Heat Tranfer*, Vol. 13. Academic Press, New York.

[6] Lee, D., and Vafai, K., 1999. "Comparative analysis of jet impingement and microchannel cooling for high heat flux applications". *International Journal of Heat and Mass Transfer,* ***42***(9), pp. 1555–1568. Compendex.

[7] Webb, B., and Ma, C.-F., 1995. "Single-phase liquid jet impingement heat transfer". Vol. 26 of *Advances in Heat Transfer*. Elsevier, pp. 105 – 217.

[8] Besserman, D., Incropera, F., and Ramadhyani, S., 1991. "Experimental study of heat transfer from a discrete source to a circular liquid jet with annular collection of the spent fluid". *Experimental Thermal and Fluid Science,* ***4***(1), pp. 41–57. Compendex.

[9] Besserman, D., Incropera, F., and Ramadhyani, S., 1992. "Heat transfer from a square source to an impinging liquid jet confined by an annular wall". *Journal of Heat Transfer,* ***114***(1), pp. 284–287. Compendex.

[10] Chang, C., Kocamustafaogullari, G., Landis, F., and Downing, S., 1993. "Single and multiple liquid jet-impingement heat transfer". In 29th National Heat Transfer Conference, August 8, 1993 - August 11, 1993, Vol. 246 of *American Society of Mechanical Engineers, Heat Transfer Division, (Publication) HTD*, Publ by ASME, pp. 43–52. Compendex.

[11] Elison, B., and Webb, B., 1994. "Local heat transfer to impinging liquid jets in the initially laminar, transitional, and turbulent regimes". *International Journal of Heat and Mass Transfer,* ***37***(8), pp. 1207–1216. Compendex.

[12] Ma, C., and Bergles, A., 1988. "Convective heat transfer on a small vertidcal heated surface in an impinging circular liquid jet.". *Heat Transfer Science and Technology 1988*, pp. 193–200.

[13] Garimella, S. V., and Rice, R. A., 1994. "Heat transfer in submerged and confined jet impingement". In Proceedings of the 1994 International Mechanical Engineering Congress and Exposition, November 6, 1994 - November 11, 1994, Vol. 301 of *American Society of Mechanical Engineers, Heat Transfer Division, (Publication) HTD*, ASME, pp. 59–68. Compendex.

[14] Smirnov, V., Verevochkin, G., and Brdlick, P., 1961. "Heat transfer between a jet and a held plate normal to flow". *International Journal of Heat and Mass Transfer,* ***2***(1-2), pp. 1 – 7.

[15] Sun, H., Ma, C. F., and Nakayama, W., 1993. "Local characteristics of convective heat transfer from simulated microelectronic chips to impinging submerged round water jets". *Journal of Electronic Packaging,* ***115***(1), pp. 71–77.

[16] Womac, D., Incropera, F., and Ramadhyani, S., 1994. "Correlating equations for impingement cooling of small heat sources with multiple circular liquid jets". *Journal of Heat Transfer,* ***116***(2), pp. 482–486. Compendex.

[17] Womac, D., Aharoni, G., Ramadhyani, S., and Incropera, F., 1990. "Single phase liquid jet impingement cooling of small heat sources". *Heat Transfer, Proceedings of the International Heat Transfer Conference*, p. 149. Compendex.

[18] Gardon, R., and Akfirat, J., 1965. "The role of turbulence in determining the heat-transfer characteristics of impinging jets". *International Journal of Heat and Mass Transfer,* ***8***(10), pp. 1261 – 1272.

[19] Garimella, S., and Rice, R., 1995. "Confined and submerged liquid jet impingement heat transfer". *Journal of Heat Transfer,* ***117***(4), pp. 871–877. Compendex.

[20] Chang, C., Kojasoy, G., Landis, F., and Downing, S., 1995. "Confined single- and multiple-jet impingement heat transfer - 1. turbulent submerged liquid jets". *International Journal of Heat and Mass Transfer,* ***38***(5), pp. 833–842. Compendex.

[21] Garimella, S. V., and Nenaydykh, B., 1996. "Nozzle-geometry effects in liquid jet impingement heat transfer". *International Journal of Heat and Mass Transfer,* ***39***(14), pp. 2915–2923. Compendex.

[22] Li, C., and Garimella, S., 2001. "Prandtl-number effects and generalized correlations for confined and submerged jet impingement". *International Journal of Heat and Mass Transfer,* ***44***(18), pp. 3471–3480. Compendex.

[23] Mudawar, I., 2001. "Assessment of high-heat-flux thermal management schemes". *IEEE Transactions on Components and Packaging Technologies,* ***24***(2), pp. 122–141. Compendex.

[24] Kamata, T., Kumagai, S., and Takeyama, T., 1988. "Boiling heat transfer to an impinging jet spurted into a narrow space (part 1, space with an open end)". *Heat Transfer - Japanese Research,* ***17***(5), pp. 71–80. Compendex.

[25] Kamata, T., Kumagai, S., and Takeyama, T., 1988. "Boiling heat transfer to an impinging jet spurted into a narrow space (part II. space with a limited end)". *Heat Transfer - Japanese Research,* ***17***(4), pp. 1–11. Compendex.

[26] Katto, Y., and Kunihiro, M., 1973. "STUDY OF THE MECHANISM OF BURN-OUT IN BOILING SYSTEM OF HIGH BURN-OUT HEAT FLUX.". *Bulletin of the JSME,* ***16***(99), pp. 1357–1366. Compendex.

[27] Ma, C., and Bergles, A., 1986. "JET IMPINGEMENT NUCLEATE BOILING.". *International Journal of Heat and Mass Transfer,* ***29***(8), pp. 1095–1101. Compendex.

[28] McGillis, W., and Carey, V., 1990. "Immersion cooling of an array of heat dissipating elements. an assessment of different flow boiling methodologies". In Parallel and Vector Computation in Heat Transfer - Presented at AIAA/ASME Thermophysics and Heat Transfer Conference, June 18, 1990 - June 20, 1990, Vol. 131 of *American Society of Mechanical Engineers, Heat Transfer Division, (Publication) HTD*, Publ by ASME, pp. 37–44. Compendex.

[29] Monde, M., and Furukawa, Y., 1988. "Critical heat flux in saturated forced convective boiling with an impinging jet coexistence of pool and forced convective boilings". *Heat Transfer - Japanese Research,* ***17***(5), pp. 81–91. Compendex.

[30] Monde, M., and Katto, Y., 1977. "Study of burn-out in a high heat flux boiling system with and impinging jet (part 1, behavior of the vapor-liquid flow).". *Trans. JSME,* ***43***, pp. 3399–3407.

[31] Mudawar, I., and Wadsworth, D., 1991. "Critical heat flux from a simulated chip to a confined rectangular impinging jet of dielectric liquid". *International Journal of Heat and Mass Transfer,* ***34***(6), pp. 1465 – 1479.

[32] Wadsworth, D., and Mudawar, I., 1990. "Cooling of a multichip electronic module by means of confined two-dimensional jets of dielectric liquid". *Journal of Heat Transfer,* ***112***(4), pp. 891–898. Compendex.

[33] Wolf, D., Incropera, F., and Viskanta, R., 1996. "Local jet impingement boiling heat transfer". *International Journal of Heat and Mass Transfer,* ***39***(7), pp. 1395–1406. Compendex.

[34] Liu, Z., Tong, T., and Qiu, Y., 2004. "Critical heat flux of steady boiling for subcooled water jet impingement on the flat stagnation zone". *Journal of Heat Transfer,* ***126***(2), pp. 179–183. Compendex.

[35] Chang, C., Kojasoy, G., Landis, F., and Downing, S., 1995. "Confined single- and multiple-jet impingement heat transfer - II. turbulent two-phase flow". *International Journal of Heat and Mass Transfer,* ***38***(5), pp. 843–851. Compendex.

[36] Zhou, D., and Ma, C., 2004. "Local jet impingement boiling heat transfer with r113". *Heat and Mass Transfer/Waerme- und Stoffuebertragung,* ***40***(6-7), pp. 539–549. Compendex.

[37] Inoue, A., Ui, A., Yamazaki, Y., and Lee, S., 2000. "Studies on cooling by two-dimensional confined jet flow of high heat heat flux surface in fusion reactor". *Nuclear Engineering and Design,* ***200***(1), pp. 317–329. Compendex.

[38] Mitsutake, Y., and Monde, M., 2003. "Ultra high critical heat flux during forced flow boiling heat transfer with an impinging jet". *Journal of Heat Transfer,* ***125***(6), pp. 1038–1045. Compendex.

[39] Shin, C. H., Kim, K. M., Lim, S. H., and Cho, H. H., 2009. "Influences of nozzle-plate spacing on boiling heat transfer of confined planar dielectric liquid impinging jet". *International Journal of Heat and Mass Transfer,* ***52***(23-24), pp. 5293–5301. Compendex.

[40] Rohsenow, W., 1986. "METHOD OF CORRELATING HEAT-TRANSFER DATA FOR SURFACE BOILING OF LIQUIDS.". In Heat Transfer in Electronic Equipment - 1986. Presented at the AIAA/ASME 4th Thermophysics and Heat Transfer Conference., Vol. 57 of *American Society of Mechanical Engineers, Heat Transfer Division, (Publication) HTD*, ASME, pp. 51–60. Compendex.

[41] Pioro, I., 1999. "Experimental evaluation of constants for the rohsenow pool boiling correlation". *International Journal of Heat and Mass Transfer,* ***42***(11), pp. 2003–2013. Compendex.

[42] Hsu, Y. Y., 1962. "On the size and range of active nucleation cavities on a heating surface".

[43] Carey, V., 2008. *Liquid-vapor phase-change phenomena: an introduction to the thermophysics of vaporization and condensation processes in heat transfer equipment*. Taylor and Francis.

[44] Cole, R., 1967. "Bubble frequencies and departure volumes at subatmospheric pressures". *AIChE Journal,* ***13***(4), pp. 779–783.

[45] Novak, and Zuber, 1963. "Nucleate boiling. the region of isolated bubbles and the similarity with natural convection". *International Journal of Heat and Mass Transfer,* ***6***(1), pp. 53 – 78.

[46] Tong, L. S., and Tang, Y. S., 1997. *Boiling Heat Transfer And Two-Phase Flow*, 2 sub ed. CRC Press, Feb.

[47] Boure, J., Bergles, A., and Tong, L., 1973. "Review of two-phase flow instability". *Nuclear Engineering and Design,* ***25***(2), pp. 165 – 192.

[48] Kandlikar, S. G., 2002. "Fundamental issues related to flow boiling in minichannels and microchannels". *Experimental Thermal and Fluid Science,* ***26***(2-4), pp. 389 – 407. Flow boiling;.

[49] Kandlikar, S. G., 2004. "Heat transfer mechanisms during flow boiling in microchannels". *Journal of Heat Transfer,* ***126***(1), pp. 8 – 16. Bubble base;Microchannels;Superheat;.

[50] Balasubramanian, P., and Kandlikar, S. G., 2005. "Experimental study of flow patterns, pressure drop, and flow instabilities in parallel rectangular minichannels". *Heat Transfer Engineering,* ***26***(3), pp. 20 – 27. Boiling heat transfer;Flow boiling systems;Microchannels;Minichannels;.

[51] Kandlikar, S. G., Kuan, W. K., Willistein, D. A., and Borrelli, J., 2006. "Stabilization of flow boiling in microchannels using pressure drop elements and fabricated nucleation sites". *Journal of Heat Transfer,* ***128***(4), pp. 389–396. Compendex.

[52] Qu, W., and Mudawar, I., 2004. "Transport phenomena in two-phase micro-channel heat sinks". *Journal of Electronic Packaging, Transactions of the ASME,* ***126***(2), pp. 213 – 224. Channel instabilities;Hydrodynamic instabilities;Micro-channels;Phase change;.

[53] Lu, C. T., and Pan, C., 2008. "Stabilization of flow boiling in microchannel heat sinks with a diverging cross-section design". *Journal of Micromechanics and Microengineering,* ***18***(7). Compendex.

[54] Salakij, S., Liburdy, J. A., and Pence, D. V., 2009. "Modeling in-situ vapor extraction during convective boiling". In 2009 ASME Fluids Engineering Division Summer Conference, FEDSM2009, August 2, 2009 - August 6, 2009, Vol. 2 of *Proceedings of the ASME Fluids Engineering Division Summer Conference 2009, FEDSM2009*, American Society of Mechanical Engineers, pp. 507–518. Compendex.

APPENDICES

Appendix A – Data Acquisition Program

The details of the data acquisition programs used for data collection are explained in this section. The figures shown below correspond to the temperature, pressure and Coriolis mass flow measurements are listed as data acquisition program 1. The figures that detail the data collection for the power and catch and weigh measurements are listed as data acquisition program 2.

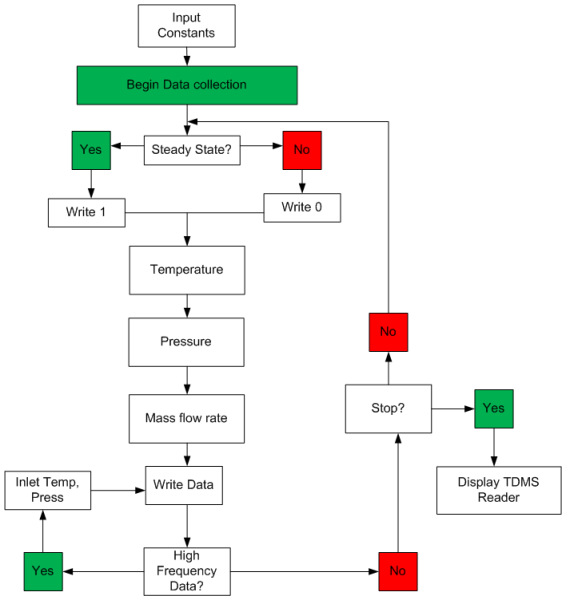

Figure A.1: Process flow chart for data acquisition program 1.

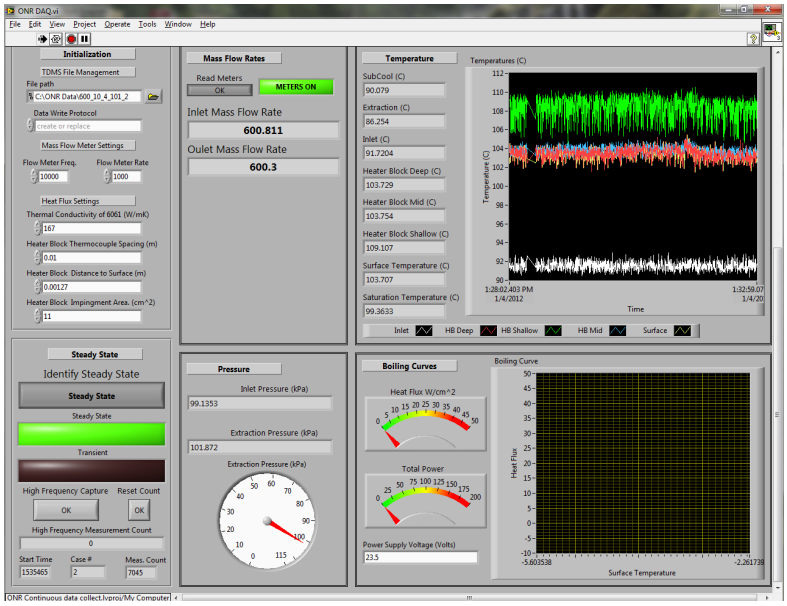

Figure A.2: LabVIEW VI front panel for DAQ program 1.

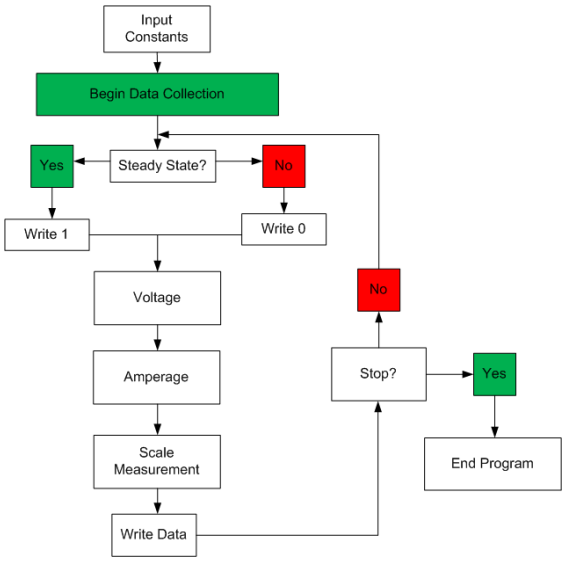

Figure A.3: Process flow chart for data acquisition program 2.

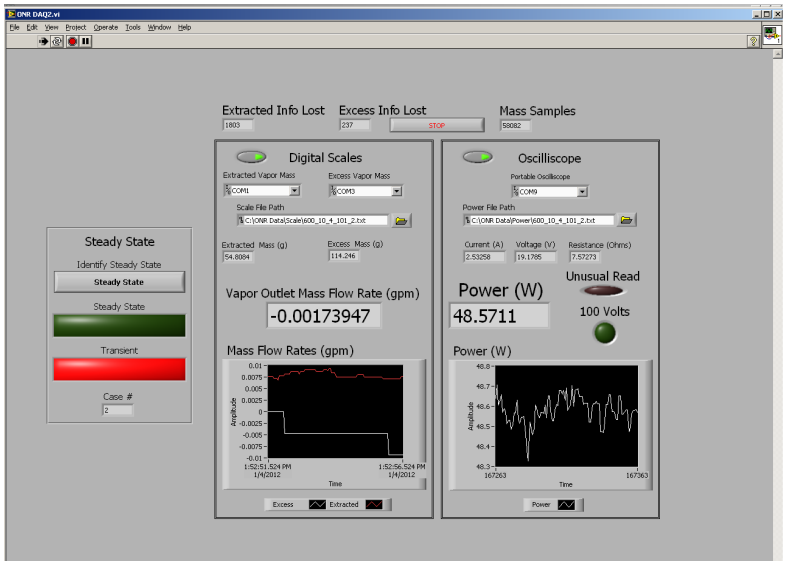

Figure A.4: LabVIEW VI front panel for DAQ program 2.

Appendix B – Test Facility Equipment

The details of the equipment, instrumentation, the calibration process are detailed in the following sections.

B.1 Equipment List

Table B.1: List of equipment and specification used in the experimental facility.

Item	**Make and Model**	**Specifications**
DAQ Computer 1	Dell Optiplex 745	2.13 GHz Intel Core 2 4.0GB RAM
DAQ Computer 2	Dell Optiplex GX280	3.20 GHz Pentium 4 1GB RAM
DAQ Board 1	NI PCI-6034E	200 kS/s, 16-Bit, 16-A-In
DAQ Board 2	NI PCI-MIO-16E-4	500 kS/s (1-C), 250 kS/s (Multil),12-Bit, 16-A-Int
Connector Block	NI SCB-68	Shielded, 68 pin
Oil Bath	Neslab EX7	200C max, 800 Watts, 1.9 Gal oil
Pump Drive	Cole Parmer 75211-10	50-5000 RPM 0.07 HP
Pump Drive	Cole Parmer 75211-50	40-3600 RPM 0.1HP
Gear Pump Head	MicroPump GB-P25	0.58 ml/rev, 8.7 bar max diff. press.

Continued on next page

Table B.1 – continued from previous page

Item	**make and Model**	**Specifications**
Gear Pump Head	Tuthill DGS.57	0.57 m/rev, 17.2 Bar max diff press.
Power supply	Textronix PS2521G	3 outputs,one 0-6V 0-5A, two 0-20V 0.25A
Oscilloscope	Textronix THS720P	
Current Probe	Tektronix A261	
Voltage Probe	Tektronix P5200	
Degassing Tank	GE hot water heater	15 gal, 2000W heater element, 115V
PID temp controller	Omega Cni 3244-DC	0.5C accuracy
Calibration Standard	Omega PCL-1B	0.06% full scale accuracy
Cartridge Heaters	Watlow	3/8 in Dia. 150 Watt

B.2 Instrumentation List

Table B.2: List of instruments and specification for measurements collected.

Measurement	Manufacturer	Model	Calibrated Range
Inlet Temp.	Omega	TMTSS-062G-6	50-120^oC
Inlet Press.	Omega	PX-409	100-200 kPaA
Inlet Mass F.R.	Micromotion	2700R Coriolis	0-800 gpm
Subcooled Temp.	Omega	TMTSS-062G-6	50-120^oC
Heater Temp. 1	Omega	TMTSS-062G-6	50-150^oC
Heater Temp. 2	Omega	TMTSS-062G-6	50-150^oC
Heater Temp. 3	Omega	TMTSS-062G-6	50-150^oC
Differential Pres.	Omega	Omega PX-409	0-34kPa
Outlet Temp.	Omega	TMTSS-062G-6	50-120^oC
Outlet Mass F.R.	Micromotion	2700R Coriollis	0-800 gpm
Extraction F.R.	Scientech	Scientech SA120	0-120g
Excess F.R.	Scientech	Scientech SP350	0-350g

B.3 Calibration Information

Table B.3: Calibration Curves for Instrumentation.

Measurement	Calibration Curve	Uncertainty
Inlet Temp.	$T_{in} = 0.9977T - 3.9496$	0.7^oC
Inlet Press.	$P_{in} = 2049.7V - 0.2$	$0.165kPa$
Differential Pres.	$P_{diff} = 342.157V$	$0.024kPa$
Subcooled Temp.	$T_{sub} = 0.9914T - 2.3612$	0.8^oC
Heater Temp. 1	$T_{HB1} = 0.9992T - 4.1385$	0.7^oC
Heater Temp. 2	$T_{HB2} = 0.9995T - 3.8485$	0.7^oC
Heater Temp. 3	$T_{HB3} = 1.0184T - 4.4224$	0.8^oC
Outlet Temp.	$T_{out} = 1.0157T - 4.4439$	0.8^oC
Coriolis Meters	Factory Calibrated	0.15%FS

Appendix C – Uncertainty Calculations

Sample calculations the heat flux and surface temperature extrapolation are used to show the method used to determine the uncertainty in the experimental results. The Kline and McClintock method was used to propagate the bias and precision errors from the measured values to the final calculated quantities. Sample values are taken from a representative data set and used for the following calculations. The uncertainty in each measurement is found using Eqn. 6.19, which combines the bias errors from calibration with the repeated measurement uncertainty for a 95% confidence interval. The heat flux is determined from the measured voltage and amperage values and then divided by the surface area.

$$q''_{PC} = \frac{IV - Q_{loss}}{A_s} \tag{C.1}$$

$$U_{q''pc} = \sqrt{\left(\frac{\partial q''}{\partial I}U_I\right)^2 + \left(\frac{\partial q''}{\partial V}U_V\right)^2 + \left(\frac{\partial q''}{\partial A_s}U_{As}\right)^2 \left(\frac{\partial q''}{\partial Q_{loss}}U_{Qloss}\right)^2} \tag{C.2}$$

Where

$$U_{AS} = \frac{\partial A_{AS}}{\partial D}U_D \tag{C.3}$$

$$
\begin{aligned}
T_{stat} &= 1.960 \\
D &= 3.8\ cm \\
I &= 3.471\ Amps \\
V &= 131.1\ Volts \\
Q &= 455\ Watts \\
Q_{loss} &= 19.1\ Watts \\
U_D &= \sqrt{(0.00254)^2 + T_{stat} \cdot (0.00254)^2} \\
U_D &= 0.003776\ cm \\
U_A &= \frac{D}{2 \cdot \pi} \cdot U_D \\
U_A &= 0.002284\ cm^2 \\
U_I &= \sqrt{0.01^2 + T_{stat} \cdot 0.0069^2} \\
U_I &= 0.0139\ Amps \\
U_V &= \sqrt{0.5^2 + T_{stat} \cdot 0.2375^2} \\
U_V &= 0.60\ Volts \\
U_{Qloss} &= 1.94\ Watts
\end{aligned}
\tag{C.4}
$$

$$
U_{q''} = \sqrt{\left(\frac{V}{A_s}U_I\right)^2 + \left(\frac{I}{A_s}U_V\right)^2 + \left(\frac{VI - Q_{loss}}{A_s^2}U_A\right)^2 + \left(\frac{1}{A_s}U_{Qloss}\right)^2}
$$

$$
U_{q''pc} = 3.546\ W/cm^2
$$

And now for the uncertainty in the surface temperature calculation, assuming a 3% uncertainty in the material properties.

$$
\begin{aligned}
T_{wall} &= T_{HB2} - q''_{PC}\frac{k}{L_{2w}} \\
U_{Twall} &= \sqrt{\left(\frac{\partial T_{wall}}{\partial q''}U_{q''}\right)^2 + \left(\frac{\partial T_{wall}}{\partial k}U_k\right)^2 + \left(\frac{\partial T_{wall}}{\partial L_{2W}}U_{L2w}\right)^2 + + \left(\frac{\partial T_{wall}}{\partial T_{HB2}}U_{THB2}\right)^2} \\
T_{2W} &= 131.37\,^oC \\
q'' &= 40.12\ W/cm^2 \\
L_{2w} &= 0.65024\ cm \\
k_{6061Al} &= 172\ W/m\cdot k \\
U_{L2w} &= \sqrt{(0.00254)^2 + T_{stat}\cdot(0.004)^2} \\
U_{L2w} &= 0.00606\ cm \\
U_{THB2} &= \sqrt{0.7^2 + T_{stat}\cdot 0.558^2} \\
U_{THB2} &= 1.1\,^oC \\
U_{Tw} &= \sqrt{\left(\frac{k}{L_{2w}}U_{q''}\right)^2 + \left(\frac{q''}{L_{2w}}U_k\right)^2 + \left(\frac{q''k}{L_{2w}^2}U_{L2w}\right)^2 + (U_{THB2})^2} \\
U_{Tw} &= 1.4\,^oC
\end{aligned}
\tag{C.5}
$$

Appendix D – Additional Figures

D.1 Boiling Curves

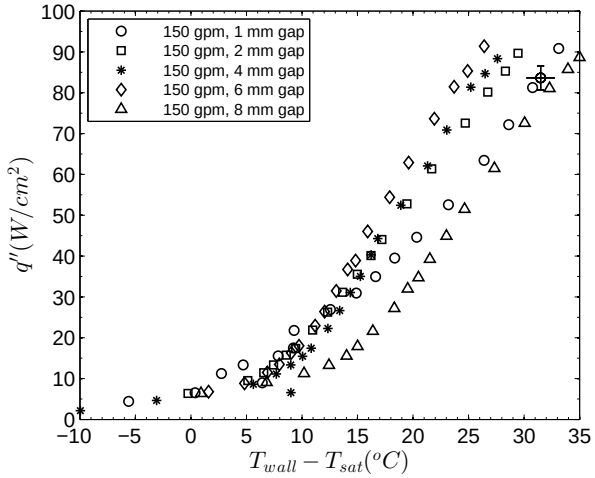

Figure D.1: Boiling curve for 150 gpm and H=1-8 mm.

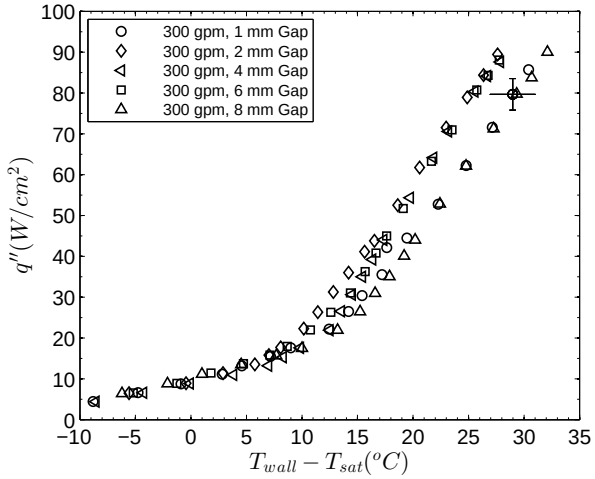

Figure D.2: Boiling curve for 300 gpm and H=1-8 mm.

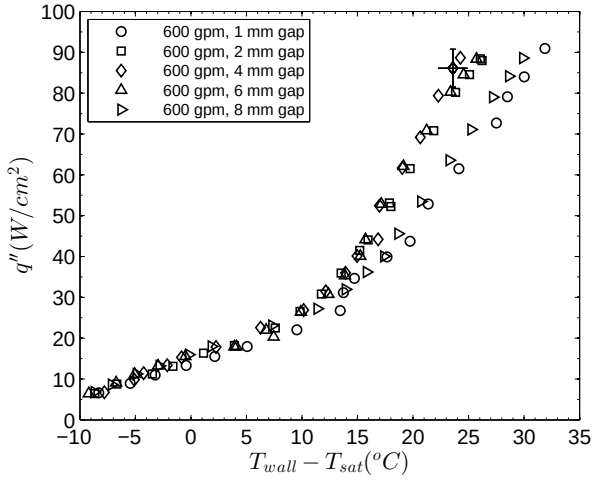

Figure D.3: Boiling curve for 600 gpm and H=1-8 mm.

Appendix E – Machine Drawings

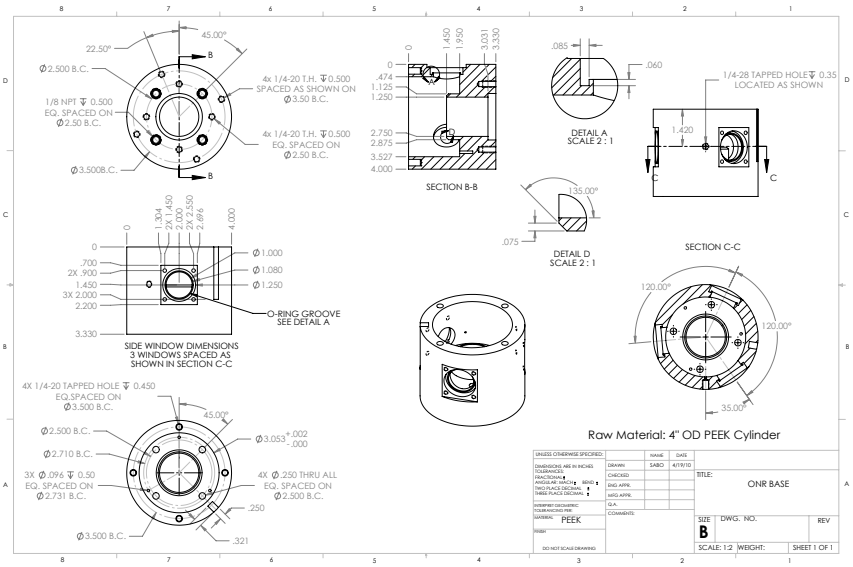

Figure E.1: PEEK lower half of test device housing.

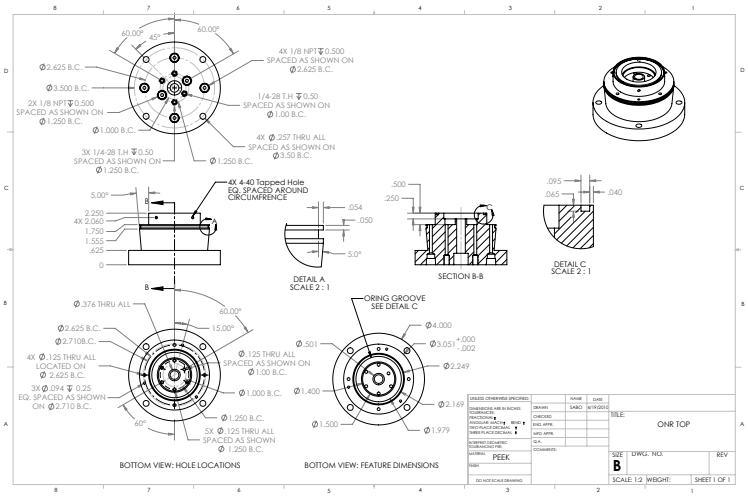

Figure E.2: PEEK upper half of test device housing.

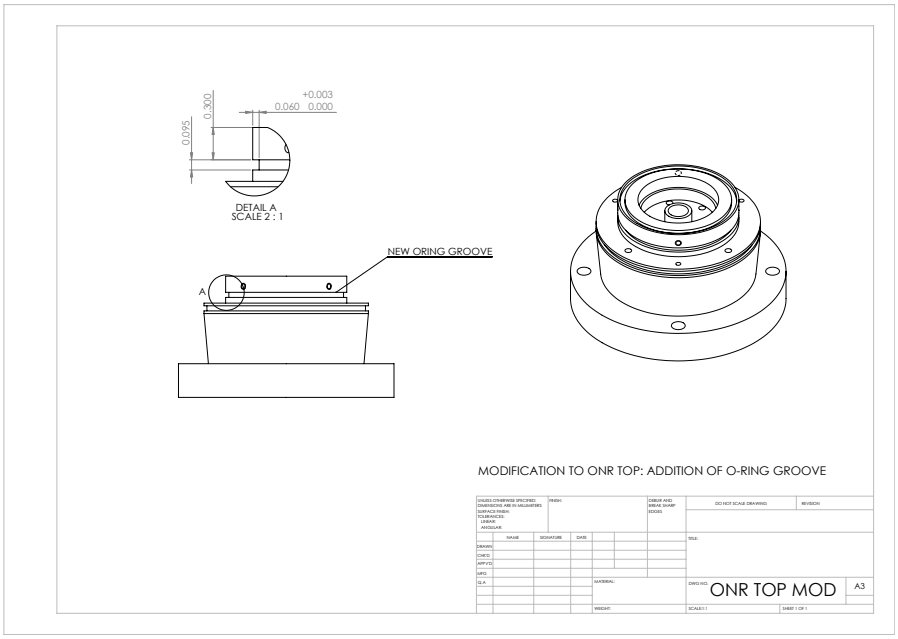

Figure E.3: Modification to upper half of test device housing.

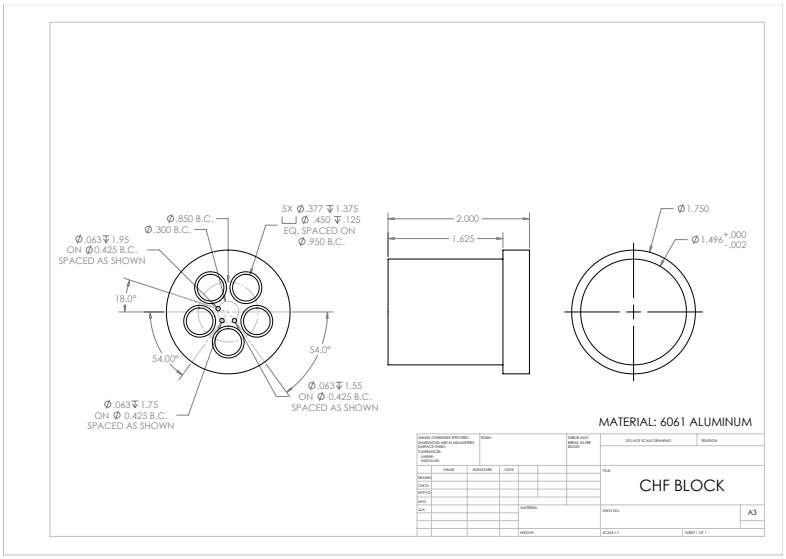

Figure E.4: Aluminum heater block.

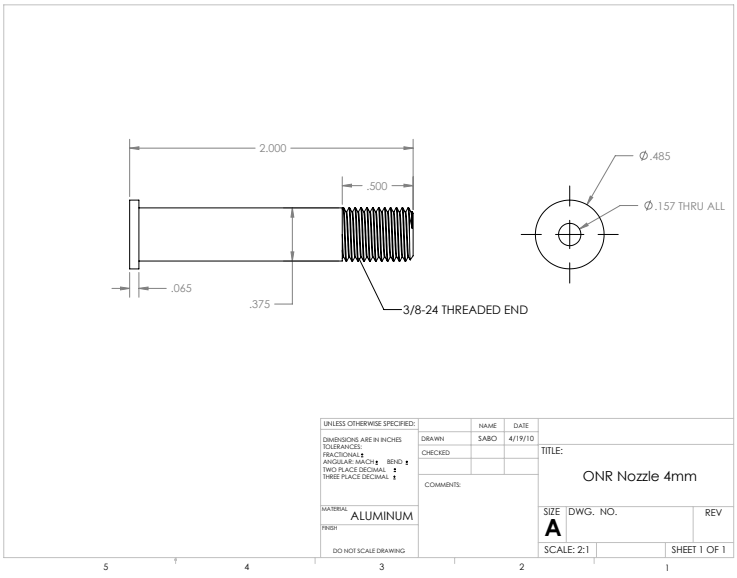

Figure E.5: Male section of two piece nozzle assembly.

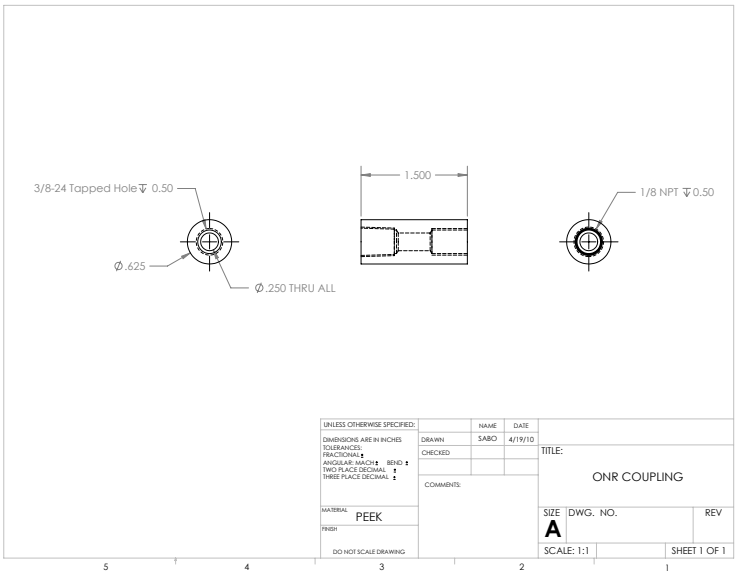

Figure E.6: Female section of two piece nozzle assembly.

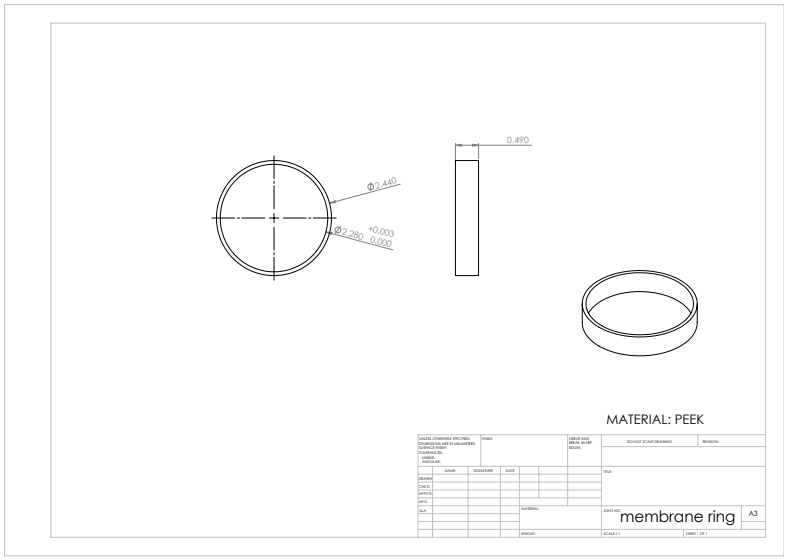

Figure E.7: Outer retaining ring for membrane.

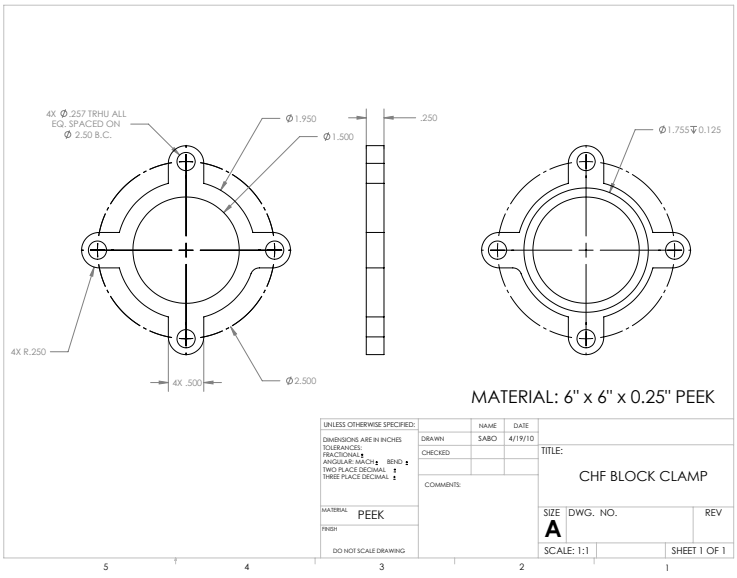

Figure E.8: Retaining clamp for heater block.

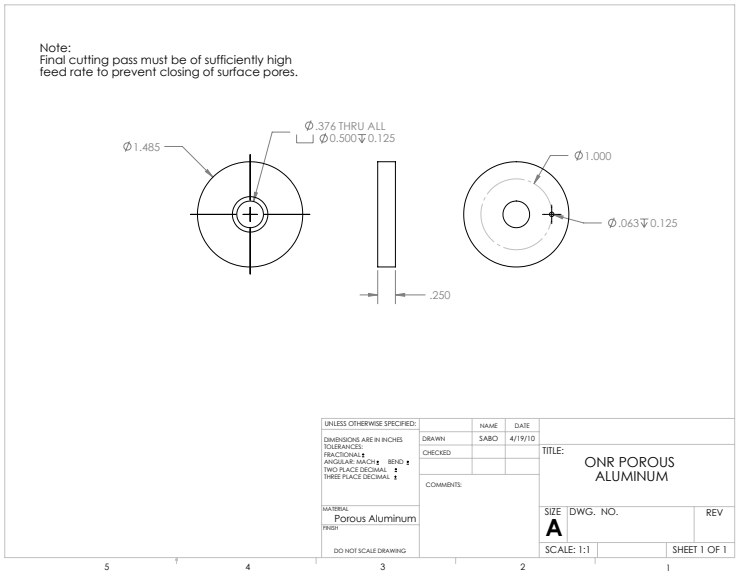

Figure E.9: Porous aluminum backing for membrane.